Application of Photochromic Molecules to Electric Circuit as Photo-Controlling Conductance Switches

Takeshi Sakano

2012

Contents

General Introduction

1. Molecular electronics

The two basic approaches to creating surface patterns and devices on substrates in a controlled and repeatable manner are the "top-down" and "bottom-up" techniques. The former may be seen as modern analogues of ancient methods such as lithography, writing or stamping, but capable of creating features down to the sub-100 nm range. That is mainly because of the optical diffraction limit. To overcome the limitation, bottom-up technology has potential application to create the systems in the size range of about 0.1–100 nm. The size of organic molecules including macromolecules is appropriate to bottom-up technology. The atoms within the molecules are joined in specific, controlled configurations. As a result, space and energy are organized very differently in molecules compared to those in solid metals, semiconductors and insulators. In particular, configuration and electronic properties of functional organic molecules can be easily switched by external stimuli. Therefore, organic molecules have a potential application to the electric circuit elements.

Figure 1 shows the relationship from the molecular design of functional molecules to single molecular switching devices. We firstly design and synthesize the switchable molecules on the theory of physical organic chemistry, secondly measure the single molecular properties, thirdly apply to the basic molecular device, finally create single molecular switching device with a combination of self-assembling properties of organic molecules. The basic researches on all the steps are very important for the molecular electronics. In this thesis, we especially studied the photo-switching behaviors of molecular conductance and self-assembled structures of photochromic diarylethenes.

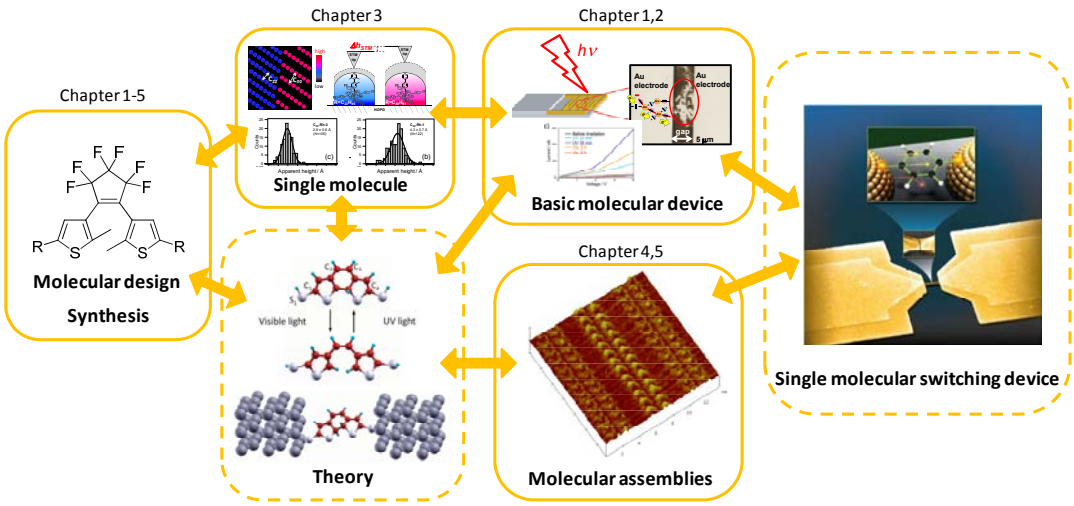

Figure 1. Relationship from molecular design to single molecular switching device.

Historically, the molecular electronics started by the proposal of a molecular rectifier by Aviram and Ratner in 1974 (Figure 2a).[3] Binnig and Rohrer invented scanning tunneling microscope (STM) in 1982, which became breakthrough for not only surface analysis with a atomic resolution but also the investigation of single molecular conductance.[4] In 1991, Ratner firstly demonstrated that cupper-phthalocyanine on the Highly-oriented pyrolytic graphite (HOPG) have the single molecular rectifier properties (Figure 2).[5] Nowadays single molecular conductance is measured by various methods as depicted in the following session.

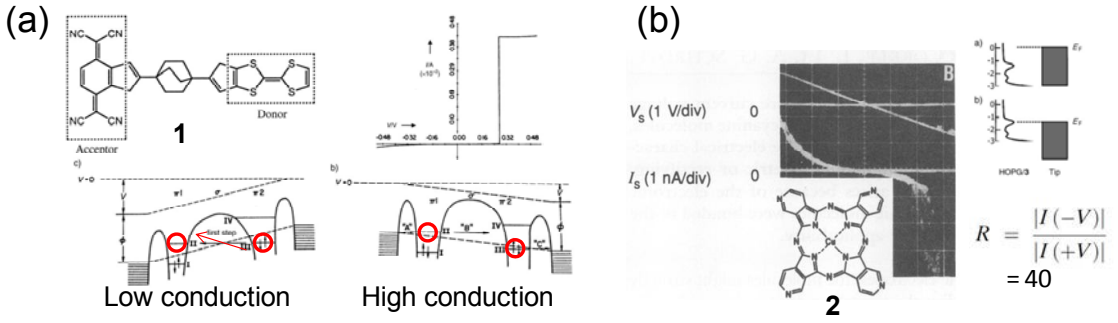

Figure 2. (a) Single molecular rectifier **1** proposed by Aviram and Ratner, and calculated *I*/*V* curve of the molecular rectifier **1**;[3] (b) molecular structure of Cu-phthalocyanine **2** behaving as rectifier on HOPG substrate, and observed *I*/*V* curve of the rectifier **2**.[5]

2. Molecular conductance

2.1 Measuring method of molecular conductance

To determine the single molecular conductance, single molecule is required to be bound between two electrodes. Reed and Tour applied the mechanical controllable break junction (MCBJ) method to determine the single molecular conductance.[6] They prepared the molecular junction by tearing off the thin gold wire coated by 1,4-benzenedithiol and then pushing back together (Figure 3a). This method is based on the formation of self-assembled monolayer on gold surface.[7] Tao introduced the statistical analysis and found that point conductance (G_0) and multi molecular conductance are observed in one conductance histogram (Figure 3b).[8] This method is optimal to determine the single molecular conductance because point conductance guarantees the absolute value of molecular conductance. Weiss applied the STM measurement in the constant current condition to the determination of relative conductance (difference of decay constant, $\Delta\beta$)from apparent height value (Figure 3c).[9] Other methods are summarized in Figure 3.[10-12]

(a) MCBJ

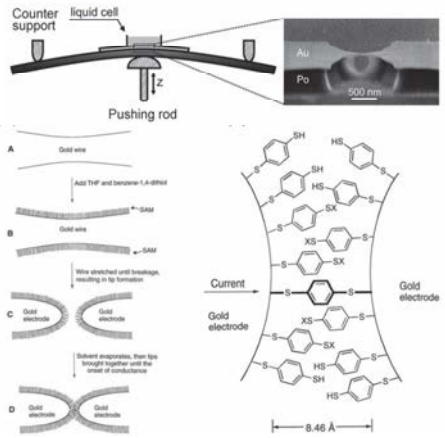

J. M. Tour et al., *Science* **1997**

(b) STM BJ

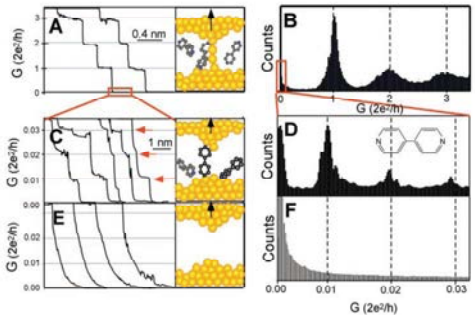

N. J. Tao et al., *Science* **2003**

(c) STM Apparent height measurement

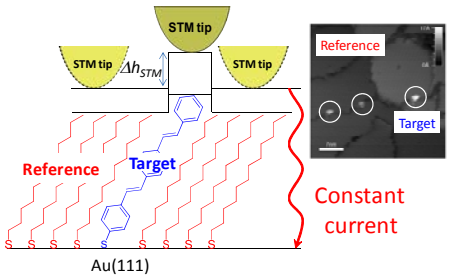

P. S. Weiss et al., *J. Phys. Chem. B* **1999**

(d) Conductive AFM

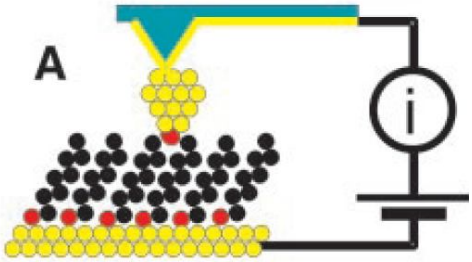

S. M. Lindsay et al., *Science* **2001**

(e) Crossed wire junction

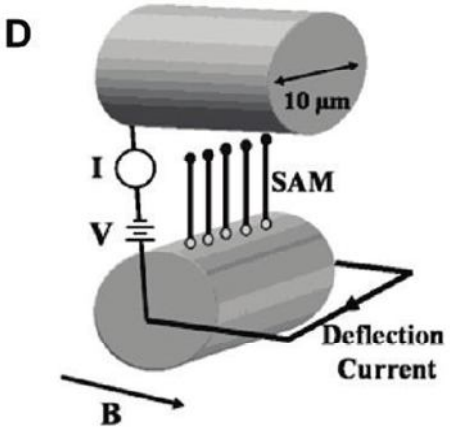

R. Shashidhar et al., *Phys. Rev. Lett.* **2002**

(f) SWNT nanogap electrode

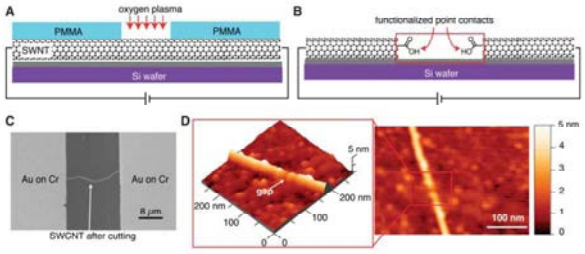

C. Nuckolls et al., *Science* **2006**

Figure 3. Measuring methods of single molecular conductance: (a) mechanical controllable break junction (MCBJ),[6] (b) STM break junction,[8] (c) STM apparent height measurement,[9] (d) Conductive AFM,[10] (e) crossed wire junction[11] and (f) single walled carbon nanotube (SWNT) nanogapped electrode.[12]

2.2 Conduction mechanism

Current flows through the molecules in accordance with the optimal conduction mechanism. When we focus on the direct current, the conduction mechanism depends on the length and applied bias voltage. There are multi mechanisms for the conduction. Here primary two mechanisms are introduced. One is thermally independent tunneling mechanism and another is thermally dependent hopping mechanism. Tunneling mechanism is based on the tunneling phenomena in quantum mechanics; therefore, this conduction is limited to the short range conduction. Conductance of the organic molecules (G) in the direct tunneling mechanism is according to the following equation (1);

$$\text{Tunneling} \qquad G = G_0 \exp(-\beta L) \qquad (1)$$

where G_0 is contuct conductance ($= 2e^2/h$, 12.9 kΩ), β is decay constant ($= 2(2m_e\phi)^{1/2}/\hbar$), L is molecular length, e is elementary charge, h is Plank constant ($\hbar = h/2\pi$), m_e is electron effective mass, ϕ is tunneling barrier height (ϕ is often approximated by the energy difference between the Fermi level (E_F) and the closest frontier orbital (E_{HOMO} or E_{LUMO})). When the Fermi level is resonant to the density of state (DOS) of molecules, conductance is further enhanced. Long range conduction is known as carrier hopping mechanism following equation (2);

$$\text{Hopping} \qquad G \propto (A/L)\exp(-E_a/k_BT) \qquad (2)$$

where A includes carrier density, L is the molecular length, E_a is activation energy, k_B is Boltzmann constant, T is temperature. These two mechanisms are experimentally distinguishable by measuring the temperature dependency on molecular conductance. The tunneling conduction is more important for the molecular electronic devices because the tunneling conduction is highly sensitive to the molecular structure.

Frisbie et al experimentally revealed the transition of these conduction mechanisms by using surface synthesis of conjugated oligophenyleneimine (**OPI**) wire on Au(111) surface (Figure 4a).[13] The conduction mechanism transitioned from direct tunneling to hopping near 4 nm (Figure 4b). Short wires of **OPI 1-4** showed temperature independent tunneling conduction, while long wires **OPI 6-10** showed thermal activated conduction (Figure 4c). The conduction mechanism also transitioned from tunneling to field emission at 0.75 V (Figure 4d). The bias voltage dependency of the conduction mechanism is theoretically revealed by Simmons model.[14] In the low bias region, electron cannot overcome the potential barrier, therefore current flows via direct tunneling mechanism. While, when the potential of electron becomes higher than the barrier by applying high bias voltage, field emission alternates to direct tunneling.

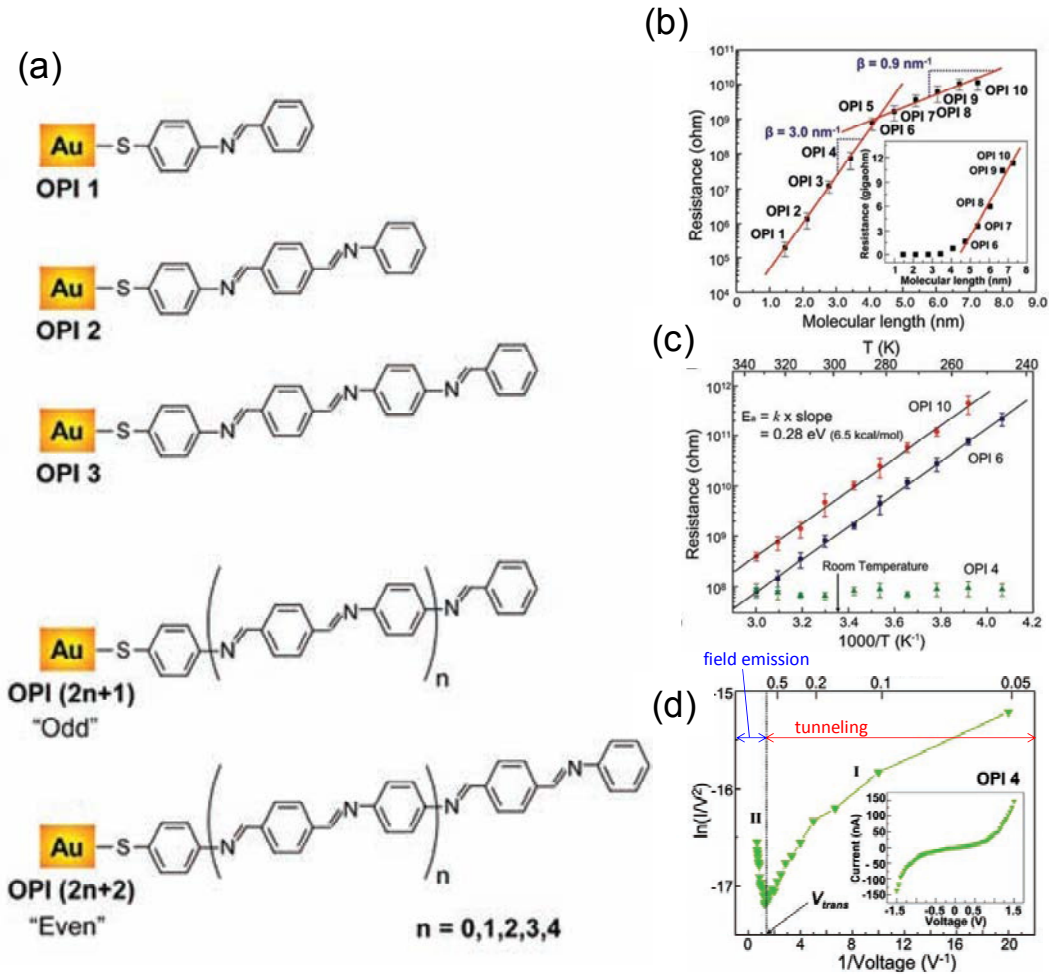

Figure 4. (a) Molecular structures of molecular wires **OPI n**. (b) Length dependence of molecular resistance (**OPI 1-4**: tunneling conduction, **OPI 6-10**: hopping conduction). (c) Temperature dependence of molecular resistance (**OPI 4**: temperature independent conduction, **OPI 6,10**: temperature dependent conduction). (d) Bias voltage dependence on the conduction mechanism.

3. Photochromic molecules as a conductance photo-switching unit

Photochromism is generally known as the photoinduced change between two isomers with different colors.[15] In various photochromic molecules, diarylethene has favorable properties; such as thermally stability of both open-ring isomer and closed-ring isomer, and high fatigue-resistance.[16] The conjugation backbones of two isomers are reversibly switched by the photoirradiation of appropriate wavelength. From the view point of the conjugation backbone, when bias voltage was applied to two

isomers, these would show different tunneling conductances in the low bias region. In addition, the open-ring isomer has lower HOMO level and higher LUMO level than those of closed-ring isomers.[17] This relationship of these frontier energy levels associates us diarylethene also performs as a conductance switch in term of resonance tunneling mechanism. Some reports on the switching behavior of conductance of diarylethenes are summarized in Figure 5.[18-28] Besides diarylethenes, conductance photoswitching behavior of other photochromic molecules, such as azobenzenes,[29,30] stylbene[31] and dihydroazulene/vinylheptafulvene,[32] are reported.

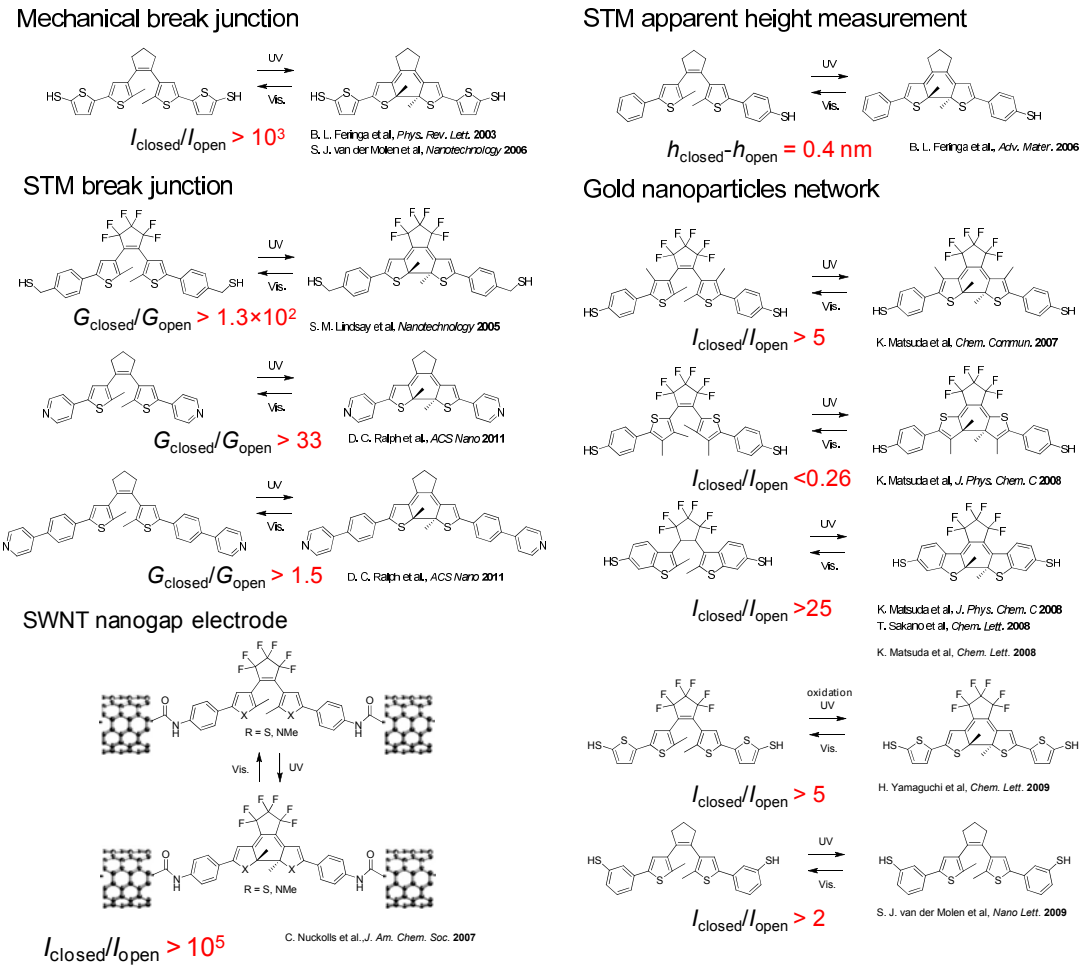

Figure 5. Summary of conductance switching of diarylethenes.[18-28] G_{closed}/G_{open} and I_{closed}/I_{open} denote the conductance ratio and current ratio between open- and closed-ring isomers, respectively. h_{closed} and h_{open} denote the apparent heights of these isomers.

4. Self-assemblies at the liquid-solid interface

4.1 General

Supramolecular organization on the two-dimensional (2-D) surface is the subject of intensive research because it potentially allows the formation of functional surfaces, including the development of prototypes of future molecule-based electronic devices.[33-35] Intrinsic self-assembling nature of organic molecules is available to organize the organic molecules on metal surface. In order to prepare the highly ordered molecular ordering on the metal surface, vapor deposition and general coating methods is sometimes inefficient because of yielding the disordered aggregates. The simple drop casting the solution of organic molecules on the highly oriented pyrolytic graphite (HOPG) produces highly ordered SAMs at the liquid-HOPG interface.[36] Solute molecules are stabilized on the graphite surface via van der Waals interaction. An appropriate choice of the solvent species affords a perfect selectivity of adsorbate, that is a less adsorptive solvent yields pure SAMs.[37] The use of the solution enable to prepare the defect free SAMs owing to the adsorption-desorption equilibrium of the solute molecules. This self-healing property is one of advantage of the physisorbed monolayers at the liquid-solid interface.[38] Two-dimensional phase separation is also interesting phenomena at the liquid-solid interface. When several species of molecules are put on the substrate, they form different domains composed of almost pure components. That is because molecules having similar structure tend to assemble to maximize the intermolecular stabilization energy. That enables to apply to the comparison of the molecular conductance by STM measurement.

4.2 Chlonological change of surface ordering at the liquid-solid interface

STM in particular turned out to be extremely useful to probe not only the organization of molecules on a local scale, but also of molecular surface dynamics involved in the self-assembly process and the resulting electronic properties of the surface molecule. Ostwald ripening,[39] which is defined as the growth of the larger domains at the expense of dissolving smaller domains, is considered as intrinsic phenomenon observed in the 2-D structure at the interface. Rabe et al. reported the 2-D Ostwald ripening at the liquid-HOPG interface with 2-hexadecylanthraquinone (Figure 6a).[40] In addition, other studies on the real-time STM analysis are reported. For example, Otsuki et al. reported dynamic rotation of double-decker porphyrins (Figure 6b),[41] De Feyter et al. reported conformational dynamics of six-legged molecules,[42] Fichou et al. reported phase transition of the alkylated hexabenzocoronene on the *n*-pentacontane template,[43] and Flynn et al. reported frustrated Ostwald ripening

of 2-D chiral reorientation of racemic compounds (Figure 6c).[44]

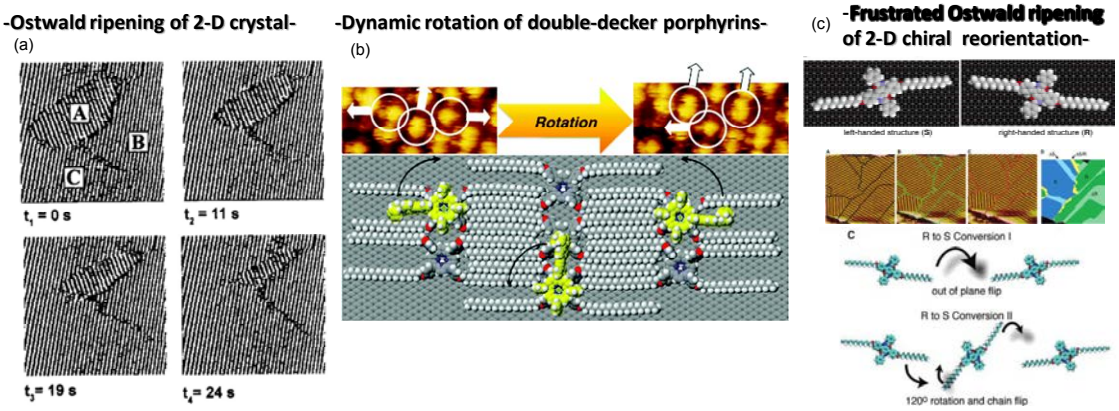

Figure 6. Dynamics of the SAMs at the liquid-HOPG interface analyzed by STM: (a,c) 2-D Ostwald ripening;[40,44] (b) dynamic rotation of porphyrin.[41]

4.3 Controlling the surface ordering by external stimuli

One of the main challenges is the generation of controllable highly organized supramolecular nanostructures by external stimuli. Two-dimensional ordering manners are known to be changed by solvent polarities[45] and chiralities,[46] heating,[47] concentration,[48,49] co-adosorption molecules[50,51] and photoirradiation.[52] Photoirradiation can change or switch the 2-D ordering at the liquid-solid interface. Adsorption-desorption equilibrium helps to replace the surface molecules to large amount of molecules in solution phase. Some investigations of the reversible switching of surface ordering by using photochromic molecules are reported (Figure 7).[53-55] When the 2-D orderings of azobenzenes were prepared on the metal surface in the ultra high vacuum (UHV) condition, the ordering manner was not changed by the photoirradiation or electric field. Instead, switching behavior of the *cis-trans* isomerization could be traced by UHV-STM with single molecular resolution.[56-58.]

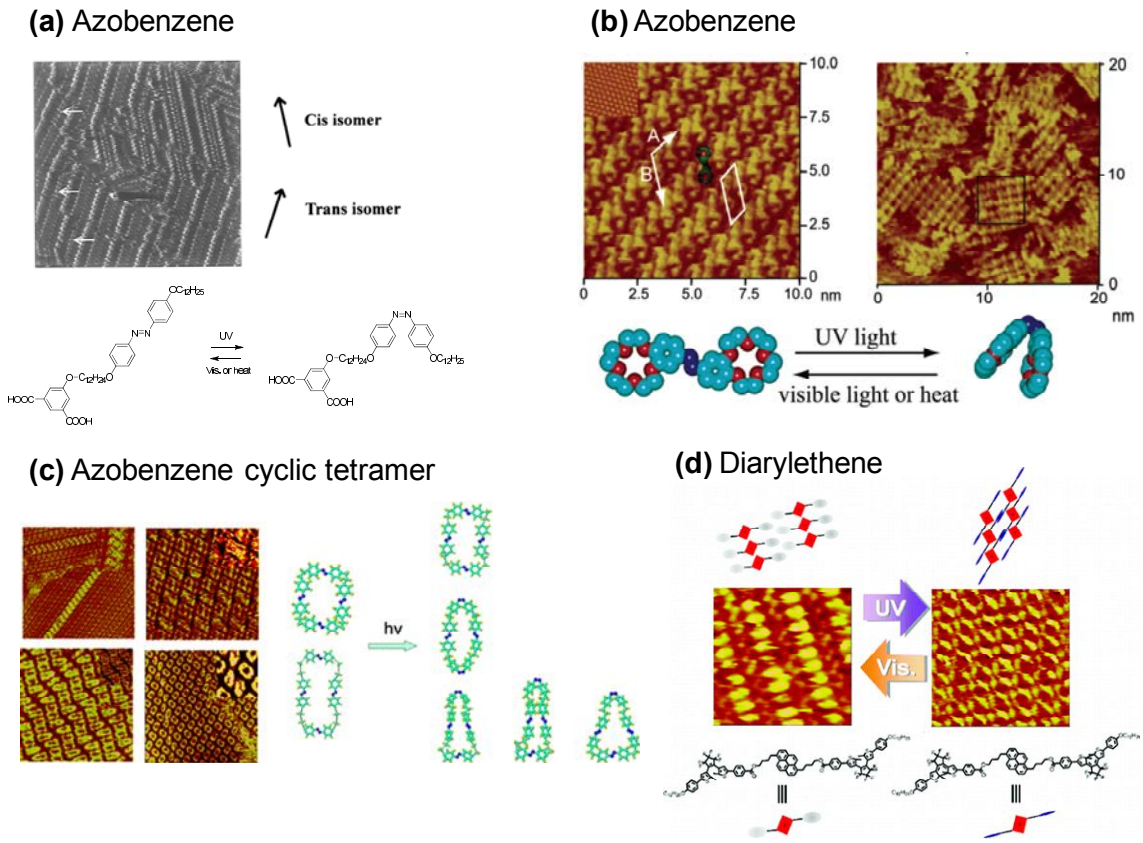

Figure 7. Phase transition of 2-D ordering induced by photo-irradiation at the liquid-solid interface: (a,b) azobenzene derivatives;[53,54] (c) azobenzene cyclic tetramer;[52] (d) diarylethene.[55]

5. Scope of this thesis

In chapters 1 and 2, the relationship between molecular conductance and molecular structure was investigated by using diarylethene-metal nanoparticles network. From these studies, it is revealed that conductance was reversibly switched by the photochromism of interlinked diarylethenes between gold nanoparticles. According to the photoirradiation to the network, conductance of the circuit showed the percolation type behavior.

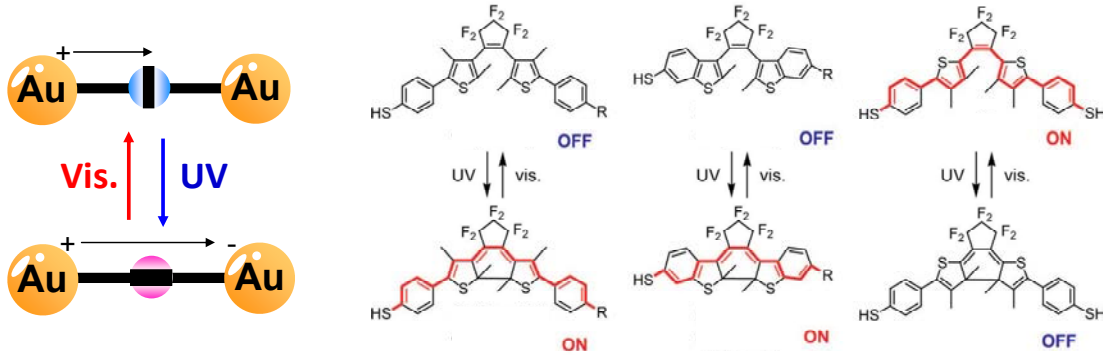

Figure 8. Graphical abstract of chapter 1, entitled "*Conductance photoswitching of diarylethene-gold nanoparticle network induced by photochromic reaction*."

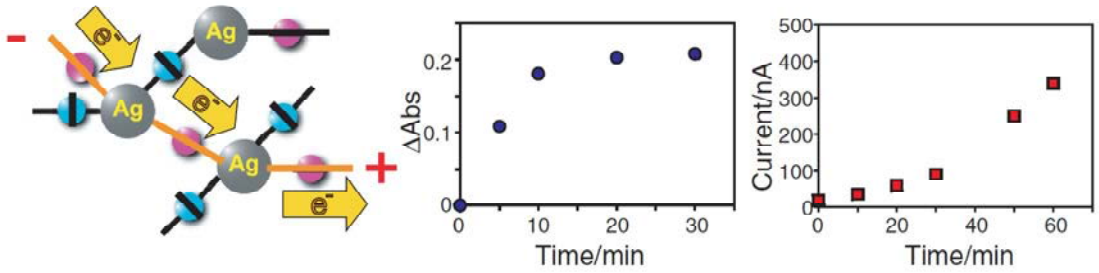

Figure 9. Graphical abstract of chapter 2, entitled "*Percolation-type photoswitching behavior in conductance of diarylethene–silver nanoparticle networks*."

In chapter 3, method for the comparing the molecular conductance by STM was proposed. Two-dimensional phase separation of the template molecules enabled to put the measuring molecules separately on the graphite surface. Operation of this system was confirmed by the planer and twisted phenylpyridines as a reference. This method enabled to statistically analyze the ratio of single molecule conductance with a large number of molecules on the surface.

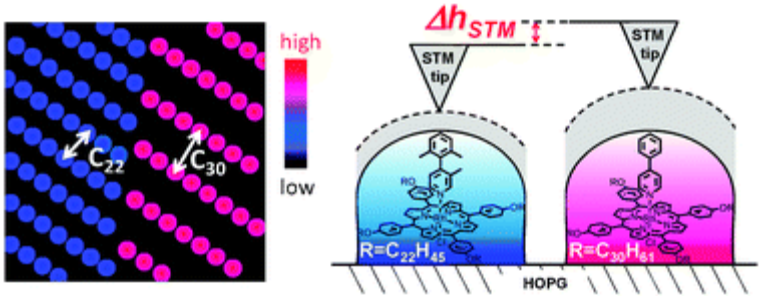

Figure 10. Graphical abstract of chapter 3, entitled "*Comparison of molecular conductance between planar and twisted 4-phenylpyridines by means of two-dimensional phase separation of tetraphenylporphyrin templates at a liquid–HOPG interface*".

In chapter 4, two-dimensional phase transition behavior of porphyrin was analyzed by STM. The alkoxy porphyrin showed phase transition from face-on to edge-on ordering. The chronological change of the ordering was traced to show the existence of several types of Ostwald ripening including two-step phase transition from small edge-on to face-on furthermore to edge-on orderings. While, the *N*-alkylcarbamoyl porphyrin showed persistent edge-on ordering and the ordering was showed Moiré pattern suggesting highly stacked structure. The edge-on orderings have potential application to the charge and energy transfer.

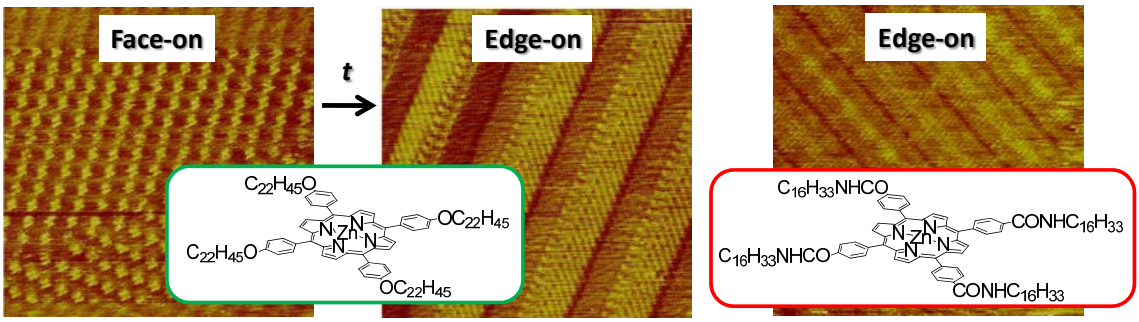

Figure 11. Graphical abstract of chapter 4, entitled "*Chronological change from face-on to edge-on ordering of zinc tetraphenylporphyrin at phenyloctane–highly oriented pyrolytic graphite interface*".

In chapter 5, molecular ordering of photochromic diarylethene was controlled by light. *In-situ* UV irradiation induced photochromic reaction not only in the solution phase but also in the surface ordering. The photo-induced phase transition was

proceeded with keeping the 2-D chirality due to the commensuration of alkyl side chains to HOPG substrate. The transformed ordering by light was different from not only the ordering prepared by open-ring isomer but also that by closed-ring isomer.

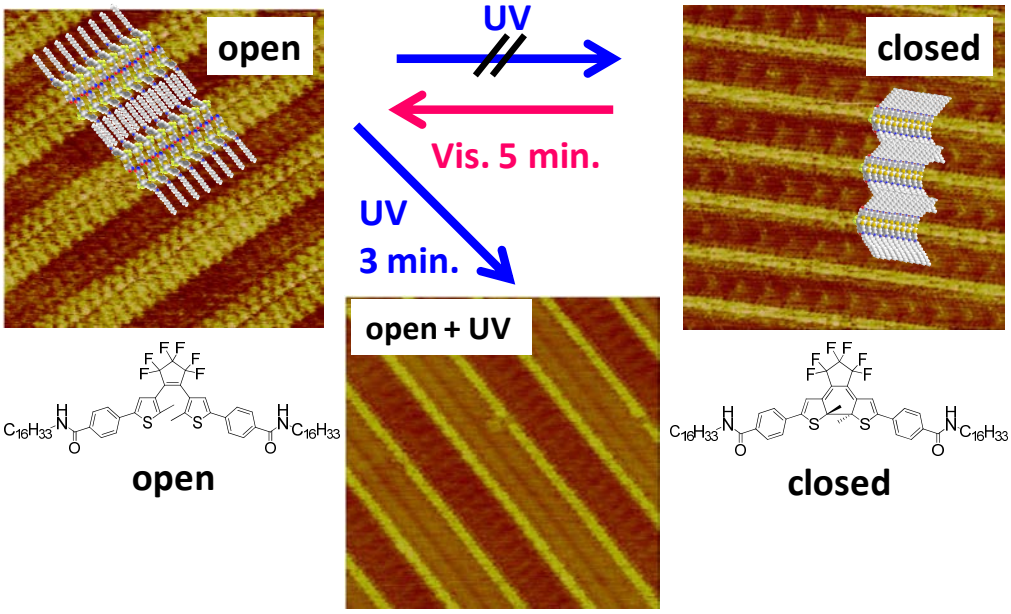

Figure 12. Graphical abstract of chapter 5, entitled "*Preparation of Metastable 2-D Ordering of Diarylethene by Light at the 1-Octanoic Acid-HOPG Interface*".

References

(1) Barth, J. V.; Costantini, G.; Kern, K. *Nature* **2005**, *437*, 671–679.

(2) Born, M.; Wolf, E. *Principles of Optics* (Cambridge Univ. Press, Cambridge, **2002**).

(3) Aviram, A.; Ratner, M. A. *Chem. Phys. Lett.* **1974**, *29*, 277-283.

(4) Binning, G.; Rohrer, H.; Gerber, Ch.; Weibel, E. *Phys. Rev. Lett.* **1982**, *49*, 57–61.

(5) Pomerantz M.; Aviram A.; Mccorkle R. A.; Li L.; Schrott A. G. *Science* **1992**, *255*, 1115–1118.

(6) Reed,M. A.; Zhou, C.; Muller, C. J.; Burgin, T. P.; Tour, J. M. *Science* **1997**, *278*, 252–254.

(7) Love, J. C.; Estroff, L. A.; Kriebel, J. K.; Nuzzo, R. G.; Whitesides, G. M. *Chem. Rev.* **2005**, *105*, 1103–1169.

(8) Xu, B.; Tao, N. J. *Science* **2003**, ***301***, 1221–1223.

(9) Bumm, L. A.; Arnold, J. J.; Dunbar, T. D.; Allara, D. L.; Weiss, P. S. *J. Phys. Chem. B* **1999**, *103*, 8122–8127.

(10) Cui, X. D.; Primak, A.; Zarate, X.; Tomfohr, J.; Sankey, O. F.; Moore, A. L.; Moore, T. A.; Gust, D.; Harris, G.; Lindsay, S. M. *Science* **2001**, *294*, 571–574.

(11) Kushmerick, J. G.; Holt, D. B.; Yang, J. C.; Naciri, J.; Moore, M. H.; Shashidhar, R. *Phys. Rev. Lett.* **2002**, *89*, 086802.

(12) Guo, X.; Small, J. P.; Klare, J. E.; Wang, Y.; Purewal, M. S.; Tam, I. W.; Hong, B. H.; Caldwell, R.; Huang, L.; O'Brien, S.; Yan, J.; Breslow, R.; Wind, S. J.; Hone, J.; Kim, P.; Nuckolls, C. *Science* **2006**, *311*, 356–359.

(13) Choi, S. H.; Kim, B. S.; Frisbie, C. D. *Science* **2008**, *320*, 1482–1486.

(14) (a) Simmons, J. G. *J. Appl. Phys.* **1963**, *34*, 1793–1803. (b) Beebe, J. M.; Kim, B. S.; Gadzuk, J. W.; Frisbie, C. D.; Kushmerick, J. G. *Phys. Rev. Lett.* **2006**, *97*, 026801.

(15) Bouas-Laurent, H.; Dürr, H. *Pure Appl. Chem.* **2001**, *73*, 639–665.

(16) Irie, M. *Chem. Rev.* **2000**, 100, 1685–1716.

(17) Zacharias, P.; Gather, M. C.; Köhnen, A.; Rehmann, N.; Meerholz, K. *Angew. Chem. Int. Ed.* **2009**, *48*, 4038–4041.

(18) (a) Dulić, D; van der Molen, S. J.; Kudernac, T.; Jonkman, H.T.; de Jong, J. J. D.; Bowden, T. N.; van Esch, J.; Feringa, B. L.; Van Wees, B. J. *Phys. Rev. Lett.* **2003**, *91*, 207402. (b) van der Molen, S. J.; Van Der Vegte, H.; Kudernac, T.; Amin, I.; Feringa, B. L.; Van Wees, B. J. *Nanotechnology* **2006**, *17*, 310–314.

(19) He, J.; Chen, F.; Liddell, P. A.; Adréasson, J.; Straight, S. D.; Gust, D.; Moore,

T. A.; Moore, A. L.; Li, J.; Sankey, O. F.; Lindsay, S. M. *Nanotechnology* **2005**, *16*, 695–702.

(20) Tam, E.S.; Parks, J. J.; Shum, W. W.; Zhong, Y.-W.; Santiago-Berríos, M. B.; Zheng, X.; Yang, W.; Chan, G. K. -L.; Abruña, H. D.; Ralph, D. C. *ACS Nano* **2011**, *5*, 5115–5123.

(21) Whalley, A. C.; Steigerwald, M. L.; Guo, X.; Nuckolls, C. *J. Am. Chem. Soc.* **2007**, *129*, 12590–12591.

(22) Katsonis, N.; Kudernac, T.; Walko, M.; Van Der Molen, S. J.; Van Wees, B. J.; Feringa, B. L. *Adv. Mater.* **2006**, *18*, 1397–1400.

(23) Kronemeijer, A. J.; Akkerman, H. B.; Kudernac, T.; Van Wees, B. J.; Feringa, B. L.; Blom P. W. M.; De Boer, B. *Adv. Mater.* **2008**, *20*, 1467–1473.

(24) Ikeda, M.; Tanifuji, N.; Yamaguchi, H.; Irie, M.; Matsuda, K. *Chem. Commun.* **2007**, 1355–1357.

(25) Matsuda, K.; Yamaguchi, H.; Sakano, T.; Ikeda, M.; Tanifuji, N.; Irie, M. *J. Phys. Chem. C* **2008**, *112*, 17005–17010.

(26) Sakano, T.; Yamaguchi, H.; Tanifuji, N.; Irie, M.; Matsuda, K. *Chem. Lett.* **2008**, *37*, 634–635.

(27) Yamaguchi, H.; Matsuda, K. *Chem. Lett.* **2009**, *38*, 946–947.

(28) Van Der Molen, S. J.; Liao, J.; Kudernac, T.; Agustsson, J. S.; Bernard, L.; Calame, M.; Van Wees, B. J.; Feringa, B. L.; Schönenberger, C. *Nano Lett.* **2009**, *9*, 76–80.

(29) Mativetsky, J. M.; Pace, G.; Elbing, M.; Rampi, M. A.; Mayor, M.; Samorì, P. *J. Am. Chem. Soc.* **2008**, *130*, 9192–9193.

(30) Ferri V.; Elbing M.; Pace G.; Dickey M. D.; Zharnikov M.; Samor P.; Mayor M.; Rampi M. A. *Angew. Chem. Int. Ed.* **2008**, *47*, 3407–3409.

(31) Martin, S.; Haiss, W.; Higgins, S. J.; Nichols, R. J. *Nano Lett.* **2010**, *10*, 2019–2023.

(32) Lara-Avila, S.; Danilov, A. V.; Kubatkin, S. E.; Broman, S.L.; Parker, C. R.; Nielsen, M. B. *J. Phys. Chem. C* **2011**, *115*, 18372–18377.

(33) Lehn, J.-M. *Proc. Natl. Acad. Sci. USA* **2002**, *99*, 4763–4768.

(34) Barth, V.; Costantini, G.; Kern, K. *Nature* **2005**, *437*, 671–679.

(35) Müllen, K.; Rabe, J. P. *Acc. Chem. Res.* **2008**, *41*, 511–520.

(36) Elemans, J.; Lei, S. B.; De Feyter, S. *Angew. Chem., Int. Ed.* **2009**, *48*, 7298–7333.

(37) Yang, Y.; Wang, C. *Curr. Opin. Colloid* **2009**, *14*, 135– 147.

(38) Samorí, P.; Müllen, K.; Rabe, J. P. *Adv. Mater.* **2004**, *16*, 1761.

(39) Ostwald, W. Z. *Phys. Chem.* **1900**, *34*, 495.

(40) Stabel, A.; Heinz, R.; De Schryver, F. C.; Rabe, J. P. *J. Phys. Chem.* **1995**, *99*, 505–507.

(41) Otsuki, J.; Komatsu, Y.; Kobayashi, D.; Asakawa, M.; Miyake, K. *J. Am. Chem. Soc.* **2010**, *132*, 6870–6871.

(42) Xu, H.; Minoia, A.; Tomović, Ž.; Lazzaroni, R.; Meijer, E. W.; Schenning, A. P. H. J. ; De Feyter, S. *ACS Nano* **2009**, *3*, 1016–1024.

(43) Piot, L.; Marchenko, A.; Wu, J.; Müllen, K.; Fichou, D. *J. Am. Chem. Soc.* **2005**, *127*, 16245–16250.

(44) Florio, G. M.; Klare, J. E.; Pasamba, M. O.; Werblowsky, T. L.; Hyers, M.; Berne, B. J.; Hybertsen, M. S.; Nuckolls, C.; Flynn, G. W. *Langmuir* **2006**, *22*, 10003–10008.

(45) Liu, J.; Zhang, X.; Yan, H. J.; Wang, D.; Wang, J. Y.; Pei, J.; Wan, L. J. *Langmuir* **2010**, *26*, 8195–8200.

(46) Katsonis, N.; Xu, H.; Haak, R. M.; Kudernac, T.; Tomovic, Z.; George, S.; Van der Auweraer, M.; Schenning, A. P. H. J.; Meijer, E. W.; Feringa, B. L.; De Feyter, S. *Angew. Chem., Int. Ed.* **2008**, *47*, 4997–5001.

(47) Rohde, D.; Yan, C. J.; Yan, H. J.; Wan, L. J. *Angew. Chem., Int. Ed.* **2006**, *45*, 3996–4000.

(48) Tahara, K.; Okuhata, S.; Adisoejoso, J.; Lei, S.; Fujita, T.; de Feyter, S.; Tobe, Y. *J. Am. Chem. Soc.* **2009**, *131*, 17583–17590.

(49) Ha, N. Thi Ngoc; Gopakumar, T. G.; Hietschold, M. *J. Phys. Chem. C* **2011**, *115*, 21743–21749.

(50) Guan, C.-Z.; Chen, T.; Wu, J.-Y.; Chen, Q.; Wang, D.; Stang, P. J.; Wan, L.-J. *Langmuir* **2011**, *27*, 9994–9999.

(51) Zhang, X.; Chen, T.; Chen, Q.; Deng, G. J.; Fan, Q. H.; Wan, L. J. *Chem. Eur. J.* **2009**, *15*, 9669–9673.

(52) Shen, Y. T.; Guan, L.; Zhu, X. Y.; Zeng, Q. D.; Wang, C. *J. Am. Chem. Soc.* **2009**, *131*, 6174–6180.

(53) Vanoppen, P.; Grim, P. C. M.; Ru1cker, M.; De Feyter, S.; Moessner, G.; Valiyaveettil, S.; Mü1llen, K.; De Schryver, F. C. *J. Phys. Chem.* **1996**, *100*, 19636–19641.

(54) Xu, L.-P.; Wan, L.-J. *J. Phys. Chem. B* **2006**, *110*, 3185–3188.

(55) Arai, R.; Uemura, S.; Irie, M.; Matsuda, K. *J. Am. Chem. Soc.* **2008**, *130*, 9371–9379.

(56) Alemani, M.; Peters, M. V.; Hecht, S.; Rieder, K. H.; Moresco, F.; Grill, L. *J. Am. Chem. Soc.* **2006**, *128*, 14446–14447.

(57) Dri, C.; Peters, M. V.; Schwarz, J.; Hecht, S.; Grill, L. *Nat. Nanotechnol.* **2008**, *3*, 649–653.

(58) Comstock, M. J.; Levy, N.; Kirakosian, A.; Cho, J. W.; Lauterwasser, F.; Harvey, J. H.; Strubbe, D. A.; Frechet, J. M. J.; Trauner, D.; Louie, S. G.; Crommie, M. F. *Phys. Rev. Lett.* **2007**, *99*, 038301.

Chapter 1

Conductance Photoswitching of Diarylethene-Gold Nanoparticle Network Induced by Photochromic Reaction

Abstract

The relationship between molecular conductance and molecular structure is an important issue in molecular electronics. Photochromic molecules can interconvert their molecular structures by light, so that the molecular conductance should be photocontrolled. According to this strategy the networks composed of photochromic diarylethene dithiols and gold nanoparticles were prepared, and the photochemical reactivity and photoswitching of the conductance were studied. The networks showed a completely reversible photoswitching of the conductance according to the photochromic reactions of the diarylethene units. The switching behavior is attributed to the change of the π-conjugation length of the molecule. Because of the high switching ratio and good reversibility this switching system opens up the possibility of sophisticated molecular electric circuits.

This work has been presented in *J. Phys. Chem. C* **2008**, *112*, 17005-17010, essentially in the same form.

Introduction

The control of molecular conductance by controlling molecular structure is a key issue in molecular electronics.[1] Several approaches are proposed for measurement of the molecular conductance regulated by the molecular structure.[2] The relationship between the structure and the conductance has started to be unveiled.[3] Among them, the network prepared with organic molecules and gold nanoparticles is of increasing interest because of the relatively easy preparation and the applicability to a small number of molecules.[4] Besides, a reversible photoinduced molecular structural change, which is called photochromism, provides photochemically interconvertible isomers.[5] Therefore, photochromic molecules are promising candidates for the molecular-scale digital photoswitching units. Photochromic molecules, which are incorporated in the gold nanoparticle network, are considered to photoswitch the molecular-scale electric circuits.

Diarylethenes undergo photochromic reactions between the hexatriene-type open-ring isomer and cyclohexadiene-type closed-ring isomer by irradiation with UV and visible light.[6] Photoisomerization of the diarylethene unit is known to bring about switching of the π-conjugated system, which gives rise to the change of the magnetic exchange interaction more than 150-fold.[7] The exchange interaction between spins can be considered as an analogue of the electric current between electrodes because both the exchange interaction[8] and the tunneling current[9] show an exponential decrease on the distance. Molecular conductance is expected to be switched by the photochromism of diarylethene.

Although there are some reports on the conductance of the single molecules, studies on the photoswitchable molecule are rare.[10] Here we report on the conductance photoswitching in the network composed of photochromic diarylethenes and gold nanoparticles. The network showed completely reversible photoswitching of the conductance according to the photochromic reactions of the diarylethene units. When 2-thienyl-type diarylethene was used the reversed switching behavior was observed. The switching behavior is attributed to the change of the π-conjugation length of the molecule.

Results and Discussion

Molecular Design and Synthesis.

We take an approach to use gold nanoparticles to bridge diarylethene molecules

with two thiol units and make a conducting path between the interdigitated nanogapped gold electrodes (Figure 1). Because the excited state of the organic molecule on noble metal surface is known to be easily quenched by the surface plasmon resonance,[11] the photoswitching unit should be placed distant from the surface. On the other hand, considering that a conjugated molecule has much better conductance than a nonconjugated molecule,[12] the sulfur atom should be attached directly to the π-conjugated system.

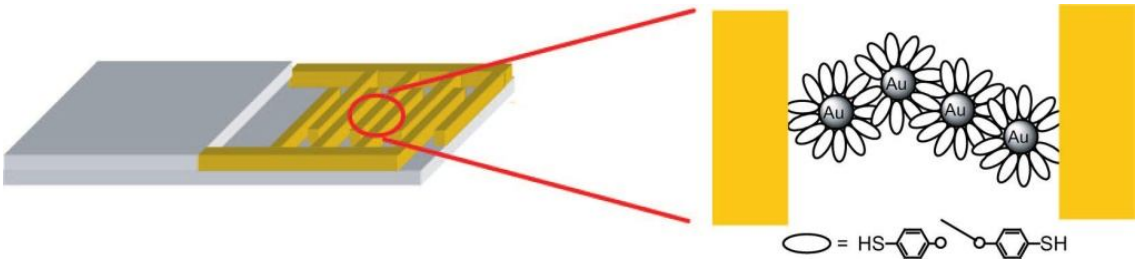

Figure 1. Schematic drawing of a diarylethene-gold nanoparticle network. The diarylethene dithiols bridge the gold nanoparticles and make a network between nanogapped interdigitated gold electrodes. Diarylethene molecules and gold nanoparticles make a conducting path between the electrodes.

On the basis of above points, five diarylethene thiols **1a-5a** have been designed and synthesized (Figure 2). The parent compound of **2a**, 1,2-bis-(2-methyl-benzothiophen-3-yl)hexafluorocyclopentene, has a cycloreversion quantum yield of 0.35, which is 23 times larger than 1,2-bis(2,4-dimethyl-5-phenyl-3-thienyl)hexafluorocyclopentene that is the parent compound of **1a**.[13] The preliminary study on **1a** revealed that the cycloreversion reaction of **Au-1a** nanoparticle network is strongly suppressed and that the switching is not completely reversible.[14] Due to the high cycloreversion quantum yield, **2a** is expected to show efficient reversible switching behavior.[15]

In diarylethene **3a** thiophene rings are connected to the ethene moiety at the 2 position, while in **1a** and **2a** thiophene rings are connected at the 3 position. The open-ring isomer **3a** has a delocalized π conjugation, and oppositely in the closed-ring isomer **3b** the π conjugation is disconnected by the sp^3 carbon at the reactive center.[16] Therefore, when using diarylethene **3a** the switching behavior is expected to be reversed

in comparison with **1a** and **2a**. Diarylethenes **4a** and **5a**, having only one thiol group, were also prepared as reference compounds. Synthesis of diarylethenes was performed by the standard organic synthesis procedure using trimethylsilylethyl protecting group.[17]

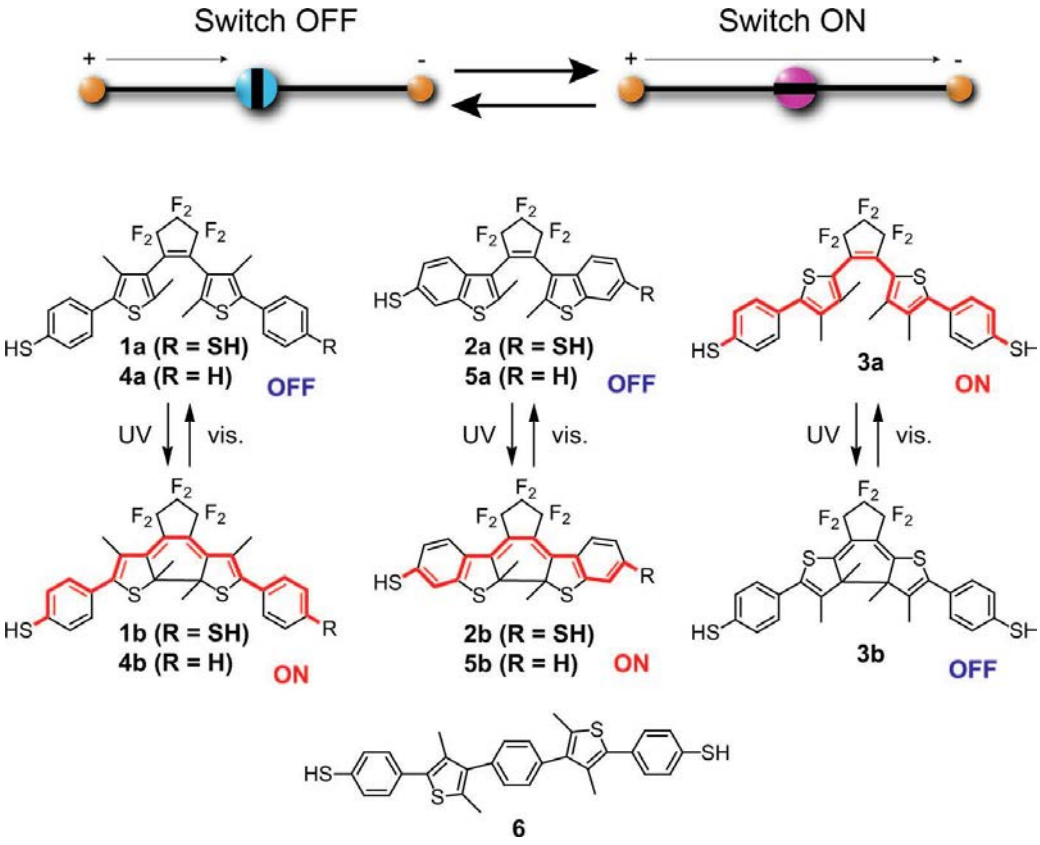

Figure 2. Photochromic reactions of diarylethene thiols as switching units of conductance. The open-ring isomer (**1a-5a**) converts to the closedring isomer (**1b-5b**) by irradiation with UV light and converts back by irradiation with visible light. Compound **6** is a nonphotoreactive reference.

Photochemical Characterization.

Photochromism of diarylethenes on the gold nanoparticles was investigated using discrete nanoparticles capped with diarylethenes **4a** and **5a**. Gold nanoparticles were prepared according to the Brust's method.[18] IR measurement showed incorporation of the diarylethenes in the nanoparticles.[19] TEM measurement revealed formation of nanoparticles with an average diameter of 3-6 nm.[20] The absorption spectral changes of **Au-4a** and **Au-5a** are shown in Figure 3. The absorption maxima of the closed-ring isomers, obtained from the difference spectrum before and after UV irradiation, are

located at 609 and 550 nm for **Au-4b** and **Au-5b**, respectively. A significant bathochromic shift was observed in comparison with the absorption maxima of free diarylethenes **4b** and **5b**, which are located at 577 and 533 nm, respectively. This indicates that the electronic structure of the closed-ring isomer is perturbed by the gold surface.[14] The photoreactivity was suppressed by the presence of the gold surface. Although the previously reported diarylethene-gold nanoparticles with pentamethylene spacer showed only moderate quenching of the excited state,[21] diarylethene-gold nanoparticles **Au-4a** and **Au-5a** showed much severe quenching. This is attributed to the direct connection of the π-conjugated system to the gold surface. Fortunately, the reaction took place in spite of the quenching. The moderate quantum yields of the cyclization/cycloreversion reaction are responsible for the reversible photochromic behavior of these systems.[22]

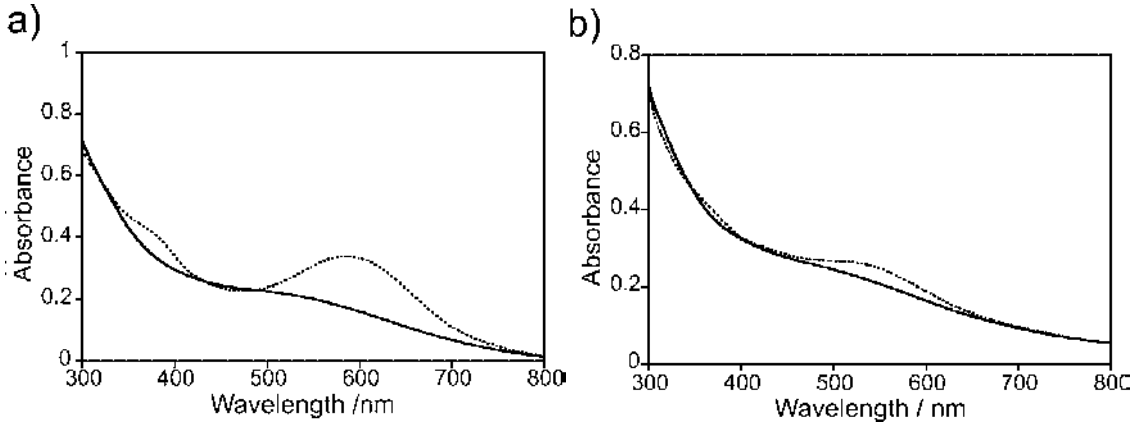

Figure 3. Absorption spectral changes of gold nanoparticles capped with diarylethenes: (a) **Au-4a** and (b) **Au-5a**. Solid lines indicate the spectra before irradiation. Dotted lines indicate the spectra in the photostationary state under irradiation with 313 nm light. Ethyl acetate was used for solvent for **Au-4a**, and toluene was used for **Au-5a**.

Preparation of the Gold Nanoparticle Network.

Preparation of the gold nanoparticle network has been carried out for diarylethene dithiols **1a-3a**. The gold nanoparticles protected by tetraoctylammonium bromide (TOAB) were first prepared, and then the dithiol was reacted with TOAB-protected gold nanoparticles. In this method, formation of the nanoparticles occurred before reaction with the dithiol, so that the size and shape of the nanoparticles could be controlled and aggregation of the nanoparticles could be avoided.[23] The absorption maximum of the closed-ring isomer in the gold nanoparticle network showed

a significant bathochromic shift, suggesting interaction between the chromophore and the gold surface.[14]

The diarylethene-gold nanoparticle networks underwent photochromic reactions except for the **Au-3a** nanoparticle network, which did not undergo the cyclization reaction by irradiation with UV light (Figure S4, Supporting Information). However, the gold nanoparticle network **Au-3b**, which is prepared from the separated closed-ring isomer **3b** in the dark, showed the cycloreversion reaction upon irradiation with visible light. Perturbation by the gold surface is considered to suppress the reaction.

The diarylethene-gold nanoparticle networks were characterized using TEM and SEM (Figure 4). A TEM image of **Au-2a** nanoparticle network shows the existence of the extended network. The average diameter of each particle was 5.0 ± 1.1 nm. A SEM image of the network on the interdigitated nanogapped gold electrode (5 μm) shows that the network bridges the electrodes. The aggregate of the gold nanoparticle network was observed as a white sphere.[4c] The EDX elemental analysis showed that the content of carbon in the network was 28.6%, which is clearly larger than that in the empty gap (10.5%). This indicates that the diarylethenes are incorporated in the network between electrodes.

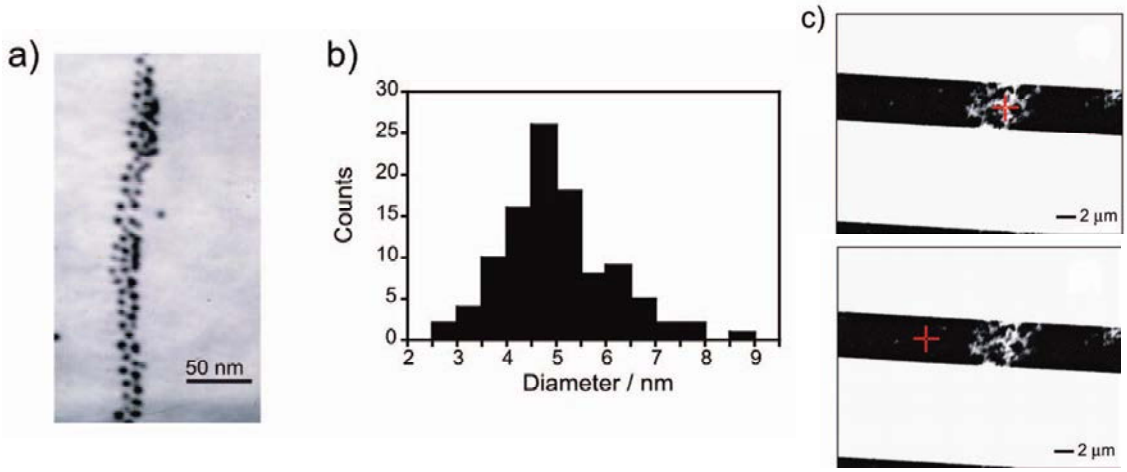

Figure 4. TEM and SEM images of **Au-2a** nanoparticle network. (a) TEM image of **Au-2a** nanoparticle network. (b) Histogram of the size of the nanoparticles in **Au-2a** nanoparticle network. (c) SEM images of **Au-2a** nanoparticle network on an interdigitated gold electrode. White part represents gold electrodes and gold nanoparticle network. Red cross sign indicates the place where EDX was measured.

Photoswitching of Conductance.

Conductance was measured along with the alternate irradiation with UV and visible light (Figure 5). For **Au-1a** and **Au-2a**, upon irradiation with UV light the conductance increased significantly and then by irradiation with visible light the conductance decreased. The photocycloreversion reaction of Au-1a nanoparticle network was very slow. Even after 56 h irradiation with visible light the conductance decreased only 18%.[14] On the contrary, the cycloreversion reaction of **Au-2a** completed in 8 h and the system showed reversible photoswitching behavior. The maximum ON/OFF ratio of the conductance was 25-fold for **Au-2a**. Because **2a** has high quantum yields of both cyclization and cycloreversion reactions, complete reversibility has been achieved.

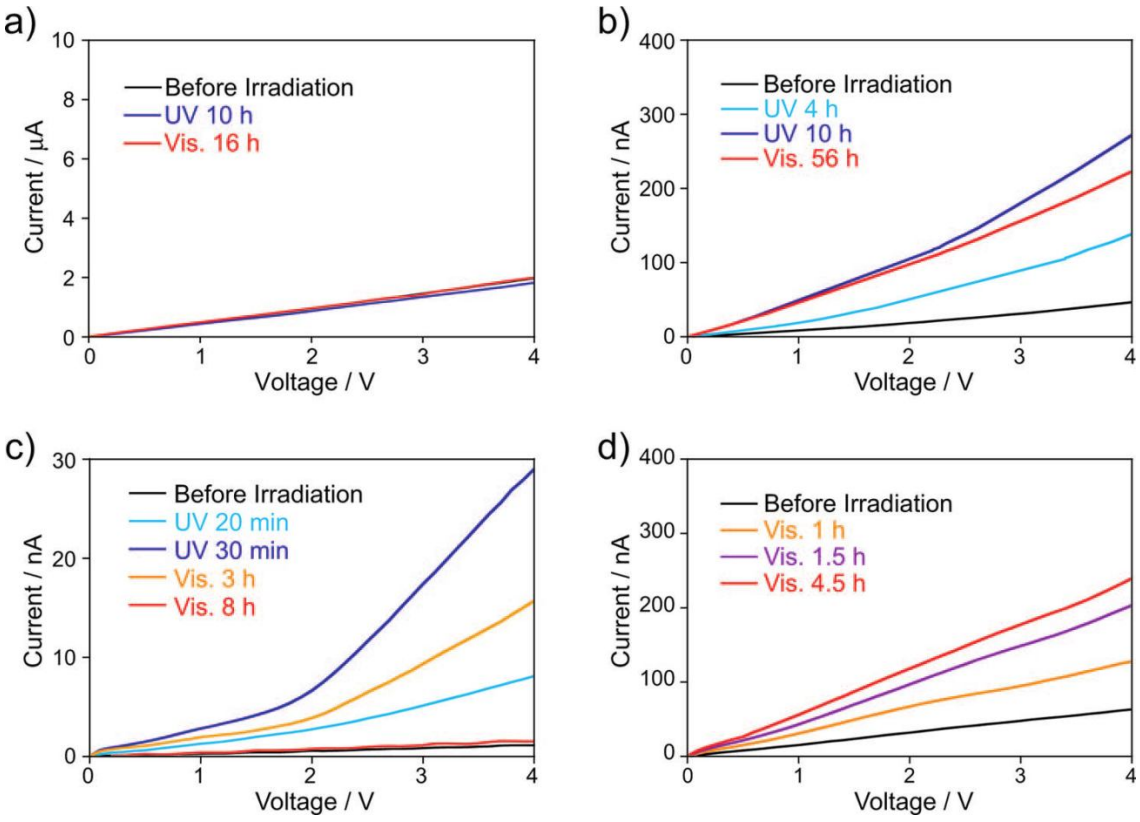

Figure 5. Changes of the I-V curves of diarylethene-gold nanoparticle networks: (a) **Au-6**, (b) **Au-1a**, (c) **Au-2a**, and (d) **Au-3b**. Measurement was carried out at different stages of photoreaction. For the open-ring isomer nanoparticle networks Au-1a and **Au-2a** initially UV light was irradiated and then visible light was irradiated. For the closed-ring isomer nanoparticle network Au-3b only visible irradiation was performed.

To confirm the origin of the switching is the photochromism of the diarylethene unit, 2-thienyl-type diarylethene 3, which has an opposite direction of switching of the π-conjugated system, was investigated. Diarylethene **3** is considered to show the opposite behavior to 3-thienyl-type diarylethene **1** and **2**. For **Au-3b** nanoparticle network, upon irradiation with visible (470 nm < λ) light, the conductance increased. The maximum ON/OFF ratio was 3.8-fold. The nonphotoreactive reference **Au-6** nanoparticle network did not show any change upon photoirradiation. Because nonphotoreactive molecule **6** did not show any photoinduced conductance change and 2-thienyl-type diarylethene **3** showed the opposite behavior, the switching behavior is not a trivial effect of the organic molecule and gold nanoparticles but the switching of the diarylethene plays an essential role in the control of the conductance.

Conclusions

We demonstrated the conductance photoswitching of the diarylethene-gold nanoparticle network on the basis of the topology photoswitching of the π conjugation in diarylethene molecules. The system reported here can be extended into a more integrated system, such as an information processing system when the precise control of the network structure is possible because a gold nanoparticle can be used as a branching unit of a network.

Experimental Section

1. Materials.

^{1}H NMR spectra were recorded on a Bruker AVANCE 400 instrument. Mass spectra were obtained on a JEOL JMS-GCmateII. All reactions were monitored by thinlayer chromatography carried out on 0.2 mm E. Merck silica gel plates (60F-254). Column chromatography was performed on silica gel (Kanto, 63-210 mesh). Ultrapure water (>18 MΩ· cm) was obtained by a Millipore SimpliLab. Syntheses of **1a**, **4a**, and **6** have already been reported.14 Syntheses of **2a**, **5a**, and **3a** were performed according to Scheme 1.

Scheme 1. Synthesis route of diarylethenes **2a**, **3a** and **5a**.

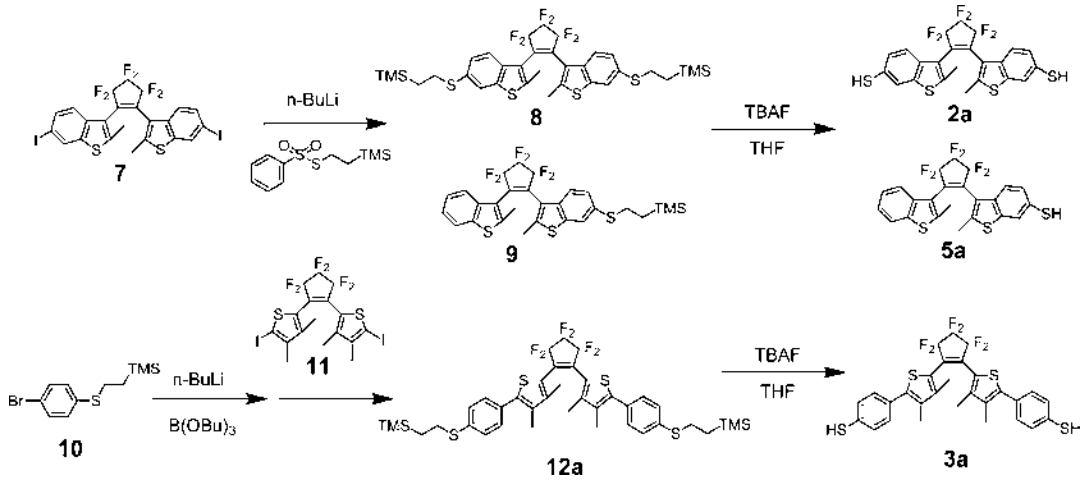

1,2-Bis(2-methyl-6-(2-trimethylsilylethylthio)benzothiophen-3-yl)hexafluorocyclopent-ene (8) and 1-(2-Methyl-6-(2-trimethylsilylethylthio)benzothiophen-3-yl)-2-(2-methylbenzothiophen-3-yl)hexafluorocyclopentene (9).

To a solution of 1,2-bis(2-methyl-6-iodo-benzothiophen-3-yl)hexafluoro-cyclopentene (**7**)[24] (630 mg, 0.87 mmol) in dry THF (100 mL) was added 1.6 M *n*-butyllithium (1.2 mL, 1.9 mmol) at -78 °C under Ar atmosphere, and the reaction mixture was stirred for 30 min. Benzenethiosulfonic acid *S*-(2-trimethylsilylethyl) ester (1.51 g, 5.50 mmol) was added at -78 °C, and the reaction mixture was allowed to warm up to room temperature. After addition of water, the mixture was extracted by diethyl ether. The organic layer was washed with brine, dried with $MgSO_4$, and concentrated. Purification by column chromatography (silica, hexane: $CHCl_3$ = 4:1) gave compound **8** as a colorless oil (250 mg, 39%). Compound **9** was also obtained as a colorless oil (100 mg, 23%). **8**: ^{1}H NMR (400 MHz, $CDCl_3$, TMS) δ 0.04 (s, 18H), 0.86-0.96 (m, 4H), 2.18 (s, 4H), 2.45 (s, 2H), 2.97-3.01 (m, 4H), 7.11-7.62 (m, 6H); HRMS (*m*/*z*) $[M]^+$ calcd for $C_{33}H_{38}F_6S_4Si_2$ 732.1299, found 732.1273. **9**: ^{1}H NMR (400 MHz, $CDCl_3$, TMS) δ 0.04 (s, 9H), 0.83-0.96 (m, 2H), 2.18 (s, 1.9H), 2.20 (s, 1.9H), 2.46 (s, 1.1H), 2.48 (s, 1.1H), 2.88-3.01 (m, 2H), 7.11-7.71 (m, 7H); HRMS (*m*/*z*) $[M]^+$ calcd for $C_{28}H_{26}F_6S_3Si$ 600.0870, found 600.0874.

1,2-Bis(2-methyl-6-mercaptobenzothiophen-3-yl)hexafluorocyclopentene (2a).

To a solution of compound **8** (20 mg, 27 μmol) in dry THF (3 mL) was added 1.0 M tetrabutylammonium fluoride THF solution (0.4 mL, 400 μmol) at N_2 atmosphere, and the mixture was stirred for 10 min at room temperature. After addition of 0.1 M aqueous HCl (7 mL), the mixture was stirred for 10 min. After extraction by diethyl

ether, the organic layer was washed with brine, dried with $MgSO_4$, and concentrated. Purification with HPLC (column Kanto Chemical Mightysil Si60 250-3.0 mm, hexane:EtOAc = 99.5:0.5) gave compound **2a** as a white solid (9 mg, 63%): ^{1}H NMR (400 MHz, $CDCl_3$, TMS) δ 2.16 (s, 3.8H), 2.44 (s, 2.2H), 3.49 (s, 0.8H), 3.56 (s, 1.2H), 7.08-7.50 (m, 6H); HRMS (*m*/*z*) $[M]^+$ calcd for $C_{23}H_{14}F_6S_4$ 531.9882, found 531.9872.

1-(2-Methyl-6-mercaptobenzothiophen-3-yl)-2-(2-methylbenzothiophen-3-yl)hexafluorocyclopentene (5a).

To a solution of compound **9** (10 mg, 17 μmol) in dry THF (3 mL) was added 1.0 M tetrabutylammonium fluoride THF solution (0.3 mL, 300 μmol) at N_2 atmosphere, and the mixture was stirred for 10 min at room temperature. After addition of 0.1 M aqueous HCl (4 mL), the mixture was stirred for 10 min. After extraction by diethyl ether, the organic layer was washed with brine, dried with $MgSO_4$, and concentrated. Purification with column chromatography (silica, hexane:$CHCl_3$ = 5:2) gave compound **6** as a white solid (7 mg, 84%): ^{1}H NMR (400 MHz, $CDCl_3$, TMS) δ 2.17 (s, 1.9H), 2.20 (s, 1.9H), 2.46 (s, 1.1H), 2.47 (s, 1.1H), 3.46 (s, 0.4H), 3.55(s, 0.6H), 7.15-7.71 (m, 7H); HRMS (*m*/*z*) $[M]^+$ calcd for $C_{23}H_{14}F_6S_3$ 500.0162, found 500.0156.

1,2-Bis(3,4-dimethyl-5-(4-mercaptophenyl)-2-thienyl)hexafluorocyclopentene (3a).

To a solution of 4-(2-trimethylsilylethyl) thiobromobenzene **10**[25] (270 mg, 0.93 mmol) in dry THF (7 mL) was added 1.6 M *n*-butyllithium (0.63 mL, 1 mmol) at -78 °C under N_2 atmosphere, and the mixture was stirred for 15 min. Tributyl borate (350 μL, 1.1 mmol) was added, and the mixture was allowed to warm up to room temperature. The reaction was quenched by adding water. Then, after addition of 1,2-bis(5-iodo-3,4-dimethyl-2-thienyl)hexafluorocyclopentene 1116 (150 mg, 0.24 mmol), $Pd(PPh_3)_4$ (25 mg, 21 μmol), and aqueous Na_2CO_3 (20 wt %, 5 mL), the reaction mixture was refluxed for 24 h. The reaction mixture was extracted by diethyl ether, and the organic layer was washed with brine, dried with $MgSO_4$, and concentrated. Purification by column chromatography (silica, hexane:$CHCl_3$ = 10:1 to 4:1) followed by GPC ($CHCl_3$) gave compound **12a** (142 mg, 74%) as a yellow oil: ^{1}H NMR (400 MHz, $CDCl_3$, TMS) δ 0.06 (s, 18H), 0.94-0.98 (m, 4H), 1.73 (s, 6H), 2.13 (s, 6H), 2.98-3.02 (m, 4H), 7.31-7.37 (m, 8H); HRMS (*m*/*z*) $[M]^+$ calcd for $C_{39}H_{46}F_6S_4Si_2$ 812.1925, found 812.1927. Closed-ring isomer **12b** was separated by HPLC (column, Kanto Chemical Mightysil Si60 250-4.6 mm; eluent, hexane: CH_2Cl_2 = 90:10) from the UV-irradiated solution of **12a**. Deprotection of compound **12b** was performed in the dark according to the procedure described above to give dithiol **3b**. Immediately after

deprotection the **Au-3b** nanoparticle network was prepared in the dark by the procedure described above.

Preparation of Diarylethene Dithiol-Gold Nanoparticle Networks.

To a solution of tetrachloroaurate(III) hydrate in ultrapure water (30 mM, 1.0 mL, 30 μmol) was added tetraoctylammonium bromide (35 mg, 64 μmol) in toluene (10 mL). Ultrapure water (3 mL) was added to the reaction mixture, and the solution was vigorously stirred. Then $NaBH_4$ (12 mg, 320 μmol) in ultrapure water (3 mL) was added, and the solution was stirred for 3 h to give TOAB-protected gold nanoparticles. One drop (50 μL) of the solution of dithiol **2a** (prepared from 10 mg of the protected dithiol) in toluene (0.25 mL) was mixed with one drop (50 μL) of a toluene solution of TOAB-protected gold nanoparticles, prepared from the above procedure, on a interdigitated 5 μm-gapped Au electrode (NTT-AT). The electrode was washed with ethanol and dried in vacuum.

Preparation of Diarylethene Monothiol-Gold Nanoparticles.

To a solution of tetrachloroaurate(III) hydrate in ultrapure water (30 mM, 1.0 mL, 30 μmol) was added tetraoctylammonium bromide (110 mg, 200 μmol) in toluene (10 mL). Compound **5a** (20 mg, 40 μmol) and ultrapure water (10 mL) was added to the solution. After vigorous stirring, $NaBH_4$ (23 mg, 610 μmol) in ultrapure water (2 mL) was added to the reaction mixture and again the solution was stirred for 3 h. The organic layer was separated and concentrated. The residue was washed by methanol to give **Au-5a** nanoparticles. The sample was kept in toluene solution.

2. TEM and SEM Measurements.

TEM measurement was performed on a Hitachi H-7500 instrument. The measurement was performed at 100 kV. TEM samples were prepared by placing a drop of toluene solution on carbon-coated copper grid. SEM measurement was performed on a Shimadzu SS-550 instrument. The measurement was performed at 15 kV. SEM samples were prepared by gold coating using a Sanyu SC-701 quick coater. Photochemical Measurement. Absorption spectra were measured on a HITACHI U-3500 spectrophotometer. IR spectra were measured on a Perkin-Elmer Spectrum One instrument by ATR method. Photoirradiation was carried out using a USHIO 500 W super high pressure mercury lamp or a Hamamatsu 200W mercury-xenon lamp with a combination optical filter and monochromator (Ritsu MC-10N).

3. Conductance Measurement.

Conductance measurement was performed by a remote source meter (Keithley model 6430) equipped with a preamplifier and an interdigitated gold electrode. The electrode and preamplifier were covered with stainless wire net. The cyclization reaction was performed using UV light (290 nm < λ < 400 nm, 85 mW/cm^2). The cycloreversion reaction was performed using visible light (560 nm < λ) for **Au-1**, **Au-4**, and **6** and visible light (470 nm < λ) for **Au-2**, **Au-3**, and **Au-5**.

References and Notes

(1) (a) Joachim, C.; Gimzewski, J. K.; Aviram, A. *Nature* **2000**, *408*, 541–548. (b) Carroll, R. L.; Gorman, C. B. *Angew. Chem., Int. Ed.* **2002**, *41*, 4378–4400. (c) Metzger, R. M. *Chem. Rev.* **2003**, *103*, 3803–3834.

(2) (a) Bumm, L. A.; Arnold, J. J.; Cygan, M. T.; Dunbar, T. D.; Burgin, T. P.; Jones, L., II; Allara, D. L.; Tour, J. M.; Weiss, P. S. *Science* **1996**, *271*, 1705–1707. (b) Reed, M. A.; Zhou, C.; Muller, C. J.; Burgin, T. P.; Tour, J. M. *Science* **1997**, *278*, 252–254. (c) Cui, X. D.; Primak, A.; Zarate, X.; Tomfohr, J.; Sankey, O. F.; Moore, A. L.; Moore, T. A.; Gust, D.; Harris, G.; Lindsay, S. M. *Science* **2001**, *294*, 571–574. (d) Xu, B.; Tao, N. J. *Science* **2003**, *301*, 1221–1223. (e) Guo, X.; Small, J. P.; Klare, J. E.; Wang, Y.; Purewal, M. S.; Tam, I. W.; Hong, B. H.; Caldwell, R.; Huang, L.; O'Brien, S.; Yan, J.; Breslow, R.; Wind, S. J.; Hone, J.; Kim, P.; Nuckolls, C. *Science* **2006**, *311*, 356–359.

(3) (a) Donhauser, Z. J.; Mantooth, B. A.; Kelly, K. F.; Bumm, L. A.; Monnell, J. D.; Stapleton, J. J.; Price, D. W., Jr.; Rawlett, A. M.; Allara, D. L.; Tour, J. M.; Weiss, P. S. Science 2001, 292, 2303–2307. (b) Xiao, X.; Xu, B.; Tao, N. J. *J. Am. Chem. Soc.* **2004**, 126, 5370–5371. (c) Venkataraman, L.; Klare, J. E.; Nuckolls, C.; Hybertsen, M. S.; Steigerwald, M. L. *Nature* **2006**, 442, 904–907.

(4) (a) Ogawa, T.; Kobayashi, K.; Masuda, G.; Takase, T.; Maeda, S. *Thin Solid Films* **2001**, *393*, 374–378. (b) Shigi, H.; Tokonami, S.; Yakabe, H.; Nagaoka, T. *J. Am. Chem. Soc.* **2005**, *127*, 3280–3281. (c) Taniguchi, S.-i.; Minamoto, M.; Matsushita, M. M.; Sugawara, T.; Kawada, Y.; Bethell, D. *J. Mater. Chem.* **2006**, *16*, 3459–3465. (d) Bernard, L.; Kamdzhilov, Y.; Calame, M.; van der Molen, S. J.; Liao, J.; Scho¨nenberger, C. *J. Phys. Chem. C* **2007**, *111*, 18445.

(5) Molecular Switches; Feringa, B. L., Ed.; Wiley-VCH: Weinheim, Germany, **2001**.

(6) Irie, M. *Chem. Rev.* **2000**, *100*, 1685–1716.

(7) (a) Matsuda, K. *Bull. Chem. Soc. Jpn.* **2005**, *78*, 383–392. (b) Matsuda, K.; Irie, M. *J. Am. Chem. Soc.* **2000**, *122*, 8309–8310. (c) Matsuda, K.; Irie, M. *Chem. Eur. J.* **2001**, *7*, 3466–3473. (d) Matsuda, K.; Matsuo, M.; Irie, M. *J. Org. Chem.* **2001**, *66*, 8799–8803. (e) Matsuda, K.; Matsuo, M.; Mizoguti, S.; Higashiguchi, K.; Irie, M. *J. Phys. Chem. B* **2002**, *106*, 11218–11225. (f) Takayama, K.; Matsuda, K.; Irie, M. *Chem. Eur. J.* **2003**, *9*, 5605–5609. (g) Tanifuji, N.; Irie, M.; Matsuda, K. *J. Am. Chem. Soc.* **2005**, *127*, 13344–13353.

(8) Pardo, E.; Faus, J.; Julve, M.; Lloret, F.; Mun˜oz, M. C.; Cano, J.; Ottenwaelder, X.; Journaux, Y.; Carrasco, R.; Blay, G.; Ferna´ndez, I.;

Ruiz-Garcı´a, R. *J. Am. Chem. Soc.* **2003**, *125*, 10770–10771.

(9) Xiao, X.; Xu, B.; Tao, N. J. *Nano Lett.* **2003**, *301*, 1221–1223.

(10) (a) Dulic´, D.; van der Molen, S. J.; Kudernac, T.; Jonkman, H. T.; de Jong, J. J. D.; Bowden, T. N.; van Esch, J.; Feringa, B. L.; van Wees, B. J. *Phys. Rev. Lett.* **2003**, *91*, 207402. (b) He, J.; Chen, F.; Liddell, P. A.; Adre´asson, J.; Straight, S. D.; Gust, D.; Moore, T. A.; Moore, A. L.; Li, J.; Sankey, O. F.; Lindsay, S. M. *Nanotechnology* **2005**, *16*, 695–702. (c) Katsonis, N.; Kudernac, T.; Walko, M.; van der Molen, S. J.; van Wees,B. J.; Feringa, B. L. *Adv. Mater.* **2006**, *18*, 1397–1400. (d) Taniguchi, M.; Nojima, Y.; Yokota, K.; Terao, J.; Sato, K.; Kambe, N.; Kawai, T. *J. Am. Chem. Soc.* **2006**, *128*, 15062–15063. (e) Whalley, A. C.; Steigerwald, M. L.; Guo, X.; Nuckolls, C. *J. Am. Chem. Soc.* **2007**, *129*, 12590–12591.

(11) Kamat, P. V. *J. Phys. Chem. B* **2002**, *106*, 7729–7744.

(12) Xiao, X.; Xu, B.; Tao, N. J. *Nano Lett.* **2004**, *4*, 267–271.

(13) (a) Uchida, K.; Tsuchida, E.; Aoi, Y.; Nakamura, S.; Irie, M. *Chem. Lett.* **1999**, 63–64. (b) Irie, M.; Sakemura, K.; Okinaka, M.; Uchida, K. *J. Org. Chem.* **1995**, *60*, 8305–8309.

(14) Ikeda, M.; Tanifuji, N.; Yamaguchi, H.; Irie, M.; Matsuda, K. *Chem. Commun.* **2007**, 1355–1357.

(15) Preliminary study on silver nanoparticles of 2a was reported in the following: Sakano, T.; Yamaguchi, H.; Tanifuji, N.; Irie, M.; Matsuda, K. *Chem. Lett.* **2008**, *37*, 634–635.

(16) Matsuda, K.; Matsuo, M.; Mizoguti, S.; Higashiguchi, K.; Irie, M. *J. Phys. Chem. B* **2002**, *106*, 11218–11225.

(17) Morales, G. M.; Jiang, P.; Yuan, S.; Lee, Y.; Sanchez, A.; You, W.; Yu, L. *J. Am. Chem. Soc.* **2005**, *127*, 10456–10457.

(18) Brust, M.; Walker, M.; Bethell, D.; Schiffrin, D. J.; Whyman, R. *Chem. Commun.* **1994**, 801–802.

(19) See Supporting Information. For IR spectrum of **Au-4a**, see ref 14.

(20) See Supporting Information. For TEM image of **Au-4a**, see ref 14.

(21) Yamaguchi, H.; Ikeda, M.; Matsuda, K.; Irie, M. *Bull. Chem. Soc. Jpn.* **2006**, *79*, 1413–1419.

(22) Yamaguchi, H.; Matsuda, K.; Irie, M. *J. Phys. Chem. C* **2007**, *111*, 3853–3862.

(23) Manna, A.; Chen, P.-L.; Akiyama, H.; Wei, T.-X.; Tamada, K.; Knoll, W. *Chem. Mater.* **2003**, *15*, 20–28.

(24) Matsuda, K.; Irie, M. *Chem. Eur. J.* **2001**, *7*, 3466–3473.

(25) Yu, C. J.; Chong, Y.; Kayyem, J. F.; Gozin, M. *J. Org. Chem.* **1999**, *64*, 2070–2079.

Chapter 2

Percolation-type Photoswitching Behavior in Conductance of Diarylethene–Silver Nanoparticle Networks

Abstract

A silver nanoparticle network interlinked by photochromic diarylethene dithiophenols was fabricated and its photoreactive and conductive properties were investigated. The network showed reversible changes in absorption spectra and conductance by photoirradiation. The results indicate the percolationtype behavior.

This work has been presented in *Chem. Lett.* **2008**, *37*, 634-635, essentially in the same form.

Introduction

Research on ‘‘molecular electronics’’ is dramatically being advanced using traditional and new methods such as STM[1] and nanogapped electrodes.[2] Network structures composed of stimuli-responsive molecules and metal nanoparticles attract increasing attention.[3] Diarylethene derivatives can be regarded as a single molecular photoswitch because π-conjugation length of both isomers is interconverted by UV and visible light.[4] Feringa et al. reported the three orders of magnitude conductance change of single diarylethene molecule.[5] We have reported the conductance photoswitching of a network composed of diarylethene dithiophenols and gold nanoparticles.[6] Among many metal nanoparticles, silver nanoparticles have unique optical properties such as enhancement of local electromagnetic field, resulting in enhanced Raman scattering[7] and photoemission. [8]

Herein, we report on the reversible conductance photoswitching of a diarylethene–silver nanoparticle network induced by photochromism of diarylethenes. The percolation-type behavior will be discussed.

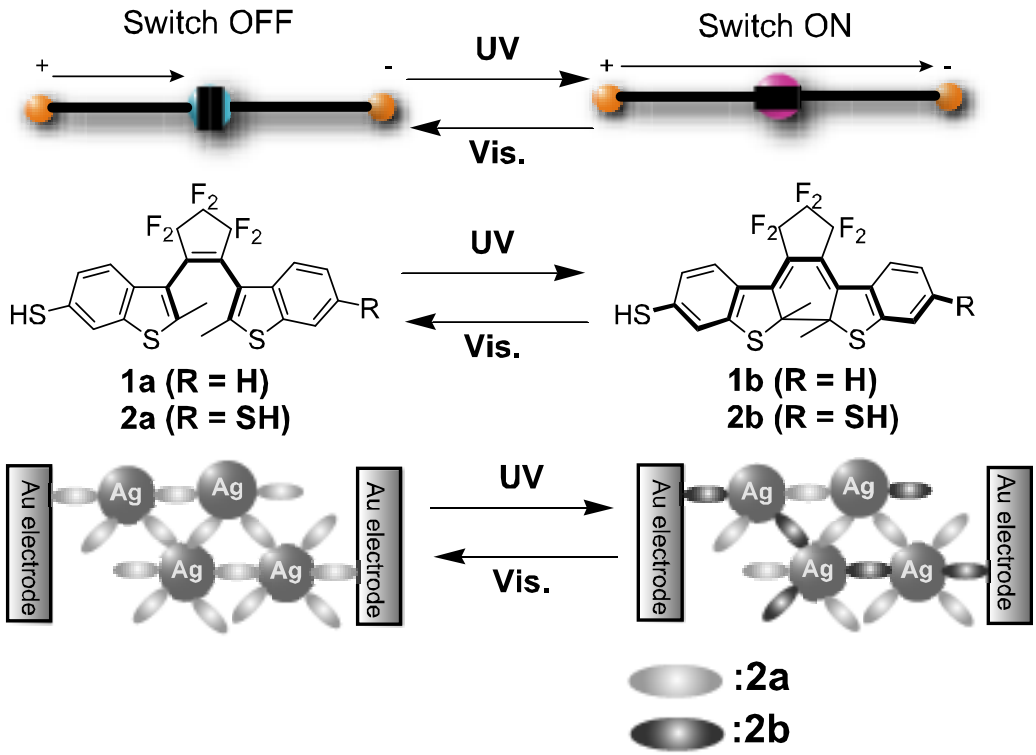

Figure 1. Molecular structure of compounds **1** and **2**. Schematic illustration of silver nanoparticle network **Ag–2**.

Results and discussion

UV-vis. spectroscopy

As photochromic linkers, benzothiophene diarylethene thiophenols **1** and **2** were synthesized (Figure 1).[9] This type of diarylethene has high cycloreversion quantum yield (Φ_{CO} = 0:35).[10] Photochromic absorption spectral changes were observed for ligands **1a** and **2a** in toluene solution (Figure 2).[11] The colorless solution turned red under irradiation with 313 nm light, indicating the formation of the closed-ring isomers **1b** and **2b**. The absorption maxima of the closed-ring isomers are located at 532 and 541 nm for **1b** and **2b**, respectively. These colored solutions went back to colorless under irradiation with 578 nm light.

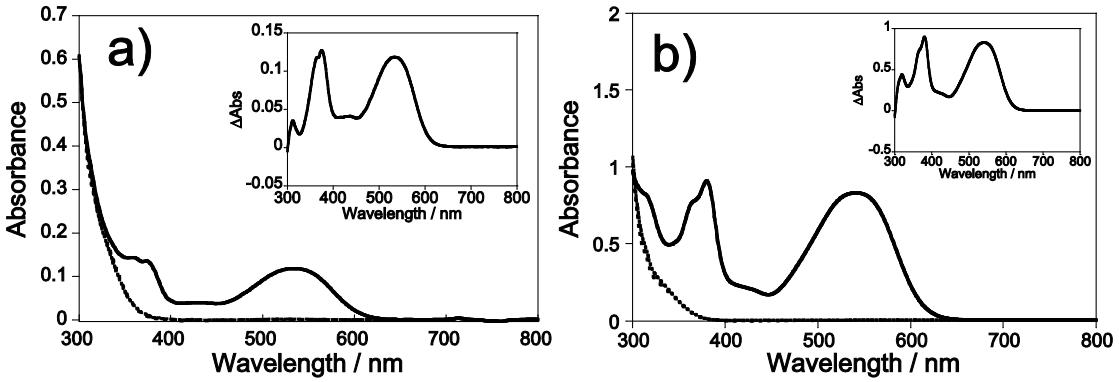

Figure 2. Absorption spectral changes of a) **1** and b) **2** in toluene solution: before photoirradiation (dotted line); after irradiation with 313 nm (solid line); after following irradiation with 578 nm (dashed line). Inset: difference absorption spectra between those measured before and after UV irradiation.

Ag nanoparticles capped with monothiol **1a** (**Ag–1a**) were prepared according to the procedure of Kim which is a modification of Brust's method.[12] The silver nanoparticles were soluble in organic solvents. The prepared **Ag–1a** was observed by a transmission electron microscope (TEM), and the average diameter was determined to be 9.1 ± 3.4 nm (Figure 3).[11] IR spectroscopy also supported that **1a** is attached to Ag nanoparticles because the spectrum of **Ag–1a** is similar to that of **1a**.[11] In order to study the photochromic properties of **Ag–1a**, absorption spectra were measured in toluene solution. As shown in Figure 4,[11] surface plasmon band appeared around 480 nm. When this solution was irradiated with 313 nm light, a new band originating from the closed-ring isomer appeared. When this solution was irradiated with 578 nm light, the new band disappeared. Absorption maximum of the closed-ring isomer is located at 582

nm, which is shifted to longer wavelength by 50 nm in comparison with the maximum of **1b**.

Preparation of the interlinked **Ag–2a** network was performed according to a previously reported method.[6] The Ag nanoparticles protected by tetraoctylammonium bromide (TOAB) were firstly prepared, and then the dithiol was mixed to make the network. From the TEM images, the diameter of TOAB-protected silver nanoparticles was determined to be 8.5 ± 2.0 nm (Figure 4).[11] The absorption spectra of **Ag–2a** were measured in KBr matrix (Figure 5). The network has broadened absorption from the visible to near-infrared region instead of the clear plasmon absorption at 480 nm that is observed for **Ag–1a**.

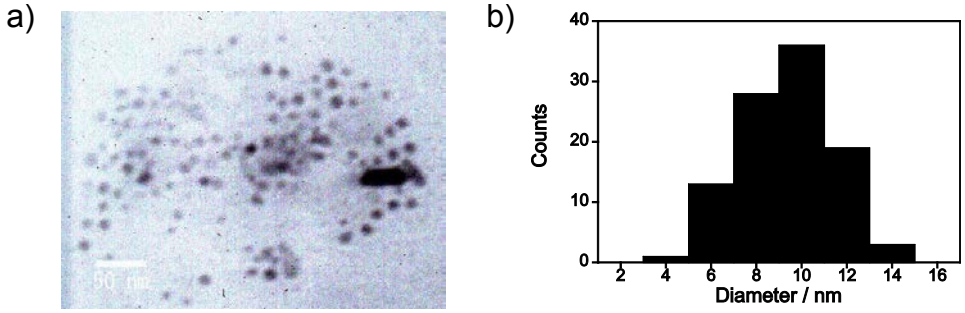

Figure 3. a) TEM image of **Ag-1a** nanoparticles. b) Histogram of the size of the **Ag-1a** nanopartilces.

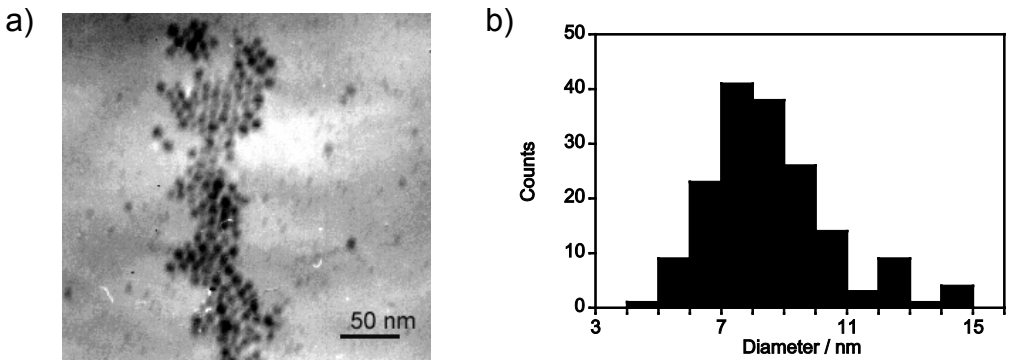

Figure 4. a) TEM image of TOAB-protected **Ag** nanoparticles for making **Ag-2a** nanoparticle network. b) Histogram of the size of the TOAB-protected **Ag** nanoparticles.

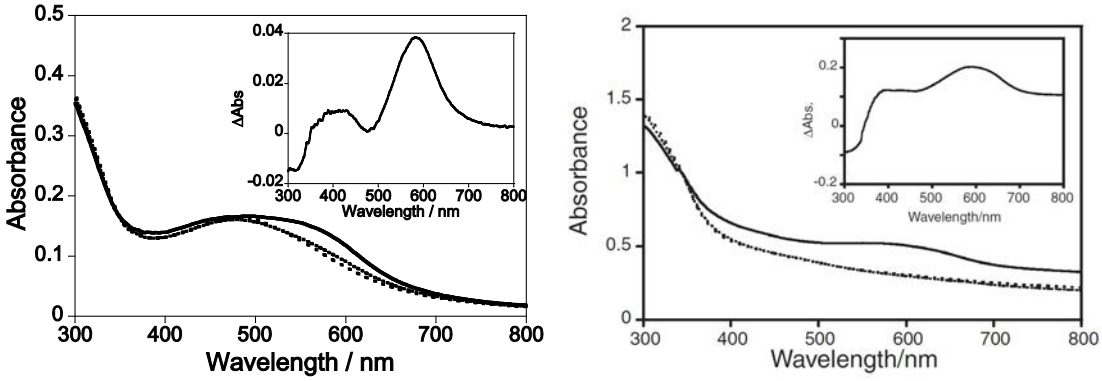

Figure 5. (a) Absorption spectral change of **Ag-1** in toluene solution. Before photoirradiation (dotted line); after irradiation with 313 nm (solid line); after following irradiation with 578 nm (dashed line). Inset: difference absorption spectrum of **Ag-1** between those measured before and after UV irradiation. (b) Absorption spectra of **Ag–2**: dashed line, before irradiation; solid line, after UV irradiation; dotted line, after visible light irradiation. Inset: difference absorption spectra between those measured before and after UV irradiation.

When the network is irradiated with 313 nm light, not only an absorption band originating from the closed-ring isomer (absorption maximum: 590 nm) but also a broad band spread in the near-infrared region (>650 nm) were observed. Changes of both bands were confirmed to be reversible by irradiation with UV and following with visible light. This reversible absorption change in the near-infrared region may suggest that the intensity of plasmon coupling is switched by photochromic reaction of interlinked diarylethenes.[13] This phenomenon was not discerned in the case of Au nanoparticle networks.

Conductance measurement of diarylethene-silver nanoparticle networks

Ag–2a was prepared on an interdigitated gold electrode (NTT-AT, 5 μm gap) in order to investigate the conductance change by photoirradiation. The fabricated network was stable against applied voltage from 0 to 4 V. Upon irradiation with UV light, an increase of conductance was observed. After UV irradiation for 60 min, the conductance became around 18 times larger than the initial value as shown in Figure 6. The increased conductance returned to the initial value after irradiation with visible (> 560 nm) light for 450 min. This switching behavior can be explained by the photochromic reaction between ‘‘OFFstate’’ (open-ring isomer) and ‘‘ON-state’’ (closed-ring isomer).

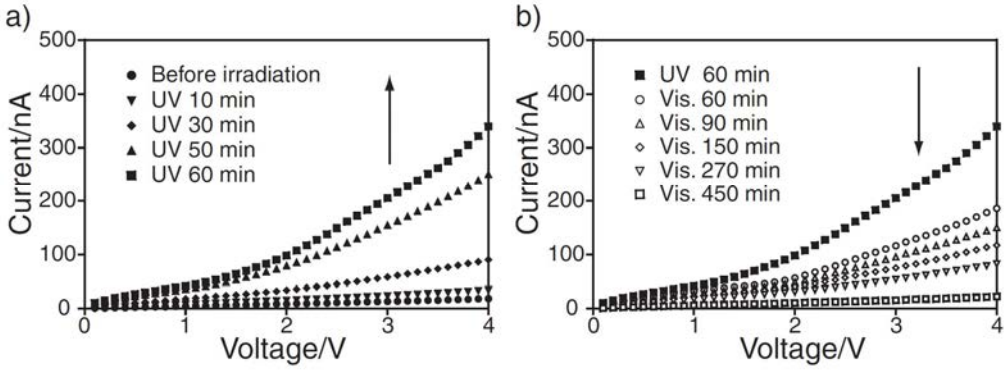

Figure 6. Conductance photoswitching behavior of **Ag–2a** network on the interdigitated electrode: a) upon irradiation with UV light; b) upon irradiation with visible light.

Percolation behavior of diarylethene-silver nanoparticle networks

In order to investigate the mechanism of conductance photoswitching, the time profiles of the conductance and the absorbance were measured at different stages of the photochromic reaction. Figure 7a shows the time profile of the increase of the absorbance at 590 nm of **Ag–2** network. The absorbance at 590 nm has a linear relationship with the population of the closed-ring isomer. The plot shows that the reaction rate is larger at the beginning and gets smaller as the reaction proceeds. This is a normal photochemical reaction. On the other hand, the time profile of the conductance showed a different behavior (Figure 7b). The reaction rate is smaller at the beginning and gets larger as the reaction proceeds. The difference of the two time profiles suggests that the increase of the conductance does not directly reflect the content of the closed-ring isomer but can be explained by the percolation model.[14] The network is not completely connected by the closed-ring isomer at the initial stage of the photochromic reaction, but as the reaction proceeds the closed-ring isomers make the conducting path between the interdigitated electrodes.

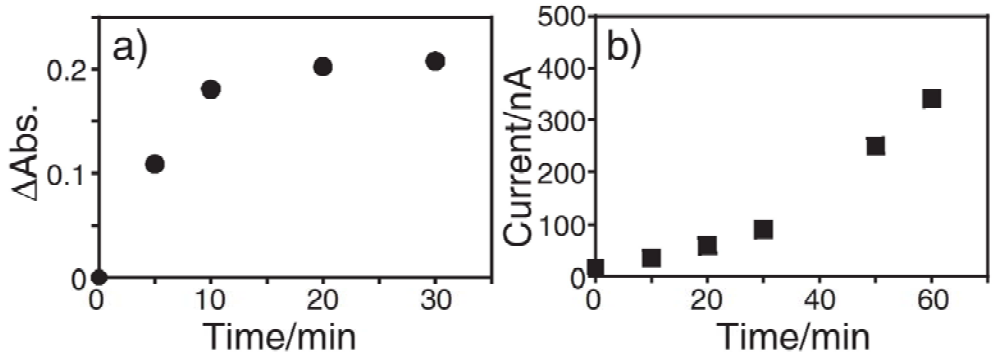

Figure 7. Time profiles of the photoinduced change of **Ag–2** network. a) Plot of difference absorbance at 590 nm. b) Plot of current value measured at applied voltage of 4V.

Conclusions

In conclusion, we have demonstrated 18-fold reversible change in conductance of a diarylethene–Ag nanoparticle network by photoirradiation. The time profiles of absorbance and conductance indicate the percolation-type behavior.

Experimental Method

1. Materials

Preparation of Ag-1a nanoparticles:

To a solution of $AgNO_3$ in ultrapure water (18.2 MΩ•cm) (32.6 mM, 1.02 mL, 0.033 mmol) was added tetraoctylammonium bromide (103 mg, 0.188 mmol) in toluene (10 mL). Then **1a** (20 mg, 0.040 mmol) was added to the mixture. After vigorous stirring, $NaBH_4$ (16 mg, 0.423 mmol) in ultrapure water (2.0 mL) was added to the reaction mixture and the solution was stirred for 3h. The organic layer was separated and concentrated. The residue was washed by methanol to give **Ag-1a** nanoparticles. The sample was kept in toluene solution.

Preparation of TOAB-protected silver nanoparticles:

To a solution of $AgNO_3$ in ultrapure water (18.2 MΩ•cm) (32.6 mM, 5.0 mL, 0.163 mmol) was added tetraoctylammonium bromide (92 mg, 0.168 mmol) in toluene (10 mL) and ultrapure water (3.0 mL). The reaction mixture was stirred vigorously and $NaBH_4$ (33 mg, 0.873 mmol) in ultrapure water (3.0 mL) was added to the reaction mixture. After stirring for 3 h, the organic layer was separated. The sample was kept

in toluene solution.

Preparation of Ag-2a nanoparticle network

Trimethylsilylethyl-protected **2a** (10mg, 0.014 mmol) was deprotected by tetrabutylammonium fluoride and was dissolved in toluene (0.15 mL) and TOAB capped silver nanoparticles toluene solution (0.50 mL) was added to the solution. For the conductance measurement, one drop of the mixture was dripped on a interdigitated 5 μm-gapped gold electrode, and the electrode was washed with methanol and dried in vacuum. For the spectroscopic measurement, the mixture was concentrated and washed with methanol. The residue was mixed with KBr powder and pressed to form a transparent pellet of **Ag-2a** network.

2. Conductance measurement

Conductance measurement was performed by a remote sourcemeter (Keithley Model 6430) equipped with preamplifier and interdigitated gold electrode (NTT-AT, 5 μm-gap). The electrode and preamplifier were covered with stainless wire net. The wavelength of UV light was used from 290 nm to 380 nm and the one of visible light was over 560 nm.

Notes and References

(1) L. Venkataraman, J. E. Klare, C. Nuckolls, M. S. Hybertsen, M. L. Steigerwald, *Nature* **2006**, *442*, 904.

(2) M. Mayor, H. B. Weber, J. Reichert, M. Elbing, C. von Ha¨nisch, D. Beckmann, M. Fischer, *Angew. Chem., Int. Ed.* **2003**, *42*, 5834.

(3) T. Ogawa, K. Kobayashi, G. Masuda, T. Takase, S. Maeda, *Thin Solid Films* **2001**, *393*, 374.

(4) M. Irie, *Chem. Rev.* **2000**, *100*, 1685.

(5) D. Dulic´, S. J. van der Molen, T. Kudernac, H. T. Jonkman, J. J. D. de Jong, T. N. Bowden, J. van Esch, B. L. Feringa, B. J. van Wees, *Phys. Rev. Lett.* **2003**, *91*, 207402.

(6) M. Ikeda, N. Tanifuji, H. Yamaguchi, M. Irie, K. Matsuda, *Chem. Commun.* **2007**, 1355.

(7) H. K. Park, J. K. Yoon, K. Kim, *Langmuir* **2006**, *22*, 1626.
S. Pan, L. J. Rothberg, *J. Am. Chem. Soc.* **2005**, *127*, 6087.

(8) The synthesis of **1** and **2** is reported in *J. Phys. Chem. C* **2008**, *112*, 17005. **1a**: ^{1}H NMR (400 MHz, TMS) δ 2.17 (s, 1.9H), 2.20 (s, 1.9H), 2.46 (s, 1.1H), 2.47 (s, 1.1H), 3.46 (s, 0.4H), 3.55 (s, 0.6H), 7.15–7.71 (m, 7H); HRMS (*m*/*z*) $[M]^+$ Calcd for $C_{23}H_{14}F_6S_3$: 500.0162, found: 500.0156. **2a**: ^{1}H NMR (400 MHz, TMS) δ 2.16 (s, 3.8H), 2.44 (s, 2.2H), 3.49 (s, 0.8H), 3.56 (s, 1.2H), 7.08–7.50 (m, 6H); HRMS (*m*/*z*) $[M]^+$ Calcd for $C_{23}H_{14}F_6S_4$: 531.9882, found: 531.9872.

(10) K. Uchida, E. Tsuchida, Y. Aoi, S. Nakamura, M. Irie, *Chem. Lett.* **1999**, 63.

(11) Supporting Information is available electronically on the CSJ-Journal Web site, http://www.csj.jp/journals/chem-lett/.

(12) S. Y. Kang, K. Kim, *Langmuir* **1998**, *14*, 226.

(13) L. Suber, D. Fiorani, G. Scavia, P. Imperatori, W. R. Plunkett, *Chem. Mater.* **2007**, *19*, 1509.

(14) M. Eikerling, A. A. Kornyshev, U. Stimming, *J. Phys. Chem. B* **1997**, *101*, 10807.

Chapter 3

Comparison of molecular conductance between planar and twisted 4-phenylpyridines by means of two-dimensional phase separation of tetraphenylporphyrin templates at a liquid–HOPG interface

Abstract

Tetraphenylporphyrin (TPP) rhodium chlorides coordinated by planar and twisted 4-phenylpyridine derivatives were synthesized. An STM image was taken by a 2-D phase separation technique and the conductance was evaluated. Difference in apparent height between these phenylpyridines reflects the conductance ratio of ligands.

This work has been presented in *Chem. Commun.* **2011**, *47*, 8427-8429, essentially in the same form.

Introduction

The investigation of single molecular conductance is a key issue in the molecular electronics field and is developing rapidly using several measurement techniques.[1] Although most experiments on the conductance of a single molecule exhibit considerable variations, the reliability of the measurements has recently been significantly increased owing to the statistical treatment by the methods of mechanically controllable break junction[2] and scanning tunneling microscopy break junction.[3,4]

Among several methods for the measurement of the molecular conductance, apparent height measurement by STM has the merit of applicability to many samples.[5,6] The method often utilizes the plating of target molecules into the self-assembled monolayers (SAMs) of alkanethiols on an Au substrate in order to prevent the intermolecular interaction among target molecules. However, this usual method precludes the statistical treatment because only few spots of target molecules are observable from one STM image. Use of a molecular template is one candidate to avoid the intermolecular interaction and STM observation of the SAM of samples on the templates makes the statistical analysis possible. Herein, we report on the comparison of molecular conductance between planar and twisted 4-phenylpyridine derivatives by using porphyrin templates, and show that a two-dimensional (2-D) phase separation technique is effective to discriminate these phenylpyridines on the substrate.

Results and Discussion

Pyridine-coordinated tetraphenylporphyrin (TPP) Rh(III) chloride having long alkyl chains forms 2-D lamellar structures at a liquid–HOPG interface, where a strongly bound axial ligand of pyridine is placed perpendicular on the TPP.[7] Therefore, TPP rhodium chloride can be used as a molecular template for the compounds carrying pyridyl groups. 4-Phenylpyridine derivatives **1** and **2** having the same molecular lengths and the different torsion angles were selected to investigate the differences in the apparent height in STM images because they are expected to have different molecular conductances due to the different torsion angles (Figure 1).[4]

Syntheses of 4-phenylpyridine-coordinated TPP rhodium chlorides (**C_0-Rh-1**, **C_0-Rh-2**, **C_{22}-Rh-1**, **C_{22}-Rh-2**, and **C_{30}-Rh-1**) were carried out according to the general organic synthesis procedure described in experimental section. Subscript numbers 0, 22, and 30 show the length of alkyl side chains. Free base TPPs **C_{16}-2H**, **C_{22}-2H**, and

C_{30}-2H were also synthesized. X-Ray crystallographic analysis of **C_0-Rh-1** and **C_0-Rh-2** revealed that the dihedral angles between the phenyl ring and the pyridyl ring of **1** and **2** are 27° and 68°, respectively. The ORTEP drawings are shown in Figure 2.

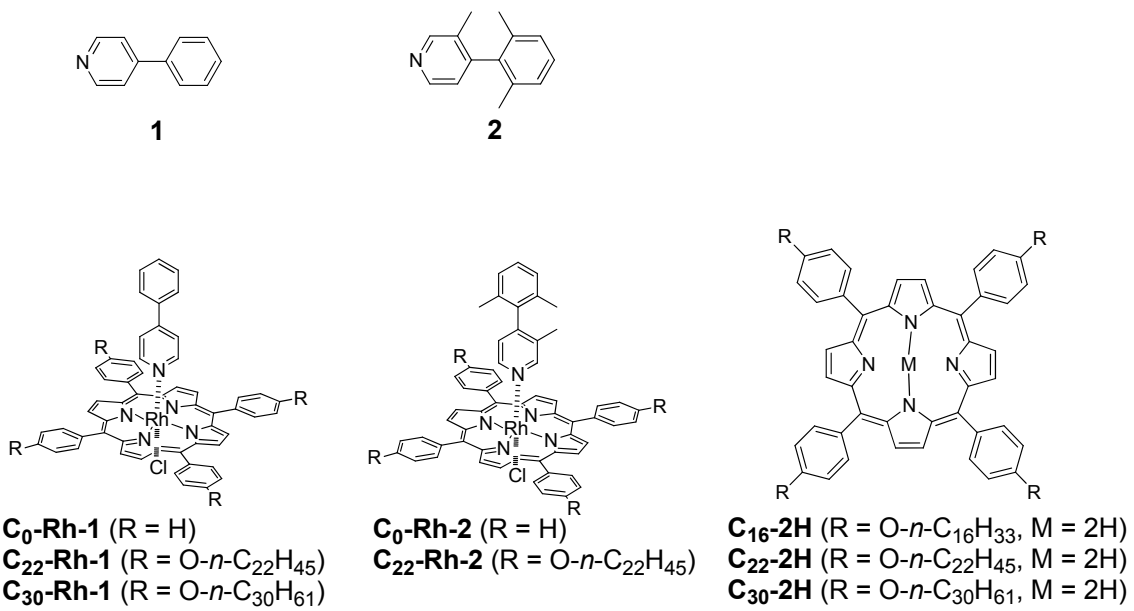

Figure 1. Molecular structures of synthesized 4-phenylpyridines, TPPs, and TPP rhodium chlorides.

STM images for a solution of **C_{22}-Rh-1** and for a 1:1 mixed solution of **C_{22}-Rh-1** and **C_{22}-Rh-2** were obtained at the 1-octanoic acid–HOPG interface in the constant current mode.[8] As shown in Figure 3a and b, both samples formed SAMs of characteristic lamellar structures, where TPPs are aligned side by side in the bright stripes. The stripes are separated by the alkyl chains from the neighboring TPP arrays.[9] In the dark areas the alkyl chains are interdigitated, although detailed structure of these chains was not observed in these images. The lattice parameters of the unit cell $a \times b$ and α were 3.9 ± 0.2 nm × 1.8 ± 0.2 nm and 71° for **C_{22}-Rh-1** and 4.2 ± 0.2 nm × 2.3 ± 0.2 nm and 82° for a mixture of **C_{22}-Rh-1** and **C_{22}-Rh-2**. These values are similar to that of characteristic lamellar structures of **C_{22}-2H** at the phenyloctane–HOPG interface (4.1 ± 0.2 nm × 1.9 ± 0.2 nm and 84°; also reported in ref. 10 as 4.2 nm × 2.1 nm and 84°).

Contrast of the TPP core shows the apparent height of the core above the alkyl side chains. Section analysis of Figure 3a is shown in Figure 3c. Statistical analyses of

apparent height for these STM images based on the section analysis are shown in Figure 3d and e. Both statistical distributions of apparent heights were fitted by a single Gaussian function. By mixing **C_{22}-Rh-2** into **C_{22}-Rh-1**, an apparent height distribution got lowered and broadened from 3.9 ± 0.5 Å to 3.6 ± 0.9 Å. In terms of apparent height, absolute values of the height are generally varied with measurement conditions even in the same setup. Therefore, the decrease of apparent height by mixing **C_{22}-Rh-2** does not give the relationship of apparent height between **C_{22}-Rh-1** and **C_{22}-Rh-2**. However, the result of broadening of the distribution suggests that **C_{22}-Rh-2** shows the different apparent height from **C_{22}-Rh-1**. Since topographic heights are the same for **C_{22}-Rh-1** and **C_{22}-Rh-2** at the 1-octanoic acid–HOPG interface, this difference in apparent height shows the difference in a tunneling decay constant of axial ligands of **1** and **2**.

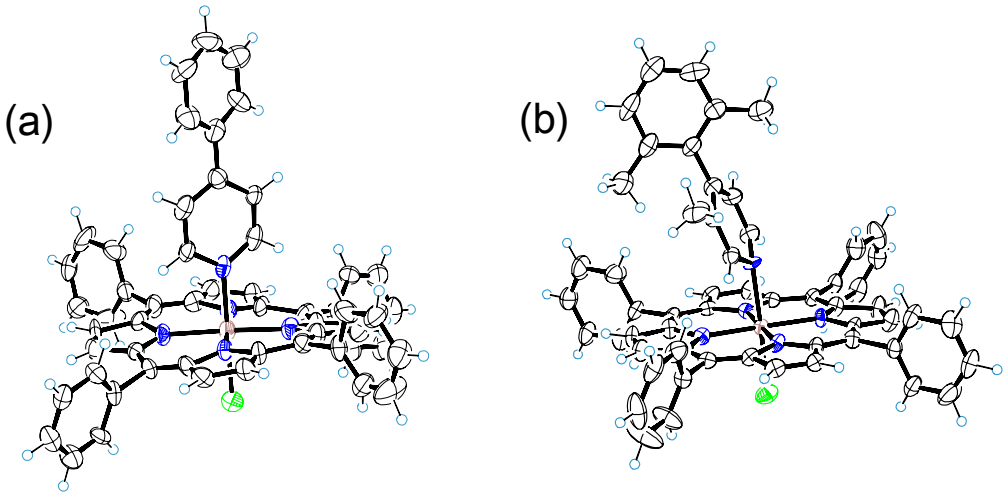

Table 1. Crystallographic parameters for **C_0-Rh-1**

formula	$C_{61}H_{49}ClN_5O_2Rh$
formula weight	1022.4326
crystal system	Monoclinic
space group	*Cc*
a / Å	17.5590(8)
b/ Å	15.5831 (7)
c / Å	18.4654(8)
β / º	105.247(1)
volume / Å^3	4874.7(4)
Z	4
R_1	0.0373
wR_2	0.0847

Table 2. Crystallographic parameters for **C_0-Rh-2**

formula	$C_{59}H_{47}N_5OClRh$
formula weight	980.3959
crystal system	Monoclinic
space group	*Cc*
a / Å	17.7891(12)
b/ Å	13.8346(11)
c / Å	20.6811(19)
β / º	111.2830(10)
volume / Å^3	4742.6(6)
Z	4
R_1	0.0477
wR_2	0.1343

Figure 2. ORTEP drawings of the X-ray crystallographic structures of (a) **C_0-Rh-1** and (b) **C_0-Rh-2**. Solvents are omitted from the figures for clarity.

To clear up this difference, apparent height distributions for these two ligands need to be distinctly separated. We focused our attention on the coadsorption phenomena at a liquid–solid interface[11] and the coadsorption behavior of two free base TPPs, **C_{16}-2H** and **C_{22}-2H**, was examined. Figure 4a shows an STM image for a mixed solution of **C_{16}-2H** and **C_{22}-2H**. Two domains were observed and each domain has different lattice parameters. Lattice parameters of the right domain were 3.4 ± 0.2 nm × 1.8 ± 0.2 nm and 89°, whereas those of the left one were 4.0 ± 0.2 nm × 1.6 ± 0.2 nm

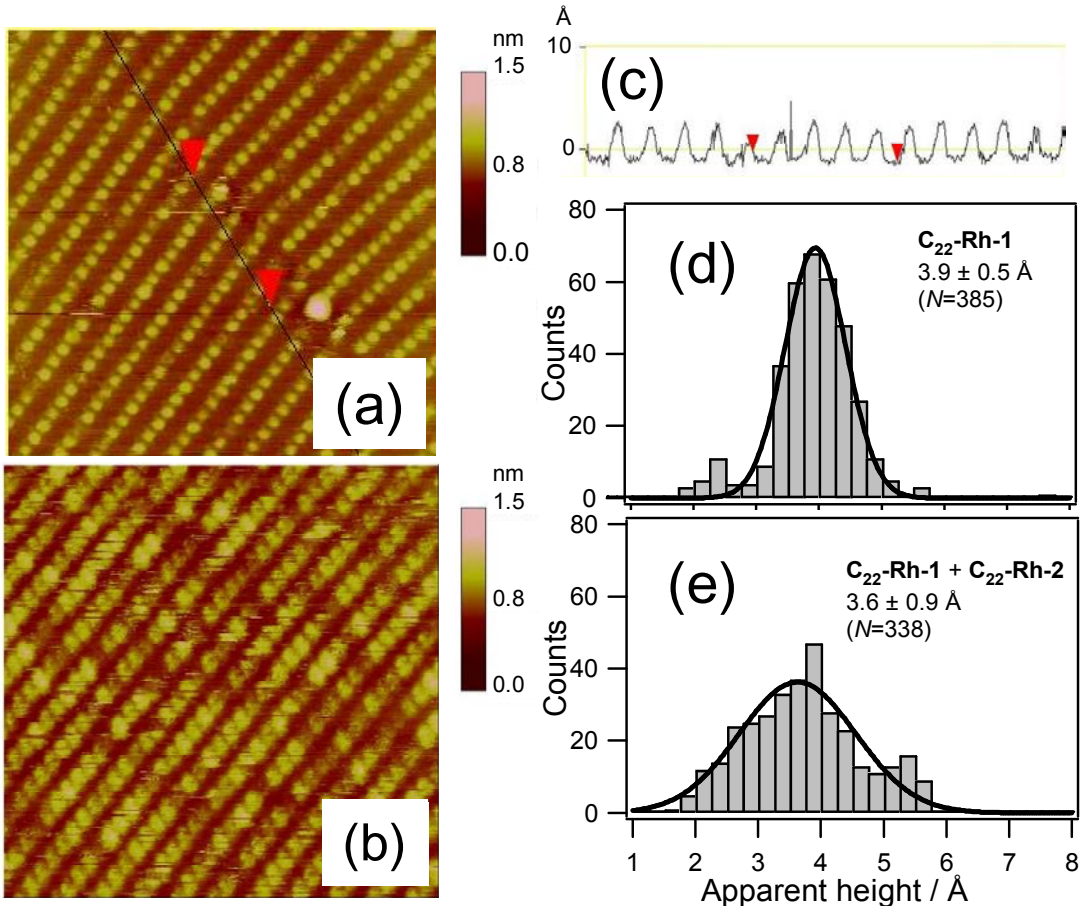

Figure 3. STM images at the 1-octanoic acid–HOPG interface in the constant current mode: (a) **C_{22}-Rh-1** (3.0×10^{-6} M) (50×50 nm^2, I_{set} = 30 pA, V_{bias} = 1.0 V); (b) a 1 : 1 mixed solution of **C_{22}-Rh-1** (1.5×10^{-6} M) and **C_{22}-Rh-2** (1.5×10^{-6} M) (60×60 nm^2, I_{set}=30 pA, V_{bias} = -1.0 V). (c) Section analysis for the image (a). Histograms of apparent height of TPP cores: (d) for the image (a); (e) for the image (b).

By means of the 2-D phase separation method, the apparent height of **1** and **2** was measured. Figure 5a shows an STM image of a mixed solution of **C_{30}-Rh-1** and **C_{22}-Rh-2**. Two domains having different lattice parameters of the unit cell were observed in one STM image. A domain on the bottom-left corner had a lattice spacing corresponding to that of **C_{30}-2H** and another one on the upper-right corner had a similar spacing of **C_{22}-2H** lattice. These domains correspond to the domains of **C_{30}-Rh-1** and **C_{22}-Rh-2**. Histograms of apparent height were separately created for each domain as shown in Figure 5b and c. Apparent heights were obtained as 4.3 ± 0.7 Å for **C_{30}-Rh-1** and 2.9 ± 0.6 Å for **C_{22}-Rh-2**. Since geometrical molecular heights of **C_{30}-Rh-1** and **C_{22}-Rh-2** are the same, the difference in apparent height should originate from the conductance ratio of two ligands **1** and **2**. Summation of these histograms gave a broad distribution (Figure 5d), which is in good agreement with the distribution of an apparent height of 1:1 mixture of **C_{22}-Rh-1** and **C_{22}-Rh-2** that has already been shown in Figure 3e.

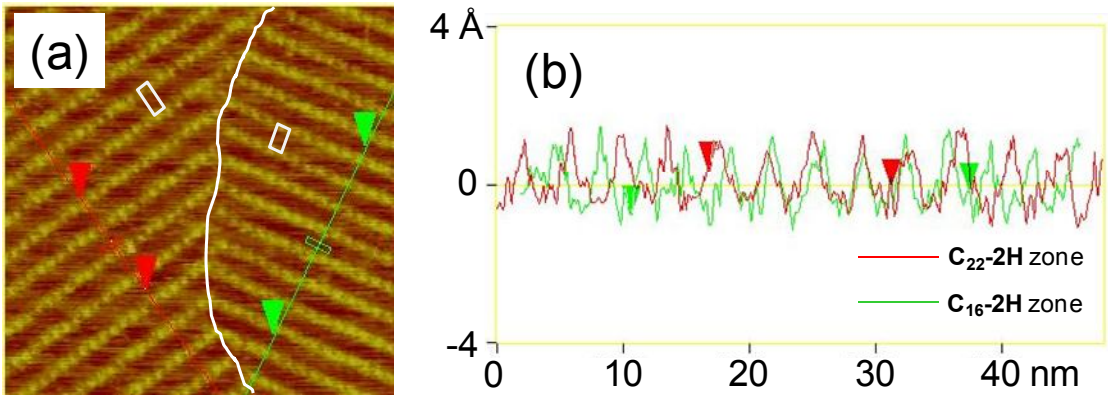

Figure 4. An STM image at the 1-phenyloctane–HOPG interface in the constant current mode: (a) a 3 : 1 mixed solution of **C_{16}-2H** (1.2×10^{-6} M) and **C_{22}-2H** (4.0×10^{-7} M) (50× 50 nm^2, I_{set}=30 pA, V_{bias}=-1.0 V). (b) Section analyses of **C_{22}-2H** (red line) and **C_{16}-2H** (green line) domains. White parallelograms in the STM images show the unit cells.

and 88°. These two parameters are similar to those of **C_{16}-2H** and **C_{22}-2H**. This result shows that the 2-D phase separation of **C_{16}-2H** and **C_{22}-2H** occurred at the solid–liquid interface. Section analysis of each domain shows that there is no significant difference in the apparent height, suggesting that the length of alkyl side chain does not influence the apparent height (Figure 4b).

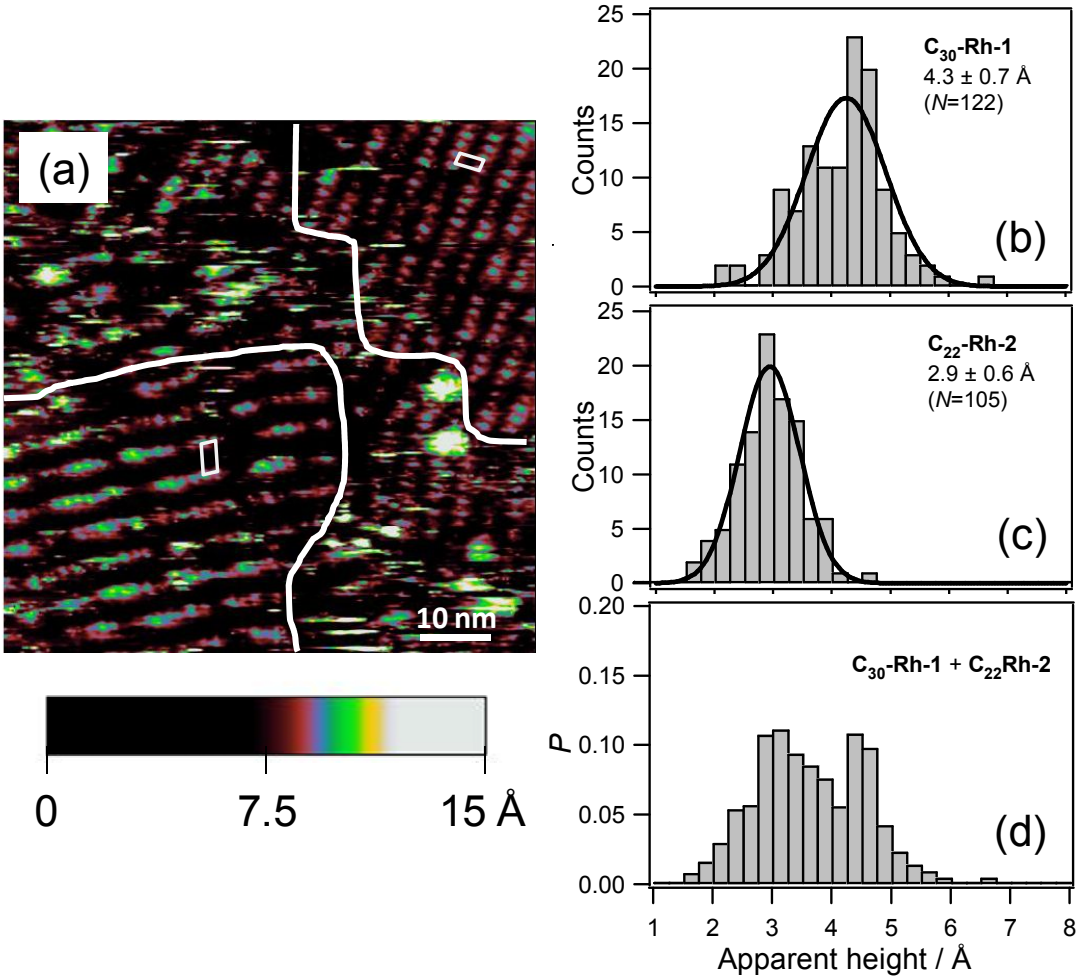

Figure 5. (a) An STM image of a 10 : 1 mixed solution of **C_{22}-Rh-2** (1.5×10^{-6} M) and **C_{30}-Rh-1** (1.5×10^{-7} M) (75×75 nm^2, I_{set}=30 pA, V_{bias} = -1.0 V) at the 1-octanoic acid–HOPG interface in the constant current mode. Histograms of apparent height in the domain of (b) **C_{30}-Rh-1**, (c) **C_{22}-Rh-2**, and (d) both **C_{30}-Rh-1** and **C_{22}-Rh-2**. The contribution in counts from each domain was normalized to 1 : 1 in histogram (d).

According to the two-layer tunnel junction model proposed by Weiss et al.,[5] the total conductance (G_{total}) between an STM tip and a substrate is described by product of the gap conductance ($G_{gap} = A \exp(-\alpha d)$) and molecular conductance ($G_{mol} = B \exp(-\beta x)$), where A and B are contact conductances, α and β are decay constants of the gap and the molecule, d is the gap distance and x is the molecular length. G_{total} is constant everywhere, therefore, the conductance ratio (G_{mol1}/G_{mol2}) is given by the following eqn (1):

$$\frac{G_{\mathrm{mol1}}}{G_{\mathrm{mol2}}} = \frac{G_{\mathrm{gap2}}}{G_{\mathrm{gap1}}} = \frac{A_2}{A_1}\exp\{\alpha(d_1 - d_2)\} \qquad (1)$$

This equation means that the ratio of A_2/A_1, decay constant of the gap (α), and difference in gap distance (d_1–d_2) give the conductance ratio. The measurement condition is identical because STM measurement was carried out for structurally similar phenylpyridines **C_{30}-Rh-1** and **C_{22}-Rh-2** and both molecules were observed in the same STM image. Therefore, contact-dependent terms A_1 and A_2 are assumed to be equal. Additionally, because x_1 and x_2 are the same, the term (d_1–d_2) is equal to the difference in apparent height Δh_{STM} (Figure 6). Then, eqn (1) is transformed to the following simple form:

$$\frac{G_{\mathrm{mol1}}}{G_{\mathrm{mol2}}} = \exp\{\alpha \Delta h_{\mathrm{STM}}\} \qquad (2)$$

This eqn (2) means that decay constant α of the gap and experimentally obtained Δh_{STM} give the conductance ratio between **C_{30}-Rh-1** and **C_{22}-Rh-2**. Since the STM measurement was conducted at the 1-octanoic acid–HOPG interface, α value of vacuum cannot be applied. We adopted the decay constant of a methylene unit (β = 1.2 $\mathrm{Å}^{-1}$) reported by the measurement of a series of alkanethiols as a substitute for 1-octanoic acid.[5] By introducing the measurement result Δh_{STM} = 1.4 Å, the conductance ratio between **C_{30}-Rh-1** and **C_{22}-Rh-2** is finally obtained to be $G_{\mathrm{mol1}}/G_{\mathrm{mol2}}$ = 5.4. Since these phenylpyridines **1** and **2** are supported by cognate templates, this conductance ratio originated from the twisting effect of the ligands. This result was compared to the $cos^2\phi$ law proposed by Venkataraman et al., in which molecular conductance of 4,4′-diaminobiphenyl is proportional to the $\cos^2\phi$, where is a dihedral angle.[4] Dihedral angles of **1** (27°) and **2** (68°) obtained from X-ray crystallographic analysis give conductance ratio $\cos^2\phi_1/\cos^2\phi_2$ = 5.7, which is in excellent agreement with experimentally obtained $G_{\mathrm{mol1}}/G_{\mathrm{mol2}}$ = 5.4. This agreement warrants that our method is applicable to the comparison of molecular conductance.

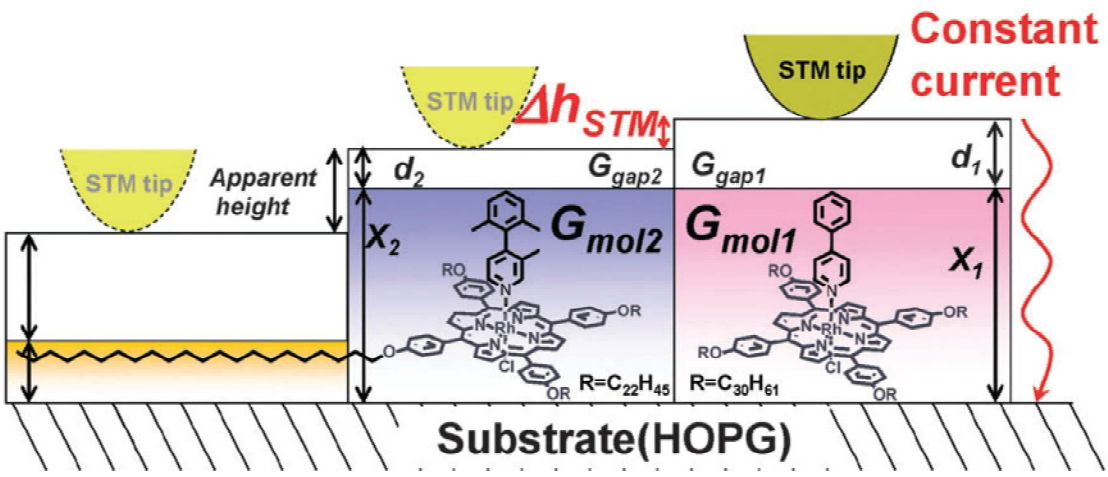

Figure 6. Schematic drawing of the two-layer tunnel junction model for the STM measurement of a mixed solution of **C_{30}-Rh-1** and **C_{22}-Rh-2**.

Conclusion

In conclusion, we have succeeded in developing the 2-D phase separation technique of TPP templates having different lengths of side chain at a solution–HOPG interface. This technique was applied to the determination of the ratio of molecular conductance between planar and twisted phenylpyridines by comparing apparent height in the STM image. This technique will be the useful method for the determination of molecular conductance.

Experimental section

1. Syntheses of the materials.

General. ^{1}H NMR spectra were recorded on a JEOL JMN-A500 instrument. Mass spectra were obtained by Bruker autoflex III MALDI-TOF mass spectrometer and Thermo Scientific Exactive mass spectrometer. All reactions were monitored by thin-layer chromatography carried out on 0.2 mm Merck silica gel plates (60F-254). Column chromatography was performed on silica gel (Nakarai, 70-230 mesh).

Scheme 1. General procedure for the syntheses of phenylpyridine-coordinated TPP rhodium chlorides.

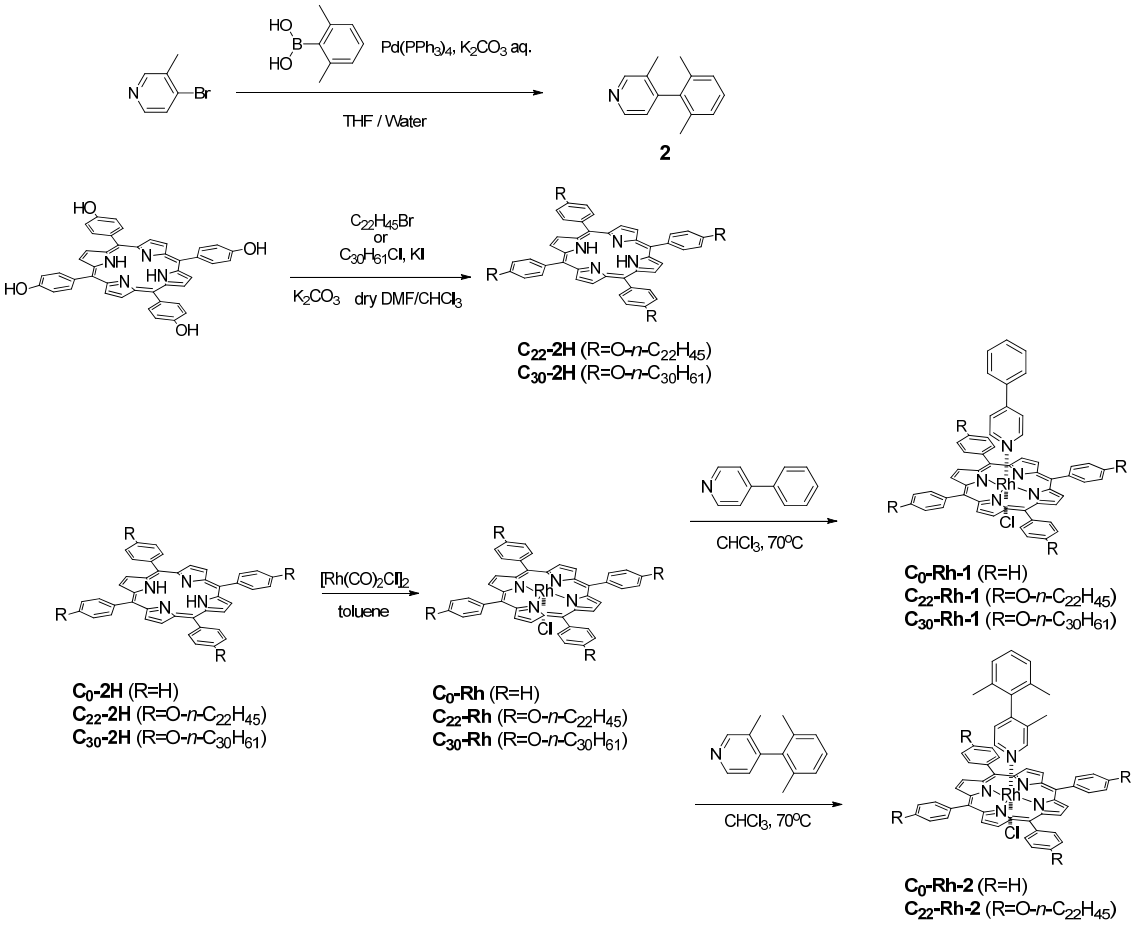

4-(2,6-Dimethylphenyl)-3-methylpyridine (2).

Tetrakis(triphenylphosphine)Palladium(0) (58 mg, 50 μmol), 2,6-dimethylphenylboronic acid (150 mg, 1.00 mmol), 4-bromo-3-methylpyridine[12] (172 mg, 1.00 mmol), and 20 wt% K_2CO_3 aqueous solution (4 mL) were mixed in THF (10 mL). The mixture was refluxed overnight. After cooled to room temperature, the mixture was extracted by diethyl ether. The organic layer was washed with brine, dried with Na_2SO_4, and concentrated *in vacuo* after filtration. Purification by column chromatography (silica, chloroform) and GPC (chloroform) gave 4-(2,6-dimethylphenyl)-3-methylpyridine as a colorless oil (103 mg, 523 μmol, 52%). ESI HRMS (*m*/*z*) $[M+H]^+$ calcd for $C_{14}H_{16}N$: 198.1277; found: 198.1277. ^1H NMR ($CDCl_3$, 500 MHz, TMS) δ 1.94 (s, 6H), 1.98 (s, 3H), 6.99 (d, J = 5 Hz, 1H), 7.12-7.13 (m, 2H), 7.19-7.21 (m, 1H), 8.50 (d, J = 5 Hz, 1H), 8.55 (s, 1H).

21,23-Dihidro-5,10,15,20-tetrakis(4-hexadecyloxyphenyl)porphyrin (C_{16}-2H).[13]
MALDI TOF-HRMS (*m*/*z*) $[M+H]^+$ calcd for $C_{108}H_{158}N_4O_4$: 1576.2356; found: 1576.2367. ^{1}H NMR ($CDCl_3$, 500 MHz, TMS) δ 1.94 (s, 6H), 1.98 (s, 3H), 6.99 (d, *J* = 5 Hz, 1H), 7.12−7.13 (m, 2H), 7.19−7.21 (m, 1H), 8.50 (d, *J* = 5 Hz, 1H), 8.55 (s, 1H).

21,23-Dihidro-5,10,15,20-tetrakis(4-docosyloxyphenyl)porphyrin (C_{22}-2H).[14]
MALDI TOF-HRMS (*m*/*z*) $[M+H]^+$ calcd for $C_{132}H_{207}N_4O_4$: 1912.6112; found: 1912.6080. ^{1}H NMR (CD_2Cl_2, 500 MHz, TMS) δ −2.81 (s, 2H), 0.87 (s, 12H), 1.25−1.64 (m, 152H), 1.98 (quint, *J* = 8 Hz, 8H), 4.26 (t, *J* =7 Hz, 8H), 7.29 (d, *J* = 9 Hz, 8H), 8.11 (d, *J* = 9 Hz, 8H), 8.89 (s, 8H).

21,23-Dihidro-5,10,15,20-tetrakis(4-triacontyloxyphenyl)porphyrin (C_{30}-2H).[15]
MALDI TOF-HRMS (*m*/*z*) $[M]^+$ calcd for $C_{164}H_{270}N_4O_4$: 2360.1042; found: 2360.1066. ^{1}H NMR ($CDCl_3$, 500 MHz, TMS) δ −2.75 (s, 2H), 0.87 (t, *J* = 7 Hz, 12H), 1.20-1.41 (m, 208H), 1.48 (quint, *J* = 7 Hz, 8H), 1.63 (quint, *J* = 7 Hz, 8H), 1.98 (quint, *J* = 7 Hz, 8H), 4.35 (t, *J* = 7 Hz, 8H), 7.26 (d, *J* = 9 Hz, 8H), 8.10 (d, *J* = 9 Hz, 8H), 8.86 (s, 8H).

1-Coordinated 5,10,15,20-tetrakisphenylporphyrin rhodium chloride (C_0-Rh-1).
Tetracarbonyl-di-μ-chlororhodium(I) (32.1 mg, 82.6 μmol) and 5,10,15,20-tetraphenylporphyrin (50.0 mg, 81.3 μmol) were dissolved in toluene. The mixture was refluxed overnight. The solvent was evaporated, and the residue was purified by column chromatography (chloroform). Red powder of TPP rhodium chloride (**C_0-Rh**) was obtained (33.9 mg, 45.1 μmol). A part of **C_0-Rh** (7.7 mg, 10.25 μmol) was added to a solution of 4-phenylpyridine (1.7 mg, 11.0 μmol) in $CHCl_3$ (2 mL). The mixture was stirred for 1 h at 70 °C, and the solvent was evaporated *in vacuo*. Purification by column chromatography (silica, chloroform), GPC (chloroform) and HPLC (dichloromethane) gave **C_0-Rh-1** (2.3 mg, 2.54 μmol, 25%) as red powder. ESI-HRMS (*m*/*z*) $[M+Na]^+$ calcd for $C_{55}H_{37}N_5ClRhNa$: 928.1685; found: 928.1693. ^{1}H NMR ($CDCl_3$, 500 MHz, TMS) δ 1.01 (d, *J* = 6 Hz, 2H), 5.28 (d, *J* = 6 Hz, 2H), 6.53 (d, *J* = 8 Hz, 2H), 6.97 (t, *J* = 8 Hz, 2H), 7.05−7.06 (m, 1H), 7.69−7.77 (m, 12H), 8.12 (d, *J* = 8 Hz, 4H), 8.33−8.35 (m, 4H), 8.90 (s, 8H).

2-Coordinated 5,10,15,20-tetrakisphenylporphyrin rhodium chloride (C_0-Rh-2).
Yield: 19%, red powder. ESI-HRMS (*m*/*z*) $[M+Na]^+$ calcd for $C_{58}H_{43}N_5ClRhNa$: 970.2154; found: 970.2184. ^{1}H NMR ($CDCl_3$, 500 MHz, TMS) δ 0.43 (s, 3H), 0.76 (s,

1H), 0.82 (s, 6H), 0.86 (d, J = 6 Hz, 1H), 4.72 (d, J = 6 Hz, 1H), 6.61 (d, J = 8 Hz, 2H), 6.81 (t, J = 8 Hz, 1H), 7.68−7.70 (m, 4H), 7.75−7.77 (m, 8H), 8.03 (d, J = 8 Hz, 4H), 8.37−8.38 (m, 4H), 8.89 (s, 8H).

1-Coordinated 5,10,15,20-tetrakis(4-docosyloxyphenyl)porphyrin rhodium chloride (C_{22}-Rh-1).

Yield: 21%, red powder. MALDI TOF-MS (m/z) $[M-C_{11}H_9N]^+$ calcd for $C_{132}H_{204}N_4O_4ClRh$: 2047.462; found: 2047.521. ^{1}H NMR ($CDCl_3$, 500 MHz, TMS) δ 0.84 (d, J = 6 Hz, 2H), 0.88 (t, J = 7 Hz, 12H), 0.98 (d, J = 6 Hz, 2H), 1.25−1.48 (m, 144H), 1.62 (quint, 7 Hz, 8H), 1.98 (quint, 7 Hz, 8H), 4.24 (t, J = 7 Hz, 8H), 5.24 (d, J = 6 Hz, 2H), 6.51 (d, J = 8 Hz, 2H), 6.96 (t, J = 8 Hz, 2H), 7.05 (t, J = 8 Hz, 1H), 7.22 (dd, J_1 = 8 Hz, J_2 = 2 Hz, 4H), 7.28−7.29 (m, 4H), 8.02 (dd, J_1 = 8 Hz, J_2 = 2 Hz, 4H), 8.22 (dd, J_1 = 8 Hz, J_2 = 2 Hz, 4H), 8.92 (s, 8H).

2-Coordinated 5,10,15,20-tetrakis(4-docosyloxyphenyl)porphyrin rhodium chloride (C_{22}-Rh-2).

Yield: 29%, red powder. MALDI TOF-MS (m/z) $[M-C_{14}H_{15}N]^+$ calcd for $C_{132}H_{204}N_4O_4ClRh$: 2047.462; found: 2047.532. ^{1}H NMR ($CDCl_3$, 500 MHz, TMS) δ 0.40 (s, 3H), 0.73 (s, 1H), 0.80 (s, 6H), 0.84 (d, J = 6 Hz, 1H), 0.88 (t, J = 7 Hz, 12H), 1.25−1.48 (m, 144H), 1.62 (quint, J = 7 Hz, 8H), 1.98 (quint, J = 7 Hz, 8H), 4.24 (t, J = 7 Hz, 8H), 4.68 (d, J = 6 Hz, 1H), 6.59 (d, J = 8 Hz, 2H), 6.79 (t, J = 8 Hz, 1H), 7.21 (dd, J_1 = 8 Hz, J_2 = 2 Hz, 4H), 7.28 (dd, J_1 = 8 Hz, J_2 = 2 Hz, 4H), 7.92 (dd, J_1 = 8 Hz, J_2 = 2 Hz, 4H), 8.25 (dd, J_1 = 8 Hz, J_2 = 2 Hz, 4H), 8.92 (s, 8H).

1-Coordinated 5,10,15,20-tetrakis(4-triacontyloxyphenyl)porphyrin rhodium chloride (C_{30}-Rh-1).

Yield: 33%, red powder. MALDI TOF-MS (m/z) $[M-C_{11}H_9N+H]^+$ calcd for $C_{164}H_{269}N_4O_4ClRh$: 2496.971; found: 2496.729. ^{1}H NMR ($CDCl_3$, 500 MHz, TMS) δ 0.86 (t, 12H), 0.98 (d, J = 7 Hz, 2H), 1.25−1.48 (m, 208H), 1.62 (quint, J = 7 Hz, 8H), 1.98 (quint, J = 7 Hz, 8H), 4.24 (t, J = 7 Hz, 8H), 5.24 (d, J = 7 Hz, 2H), 6.51 (d, J = 8 Hz, 2H), 6.96 (t, J = 8 Hz, 2H), 7.05 (t, J = 8 Hz, 1H), 7.22−7.29 (m, 8H), 8.02 (dd, J_1 = 8 Hz, J_2 = 2 Hz, 4H), 8.02 (dd, J_1 = 8 Hz, J_2 = 2 Hz, 4H), 8.86 (s, 8H).

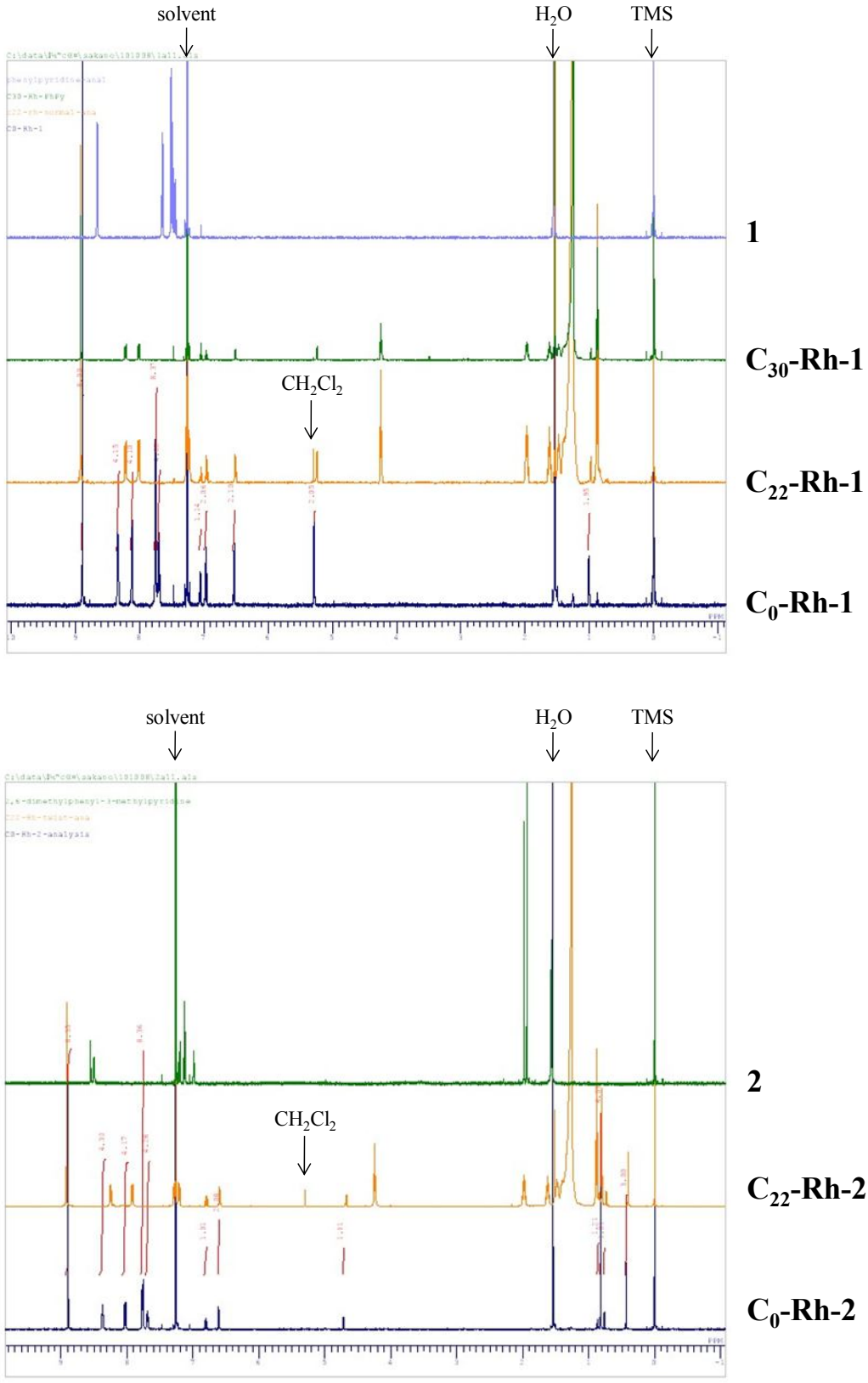

Figure 7. NMR charts of the synthesized compounds.

2. **STM Measurements.**

All STM experiments were performed at room temperature and ambient conditions. The STM images were acquired with a Digital Instrument Multimode Nanoscope IIIa and obtained at liquid-solid interface. All STM images were acquired in the constant current mode. The STM tips were electrochemically etched in a $CaCl_2$/HCl aqueous solution from Pt/Ir (80/20, diameter 0.25 mm) wire. Highly oriented pyrolytic graphite purchased from the Veeco Metrology Group was used as a substrate. The calibration of the piezoelectric position was verified by atomic resolution imaging of graphite (x- and y-directions) and by the height of single steps on the graphite surface (z-direction). Concentrations of the solution used for STM measurements were checked by absorption spectroscopy (Abs_{soret} = 0.03 to 2.0, light path 4 mm).

3. **X-ray Crystallography.**

C_0-Rh-1 and **C_0-Rh-2** were recrystallized from acetone and methanol, respectively, to give red needles in both cases. X-ray crystallographic analysis was performed using a Bruker APEX II diffractometer (55 kV, 35 mA) with Mo Kα radiation. The data were collected as a series of ω-scan frames. Data reduction was performed using SAINT software and the cell constants were calculated by the global refinement. Absorption correction was performed numerically based on the measured crystal shape. The structure was solved by direct methods using SHELXS and refined by full least-squares on F^2 using SHELXL.[16] The positions of all hydrogen atoms were calculated geometrically and refined by the riding model. CCDC 814313 and 814314 contain the supplementary crystallographic data for **C_0-Rh-1** and **C_0-Rh-2**, respectively.

4. STM image of C_{16}-2H, C_{22}-2H, and C_{30}-2H

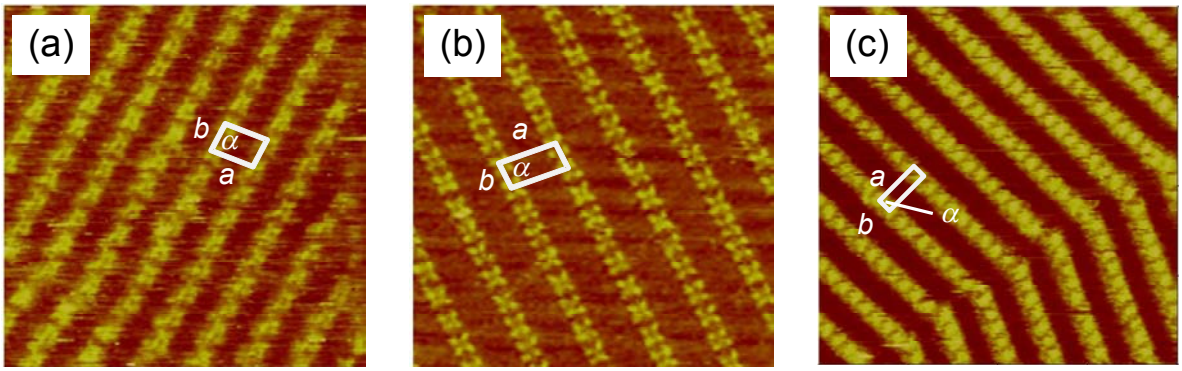

Figure 8. STM images at the liquid−HOPG interface in the constant current mode: (a) **C_{16}-2H** (1-phenyloctane, 25 × 25 nm^2, I_{set} = 30 pA, V_{bias} = −1.0 V); (b) **C_{22}-2H** (1-phenyloctane, 25 × 25 nm^2, *I*set = 30 pA, V_{bias} = +1.0 V); (c) **C_{30}-2H** (1,2,4-trichlorobenzene, 40 × 40 nm^2, I_{set} = 30 pA, V_{bias} = −1.0 V).

5. Relationship between carbon atom number of side chain and lattice parameter *a*

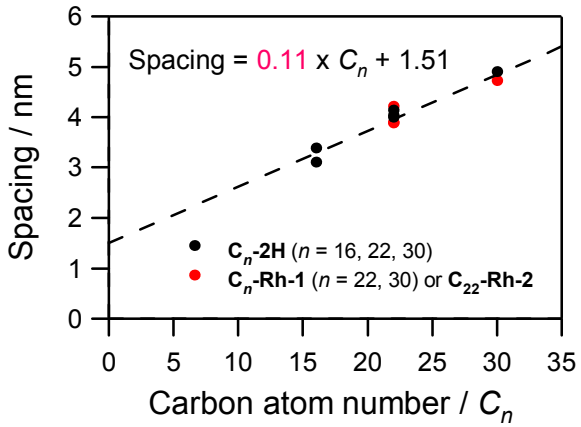

Figure 9. Relationship between the carbon atom number (C_n) of side chain and the lattice parameter *a* for TPPs **C_{16}-2H**, **C_{22}-2H**, **C_{30}-2H**, **C_{22}-Rh-1**, **C_{22}-Rh-2**, and **C_{30}-Rh-1**. Linear fitting of the plot gives the slope of 0.11 nm per carbon atom.

6. Lattice parameters of unit cell for TPPs

Table 3. Obtained lattice parameters of unit cell.

compound	solvent		*a*/nm	*b*/nm	α/°
C_{16}-2H (Figure 8a)	phenyloctane		3.1	2.0	83
C_{22}-2H (Figure 8b)	phenyloctane		4.1	1.9	84
C_{30}-2H (Figure 8c)	1,2,4-trichlorobenzene		4.9	1.7	86
C_{16}-2H+C_{22}-2H (Figure 4a)	phenyloctane	smaller larger	3.4 4.0	1.8 1.6	89 88
C_{22}-Rh-1 (Figure 3a)	ocatanoic acid		3.9	1.8	71
C_{22}-Rh-1+C_{22}-Rh-2 (Figure 3b)	ocatanoic acid		4.2	2.3	82
C_{30}-Rh-1+C_{22}-Rh-2 (Figure 5a)	ocatanoic acid	smaller larger	3.9 4.7	1.7 1.7	85 83

Notes and References

(1) C. Joachim, J. K. Gimzewski, A. Aviram, *Nature* **2000**, *408*, 541–548.; A. Nitzan, M. A. Ratner, *Science* **2003**, *300*, 1384-1389.; A. Salomon, D. Cahen, S. Lindsay, J. Tomfohr, V. B. Engelkes, C. D. Frisbie, *Adv. Mater.* **2003**, *15*, 1881-1890.; C. Joachim, M. A. Ratner, *Proc. Natl. Acad. Sci. U.S.A.* **2005**, *102*, 8801-8802.; N. J. Tao, *Nat. Nanotechnol.* **2006**, *1*, 173–181.; P. S. Weiss, *Acc. Chem. Res.* **2008**, *41*, 1772–1781.; K. Moth-Poulsen, T. Bjørnholm, *Nat. Nanotechnol.* **2009**, *4*, 551-556.

(2) M. A. Reed, C. Zhou, C. J. Muller, T. P. Burgin, J. M. Tour, *Science* **1997**, *278*, 252–254.; M. T. Gonzalez, S. M. Wu, R. Huber, S. J. van der Molen, C. Schonenberger, M. Calame, *Nano Lett.* **2006**, *6*, 2238–2242.; M. Tsutsui, M. Taniguchi, K. Yokota, T. Kawai, *Nat. Nanotechnol.* **2010**, *5*, 286–290.

(3) B. Xu, N. J. Tao, *Science* **2003**, *301*, 1221–1223.

(4) L. Venkataraman, J. E. Klare, C. Nuckolls, M. S. Hybertsen, M. L. Steigerwald, *Nature* **2006**, *442*, 904–907.; D. Vonlanthen, A. Mishchenko, M. Elbing, M. Neuburger, T. Wandlowski, M. Mayor, *Angew. Chem. Int. Ed.* **2009**, *48*, 8886–8890.; A. Mishchenko, D. Vonlanthen, V. Meded, M. Bürkle, C. Li, I. V. Pobelov, A. Bagrets, J. K. Viljas, F. Pauly, F. Evers, M. Mayor, T. Wandlowski, *Nano Lett.* **2010**, *10*, 156–163.

(5) L. A. Bumm, J. J. Arnold, T. D. Dunbar, D. L. Allara, P. S. Weiss, *J. Phys. Chem. B* **1999**, *103*, 8122–8127.

(6) K. Moth-Poulsen, L. Patrone, N. Stuhr-Hansen, J. B. Christensen, J.-P. Bourgoin, T. Bjørnholm, *Nano Lett.* **2005**, *5*, 783–785.; S. Wakamatsu, S. Fujii, U. Akiba, M. Fujihira, *Jpn. J. Appl. Phys.* **2006**, *45*, 2736–2742.

(7) J. Otsuki, *Coord. Chem. Rev.* **2010**, *254*, 2311-2341.; T. Ikeda, M. Asakawa, M. Goto, K. Miyake, T. Ishida, T. Shimizu, *Langmuir* **2004**, *20*, 5454–5459.

(8) UV-vis spectrum of the ligand-coordinated porphyrin in octanoic acid showed 3nm of red-shift compared with the ligand-free porphyrin, suggesting that the pyridyl ligand is bound to the porphyrin template. See M. Hoshino, H. Seki, K. Yasufuku, H. Shizuka, *J. Phys. Chem.* **1986**, *90*, 5149-5153.

(9) X. Qiu, C. Wang, Q. Zeng, B. Xu, S. Yin, H. Wang, S. Xu, C. Bai, *J. Am. Chem. Soc.* **2000**, *122*, 5550–5556.; H. Wang, C. Wang, Q. Zeng, S. Xu, S. Yin, B. Xu, C. Bai, *Surf. Interface Anal.* **2001**, *32*, 266–270.

(10) J. Otsuki, S. Kawaguchi, T. Yamakawa, M. Asakawa, K. Miyake, *Langmuir* **2006**, *22*, 5708–5715.

(11) F. Tao, J. Goswami, S. L. Bernasek, *J. Phys. Chem. B* **2006**, *110*, 19562–19569.

(12) A. C. Spivey, L. Shukla, J. F. Hayler, *Org. Lett.* **2007**, *9*, 891–894.

(13) J. H. van Esch, M. C. Feiters, A. M. Peters, R. J. M. Nolte, *J. Phys. Chem.,* **1994**, *98*, 5541–5551.

(14) J. Otsuki, S. Kawaguchi, T. Yamakawa, M. Asakawa, K. Miyake, *Langmuir* **2006**, *22*, 5708–5715.

(15) T. Ikeda, M. Asakawa, M. Goto, K. Miyake, T. Ishida, T. Shimizu, *Langmuir* **2004**, *20*, 5454–5459.

(16) *APEX2 Software Package ver. 2.0*, Bruker AXS, Madison, WI 2005.

Chapter 4

Chronological Change from Face-On to Edge-On Ordering of Zinc Tetraphenylporphyrin at Phenyloctane–Highly Oriented Pyrolytic Graphite Interface

Abstract

Self-assembled structure of alkoxy- and *N*-alkylcarbamoyl- substituted zinc tetraphenylporphyrin at liquid–HOPG interface was observed by using scanning tunneling microscopy. The alkoxy porphyrin showed phase transition from face-on to edge-on ordering. The phase transition requires the close packed structure of alkoxy porphyrin. The chronological change of the ordering was traced to show the existence of several types of Ostwald ripening including two-step phase transition from small edge-on to face-on furthermore to edge-on orderings. On the other hand, the *N*-alkylcarbamoyl porphyrin showed persistent edge-on ordering and the ordering was analyzed by Moiré pattern. Although the edge-on ordering is observed only in the non-polar solvent, the orderings have potential application to the charge and energy transfer.

This work has been presented in *Chem. Asian J.* **2012**, *7*, 394-399, essentially in the same form.

Introduction

The investigation of the molecular behaviors with molecular resolution is important for the bottom-up fabrication of molecular electronic device. Molecular imaging of the 2-dimensional (2-D) structure formed at a solid surface or a liquid-solid interface provides information on the molecular alignment and the molecular dynamics with distinguishing individual molecule.[1] Among various imaging methods, scanning tunneling microscopy (STM) at liquid–HOPG interface, which visualize self-assembled monolayer (SAM) of solute molecule at the interface, has been being used widely because of its very high resolution.[2] At the liquid-solid interface, adsorbed molecules on the surface are in equilibrium with the molecules in solution and the formation of the 2-D ordering is a very good model of crystallization. By real-time STM observation at the liquid-solid interface, dynamic behaviors of individual molecules can be accessed: Otsuki et al. reported dynamic rotation of double-decker porphyrins,[3] De Feyter et al. reported conformational dynamics of six-legged molecules,[4] Fichou et al. reported phase transition of the alkylated hexabenzocoronene on the *n*-pentacontane template,[5] and Flynn et al. reported frustrated Ostwald ripening of 2-D chiral reorientation of racemic compounds.[6] Ostwald ripening, which is defined as the growth of the larger domains at the expense of dissolving smaller domains, is considered as intrinsic phenomenon observed in the 2-D structure at the interface and the detailed study with molecular resolution is possible by using STM.[7]

In terms of molecular electronics, porphyrin molecules have potential application to the molecular wire and photovoltaic cell because of their high conductance in molecular wire[8] and high carrier mobility in 1-D aggregates.[9] Alkyl-substituted tetraphenylporphyrin (TPP) is known to form physisorbed 2-D structure at liquid–HOPG interface and the supramolecular architectures of TPP have been analyzed by STM.[10] The type of adsorption is classified into face-on (porphyrin is parallel to the interface) and edge-on (porphyrin is perpendicular to the interface) manners. Since metal porphyrins in face-on manner can have the axial ligand on the metal surface, they are applicable to the conductance measurement by STM.[11] Although edge-on ordering is often associated with columnar stacking and has the potential application to electron and exciton transport,[12] there are only a few reports on the edge-on orderings.[13] Up to now, best strategies for the construction of edge-on orderings of simple TPPs are to use the π-π stacking of metalloporphyrin and hydrogen bond between the side chains.[13b] In some cases, phase transition from the face-on to the edge-on ordering was observed.[13a] By taking advantage of STM method, in

principle, the phase transition can be traced with distinguishing individual molecule.

Herein, we report on the chronological change of the ordering of alkoxy-substituted zinc TPPs at 1-phenyloctane–HOPG interface by using STM. Real-time observation of such transition helps us to understand the mechanism of the transition.[14] Formation of the densely stacked edge-on ordering of alkylcarbamoyl-substituted zinc TPPs on the HOPG is also reported.

Results and Discussion

Synthesis

Docosyloxy-substituted TPP (**C_{22}O-2H**) and the corresponding zinc complex (**C_{22}O-Zn**) and *N*-hexadecylcarbamoyl-substituted TPP (**C_{16}A-2H**) and the corresponding zinc complex (**C_{16}A-Zn**) were synthesized (Scheme 1). For the synthesis of **C_{22}O-2H**, Williamson method was applied and for the synthesis of **C_{16}A-2H**, DCC coupling was used. The detail of the synthetic procedure is described in Supporting Information. Long alkyl chains assist the molecules to form the SAMs due to the van der Waals interaction between alkyl chains and HOPG substrate.[10] The characterization of the synthesized compounds was carried out by ^{1}H NMR spectroscopy and mass spectrometry.

Scheme 1. Synthesis of porphyrins.

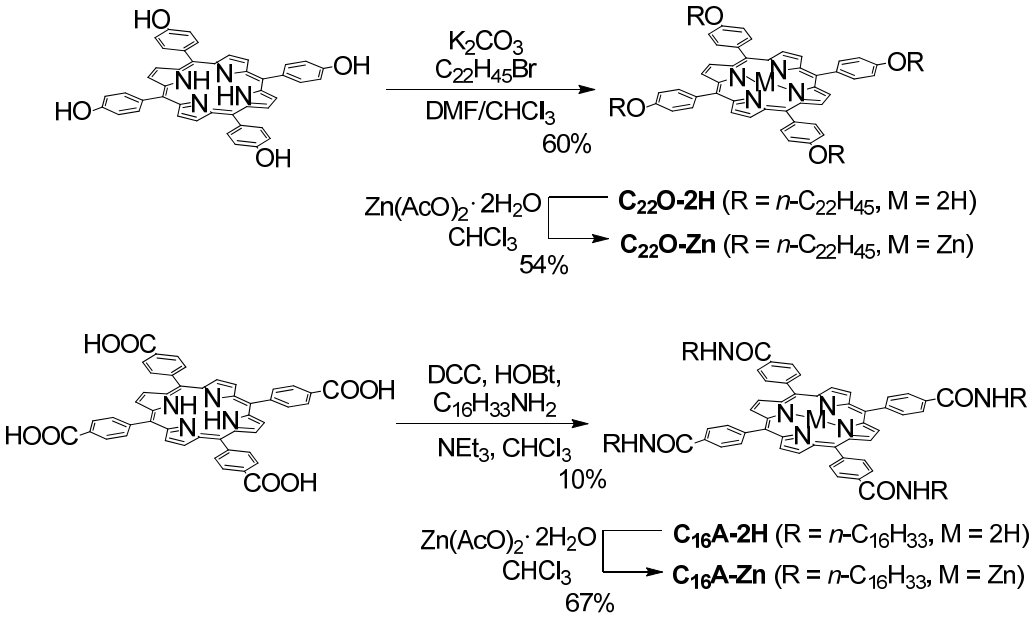

STM Measurement of Alkoxy Porphyrin

2-D self-assembled structures of **C_{22}O-2H** and **C_{22}O-Zn** were analyzed by STM at the liquid–HOPG interface. As shown in Figure 1a, **C_{22}O-2H** formed 2-D ordering at the 1-phenyloctane–HOPG interface. Docosyloxy chains are interdigitated in dark stripes, and central TPP cores are located in a face-on manner to HOPG substrate. The lattice parameters of the unit cell $a \times b$ and α were 4.1 ± 0.2 nm × 1.9 ± 0.2 nm and 84°.[15] In the case of zinc complex **C_{22}O-Zn**, although a face-on structure was observed in the beginning, the structure started to show a chronological change. Just after dropping a solution of **C_{22}O-Zn** onto a HOPG substrate, face-on ordering was observed as shown in Figure 1c. The lattice parameters were determined to be 2.9 ± 0.2 nm × 2.3 ± 0.2 nm and 72°. This lattice is smaller than that observed for **C_{22}O-2H**, indicating **C_{22}-Zn** are close packed in this lattice. The reduction of the lattice size would derive from the dissolution of alkyl chains into solution. As time goes by, the face-on ordering transformed to the edge-on herringbone ordering (5.2 nm × 0.61 nm and 82°) as shown in Figure 1d. When **C_{22}O-Zn** was mixed with the excess of pyridine *in situ*, which binds to Zn ($K = 2.4 \times 10^3$ M^{-1}), only face-on ordering was observed (Figure 1b).[16] Each TPPs had a bright spot derived from pyridine ligand at the center of the TPP ring. Axial coordinated pyridine would inhibit the phase transition to the edge-on ordering.[13a]

Details of the edge-on structure were analyzed by high resolution STM image shown in Figure 1e. Each **C_{22}O-Zn** is represented by edge-on TPP core and dark and bright side chains in the herringbone structures. Intracolumnar TPP distance was 0.61 nm, which enable us to estimate the tilt angle normal to the porphyrin plane to be 33° by assuming π-π stacking distance of 0.34 nm (Figure 1g). By analyzing HOPG orientation with increased current and decreased bias voltage (I_{set} = 50 pA, V_{bias} = −10 mV), the dark chains are found to be aligned along <1-210> direction. Difference of the contrast was due to the orientation of HOPG substrate underneath adsorbed molecules.[17] Top view of the molecular model is shown in Figure 1f. These bright and dark chains are not symmetric to TPP ring with angles of 140° and 123°, but they are symmetric to 1-D columnar direction with angle of 41 ± 1°. The leftmost column of four in Figure 1e is in inverse direction from other columns. The contrast of side chains in the leftmost column is enhanced, that is, bright chains are brighter and dark chains are darker than those in right columns. The contrast must be derived from the difference in geometric height of side chains. Moreover the left phenyl ring of TPP in the leftmost column was brightest of all the TPP cores (Figure 1e). This result

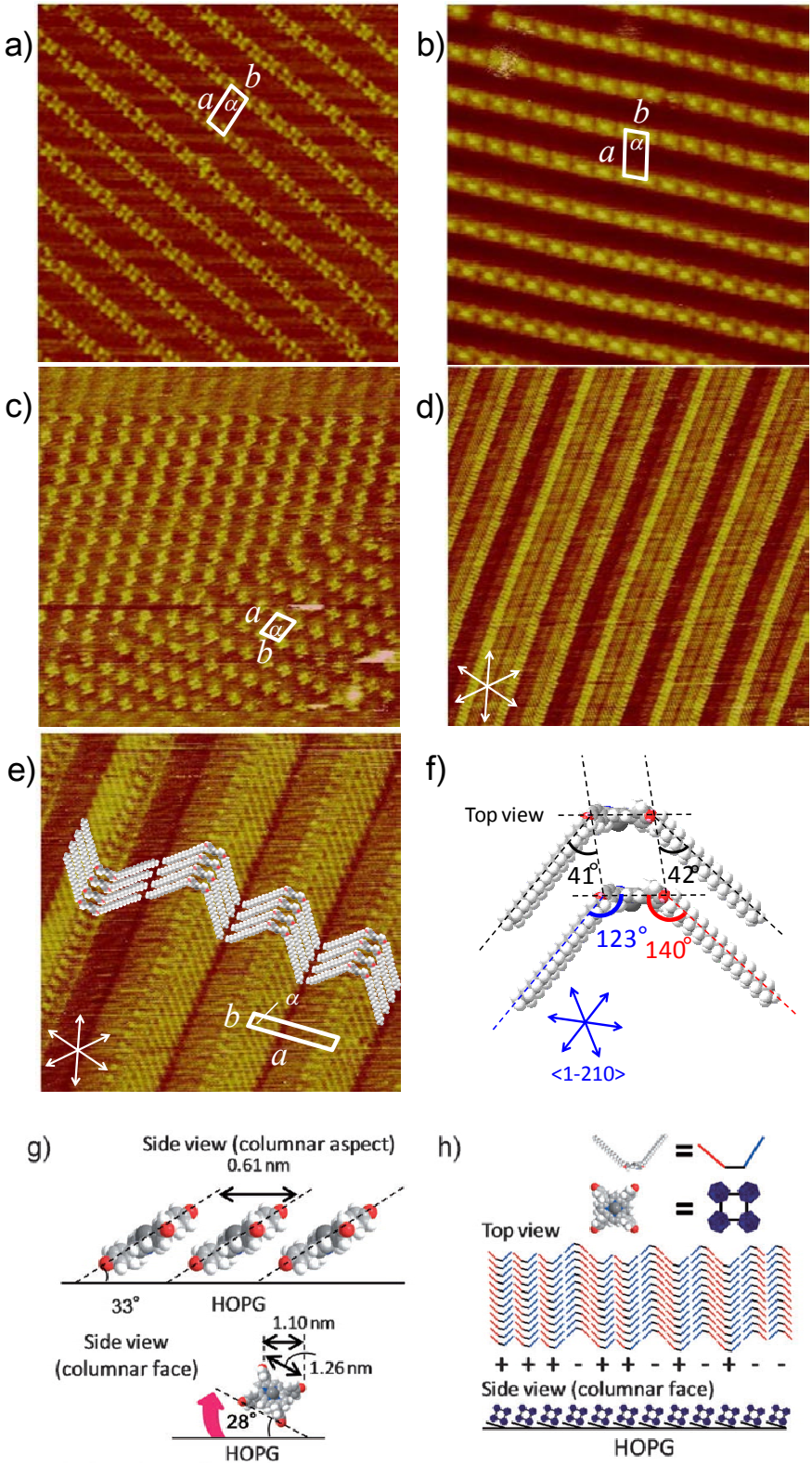

Figure 1. (a) STM image of **C_{22}O-2H** (35 × 35 nm^2, I_{set} = 30 pA, V_{bias} = +1.0 V); (b) **C_{22}O-Zn** (1 × 10^{-5} M, 7 μL) containing 2 μL of pyridine (35 × 35 nm^2, I_{set} = 30 pA, V_{bias} = −1.0 V, molar ratio of [**C_{22}O-Zn**-pyridine] / [**C_{22}O-Zn**] in solution is calculated

to be 8.5×10^3); (c) **C_{22}O-Zn** 100 min after dropping a solution onto the surface (40×40 nm^2, I_{set} = 30 pA, V_{bias} = −1.0 V, 1×10^{-5} M); (d) 250 min after dropping (50×50 nm^2, I_{set} = 30 pA, V_{bias} = −1.0 V, 1×10^{-5} M); (e) **C_{22}O-Zn** with molecular models (20×20 nm^2, I_{set} = 30 pA, V_{bias} = −1.0 V). (f) Top view, (g) side view and (h) schematic illustration of **C_{22}O-Zn** in the herringbone structure. Four docosyloxy chains are omitted from the side view for clarity. White parallelograms in the images show the unit cells and white double-headed arrows show the <1-210> direction of HOPG. STM image were taken at the 1-phenyloctane–HOPG interface in the constant current mode.

suggests that all the TPP cores were leaned to the right as shown in Figure 1g. This is the reason why the difference in the contrast of side chains between upward and downward columns was observed. TPP core part had the width of 1.10 nm which is shorter than the nearest O-O distance (1.26 nm) in a TPP determined by X-ray crystallographic analysis,[18] indicating that the tilt angle parallel to the TPP plane is 28° as shown in Figure 1g. Figure 1h shows the schematic illustration of wide-scale herringbone ordering. Upward and downward 1-D columns which marked as + and − are randomly blended in the domain. When the orderings with + and − directions have the same structure, the tilt angle parallel to the TPP will be opposite depending on the direction, but the ordering in Figure 1e shows that all the TPP rings were monotonously leaned to one direction. It means that each column strongly interacts with ambilateral

Structure of the 2-D ordering was investigated for the samples with different concentrations (Figure 2). Lower concentration solution yielded faulty ordering and higher concentration solution yielded a multilayer which was composed of face-on orderings stacked each other with various directions. In both cases, lattice parameters were similar to **C_{22}O-2H** in Figure 1a rather than **C_{22}O-Zn** in Figure 1c (Table 1). These orderings are considered to be the polymorph of that observed in Figure 1c. No phase transition occurred from these orderings. This result indicates that there is an optimal concentration to have close packed structure[19] and formation of the close packed face-on ordering would play a key role for the phase transition from face-on to edge-on ordering.

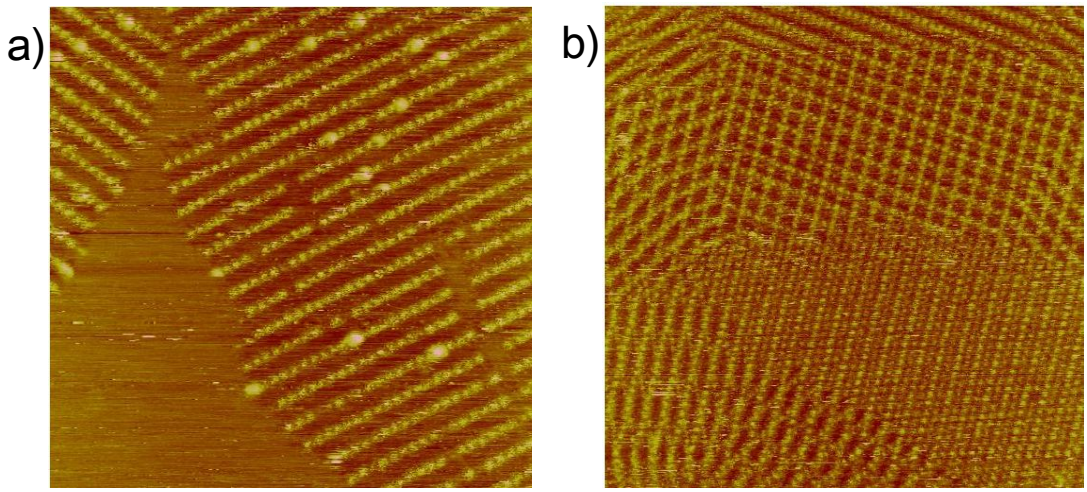

Figure 2. STM images of **C_{22}O-Zn** at the 1-phenyloctane−HOPG interface: (a) low concentration solution (80 × 80 nm^2, I_{set} = 30 pA, V_{bias} = −1.0 V, 1 × 10^{-6} M); (b) high concentration solution (80 × 80 nm^2, I_{set} = 30 pA, V_{bias} = −1.0 V, 5 × 10^{-4} M).

Observation of Phase Transition

To analyze the phase transition process from the face-on to the edge-on ordering, chronological change of the wide-scale STM image of **C_{22}O-Zn** was traced (Figure 3). At 120 minutes after dropping a solution onto the substrate, domains of the edge-on, the face-on, and the complicated orderings were observed. White, red, and blue lines in Figure 3a show some of the domain boundaries. The dashed lines in Figure 3b-e indicate the corresponding areas of the initial domains and the change of the ordering in these areas was traced. The position of the domain boundary was calibrated by the edge-structure of the HOPG substrate indicated by the black arrow at the bottom left corner.

At first, we focus on the close packed face-on ordering surrounded by blue line in Figure 3a. The domain changed to edge-on ordering after 18 minutes (see Figures 3a and 3c). Interestingly, the configuration of the edge-on ordering was completely the same as the one of upper edge-on ordering in Figure 3b. This phase transition is interpreted as 2-D Ostwald ripening at the domain boundary, that is, larger domains grow at the expense of dissolving smaller islands.[6,7] This result shows that 2-D Ostwald ripening to edge-on ordering occurs even if the initial ordering was face-on ordering.

Secondly, we focus on another domain surrounded by red line. This red domain was initially edge-on ordering with different direction from the neighboring edge-on domains (Figure 3a). After 9 minutes, the domain changed to the face-on ordering at the upper part (indicated by A) and to the edge-on ordering at the lower part (see Figure 3b). This phenomenon means the reversal phase transition from edge-on ordering to face-on ordering occurred. The initial edge-on ordering was surrounded by the larger edge-on and face-on orderings. This is also considered as 2-D Ostwald ripening controlled by the neighboring structure. As time goes by, the new face-on ordering faded out and merged to the edge-on ordering. This result shows the edge-on ordering had higher stability than the face-on ordering. The observed face-on ordering is an intermediate state and this phenomenon is a two-step Ostwald ripening.

Thirdly, we focus on the overall structure and domain boundaries. By simply comparing Figure 3a with 3e, many fragmented domains are found to be merged into the widespread one-directional edge-on orderings, although the face-on ordering at the upper-right corner was unchanged. Close examination reveals that there are two kinds of domain boundaries in the final large one-directional edge-on ordering: one is across the 1-D columnar direction indicated as B by black double headed arrow and the other along 1-D columnar direction indicated as C by white rectangle (Figure 3f).[20] Real-time observation revealed the movement of the boundaries. The position of the boundary B is found to have moved to lower direction when Figures 3c-e are compared. This result suggests that 2-D Ostwald ripening occurs also between the edge-on orderings of same direction. Boundary C was firstly observed in Figure 3b, which extended to lower direction in Figure 3c. This result suggests that boundary C between two edge-on domains grows with keeping its structure.

Overall, real-time observation of the phase transition behavior revealed that large one-directional edge-on orderings are formed by various phase transitions such as from face-on to edge-on orderings, from edge-on to edge-on orderings with and without changing the direction accompanied by elongation and shift of the boundaries. Especially, two-step phase transition behavior from small edge-on to face-on furthermore to most stable edge-on orderings clearly shows that phase transitions of both directions between face-on and edge-on orderings follow the Ostwald ripening rule.

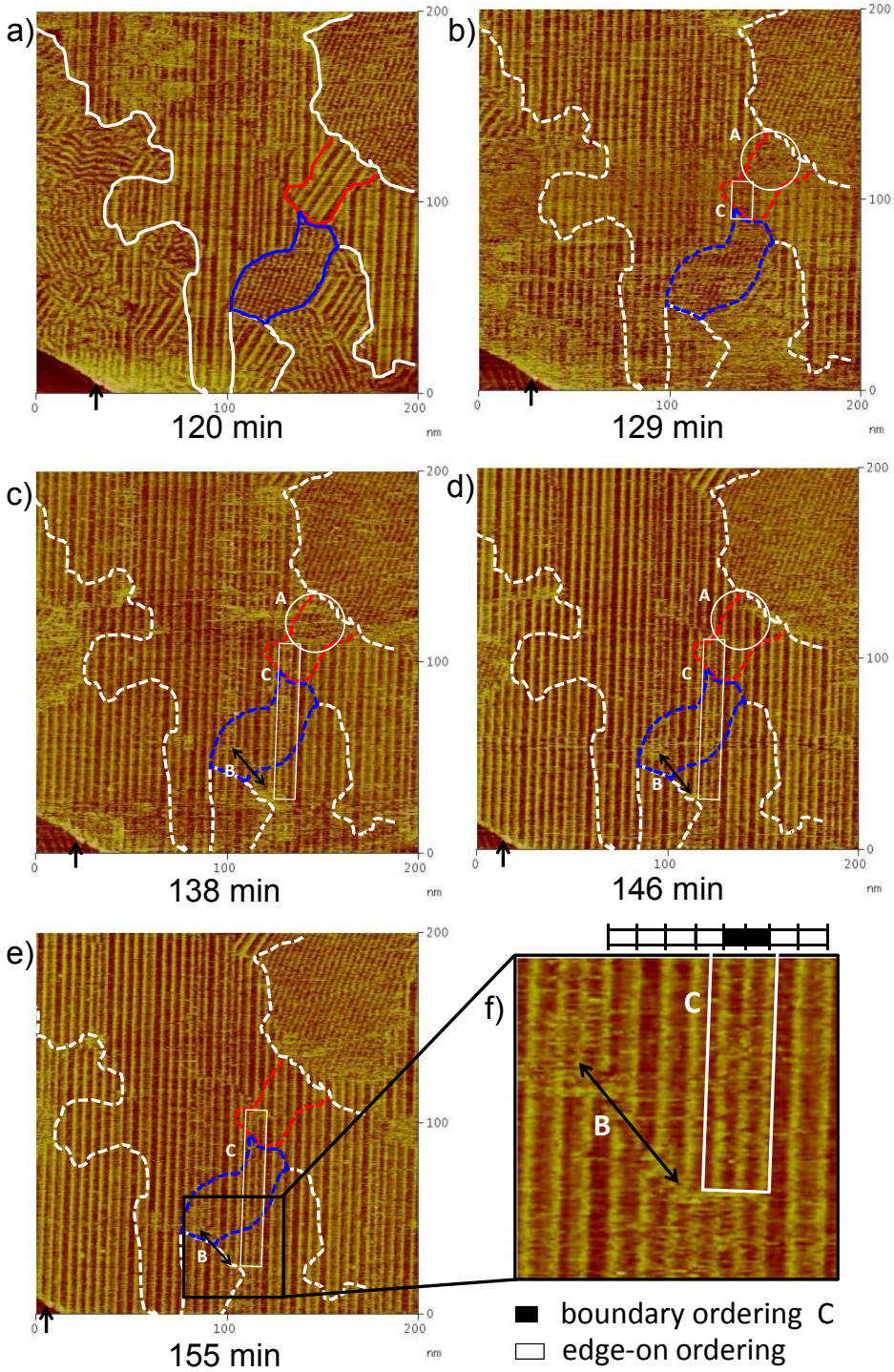

Figure 3. Chronological change of STM images of **C_{22}O-Zn** in the constant current mode at the 1-phenyloctane−HOPG interface (200 × 200 nm^2, I_{set} = 30 pA, V_{bias} = −1.0 V): (a) 120 min after dropping a solution onto the surface, (b) 129 min, (c) 138 min, (d) 146 min, (e) 155 min. (f) Expanded image of the boundary orderings among edge-on orderings (55 × 55 nm^2). Blue bars show the boundary orderings C and red bars show the edge-on orderings.

STM Measurement of *N*-Alkylcarbamoyl Porphyrin

For the construction of persistent edge-on orderings, intermolecular interaction needs to be enhanced. Zinc TPP having four *N*-alkylcarbamoyl groups (**C_{16}A-Zn**) is expected to have much higher intermolecular stacking assisted by hydrogen bonding[21] and was synthesized (Scheme 1). STM images of **C_{16}A-Zn** were observed several different conditions. When the cast film from chloroform solution is immersed in phenyloctane, a strongly stacked edge-on ordering was reproducibly produced as shown in Figure 4a. The lattice parameters were 4.8 ± 0.2 nm × 0.37 ± 0.01 nm and 88°.

By close examination, Figure 4a clearly shows the periodic Moiré pattern marked by white arrows which evidences that the ordering interferences with the HOPG underneath.[22] Since the TPP and side chains are along the direction of <1-210> and columnar direction along to <1-100>, Moiré distance ($T_{\text{Moiré}}$ = 2.48 nm) provides the precise intermolecular distance (T_{mol} = 0.364 nm) with very high accuracy according to the following equation 1.

$$T_{\text{mol}} = \left(\frac{T_{\text{HOPG}} \cdot T_{\text{Moiré}}}{T_{\text{Moiré}} \pm T_{\text{HOPG}}} \right) \qquad (1)$$

The intermolecular distance enables us to estimate the tilt angle normal to the porphyrin plane to be 69° by assuming π-π stacking distance of 0.34 nm (Figure 4b). Unlike edge-on ordering of **C_{22}O-Zn**, no special boundary was found in this edge-on ordering. After an addition of pyridine in situ, columnar structure of **C_{16}A-Zn** was persistent over several hours (Figure 4c), but when the pyridine was mixed ex situ into the self-assembled aggregates, only face-on orderings were observed (Figure 4d). These results show the columnar **C_{16}A-Zn** had the strong intermolecular stacking and strong adsorption onto HOPG substrate. Because it is easy to destruct the amide hydrogen bonding by polar solvent, an STM image was observed at the 1-octanoic acid–HOPG interface (Figure 4e). **C_{16}A-Zn** formed face-on orderings with lattice parameters of 3.4 nm × 1.8 nm and 81°. This ordering is similar to the reported structure of amide TPPs at the 1-heptanol–HOPG interface.[21] The observed edge-on ordering has a columnar stacking that is applicable to electron and exciton transport.

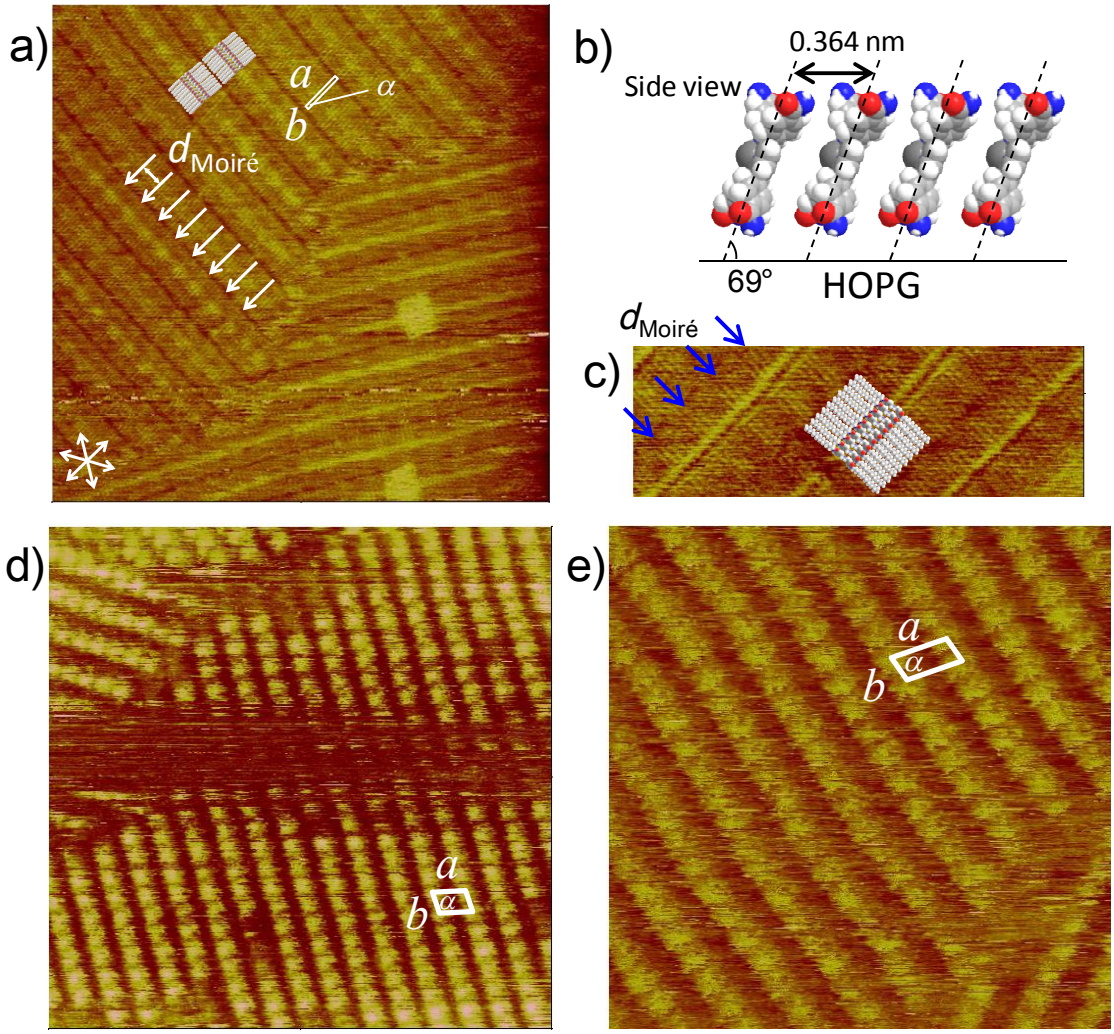

Figure 4. STM images of **C_{16}A-Zn** at the 1-phenyloctane–HOPG interface in the constant current mode with molecular models. (a) Cast film (50 × 50 nm^2, I_{set} = 20 pA, V_{bias} = −1.0 V): white double-headed arrows show the <1−210> direction of HOPG. (b) Molecular models: side view of **C_{16}A-Zn** on HOPG. Four hexadecyloxy chains are omitted for clarity. (c) Solution containing aggregates: pyridine (10 μL) was added in situ (23 × 8 nm^2, I_{set} = 20 pA, V_{bias} = −1.3 V). (d) Solution containing aggregates with 10 μL of pyridine. Pyridine was added *ex situ* (50 × 50 nm^2, I_{set} = 20 pA, V_{bias} = −1.2 V). (e) Image taken at the 1-octanoic acid−HOPG interface (30 × 30 nm^2, I_{set} = 30 pA, V_{bias} = −1.0 V).

Conclusions

We investigated the self-assembled structure of alkoxy- and *N*-alkylcarbamoyl-substituted zinc tetraphenylporphyrin at the solid–liquid interface by

using STM. The alkoxy porphyrin showed phase transition from face-on to edge-on orderings. The phase transition requires the close packed structure of alkoxy porphyrin. Chronological change revealed several types of Ostwald ripening including two-step phase transition from small edge-on to face-on furthermore to large edge-on orderings. By changing the side chain to *N*-alkylcarbamoyl groups, persistent edge-on orderings were constructed. The edge-on structure had the Moiré patterns by the interference with HOPG underneath. Although the edge-on ordering is observed only in the non-polar solvent, the orderings have potential application to the charge and energy transfer.

Table 1. Lattice parameters of the unit cell for TPPs at the 1-phenyloctane–HOPG interface.

sample	*C*/mol L^{-1}	ordering	lattice parameter			Molecular Area /nm^2
			a/nm	*b*/nm	α/°	
C_{22}O-2H	1×10^{-6}	face-on	4.1	1.9	84	7.7
C_{22}O-Zn	5×10^{-4}	face-on	3.9	1.9	84	7.4
C_{22}O-Zn	1×10^{-5}	face-on	2.9	2.3	72	6.3
C_{22}O-Zn	1×10^{-5}	edge-on	5.2	0.61	82	3.1
C_{22}O-Zn[a]	1×10^{-5}	face-on	4.2	2.2	81	9.6
C_{22}O-Zn	1×10^{-6}	face-on	3.9	1.9	83	7.4
C_{16}A-Zn	1×10^{-6}	edge-on	4.8	0.37	88	1.8
C_{16}A-Zn[a]	1×10^{-6}	face-on	3.2	2.0	79	6.3
C_{16}A-Zn[b]	1×10^{-6}	face-on	3.4	1.8	81	6.0

[a] with pyridine. [b] measured at the 1-octanoic acid–HOPG interface.

columns. During the phase transition from face-on to edge-on monolayer, 2-D density became doubled as summarized in Table 1.

Experimental Section

1. General.

All STM experiments were performed at room temperature and ambient conditions. The STM images were acquired with a Digital Instrument Multimode Nanoscope IIIa and obtained at liquid-solid interface. All STM images were acquired in the constant current mode. The STM tips were electrochemically etched in a $CaCl_2$/HCl aqueous solution from Pt/Ir (80/20, diameter 0.25 mm) wire. Highly

oriented pyrolytic graphite purchased from the Veeco Metrology Group was used as a substrate. Concentrations of the solution used for STM measurements were checked by absorption spectroscopy. Solutions of **C_{22}O-2H** and **C_{22}O-Zn** in 1-phenyloctane and a solution of **C_{16}A-Zn** in 1-octanoic acid for the STM measurements were prepared by mixing into the solvent with heating. Cast film of **C_{16}A-Zn** was prepared by drop casting from chloroform solution onto HOPG, and 1-phenyloctane was added to obtain a clear STM image after the evaporation of chloroform. The aggregate of **C_{16}A-Zn** in 1-phenyloctane was prepared by rapid injection of concentrated chloroform solution (10 μL) into 1-phenyloctane (3 mL) and shaking. Formation of the aggregate was confirmed by absorption spectroscopy as shown in Supporting Information. The synthesis and characterization of the compounds are described below.

2. Syntheses of the materials

^{1}H NMR spectra were recorded on a JEOL JMN-A500 and a JEOL JMN-A400 instrument. Mass spectra were obtained by Bruker autoflex III MALDI-TOF mass spectrometer and Thermo Scientific Exactive mass spectrometer. All reactions were monitored by thin-layer chromatography carried out on 0.2 mm Merck silica gel plates (60F-254). Column chromatography was performed on silica gel (Nakarai, 70-230 mesh).

21,23-Dihidro-5,10,15,20-tetrakis(4-docosyloxyphenyl)porphyrin (C_{22}O-2H).[15]

1-Bromodocosane (696 mg, 1.79 mmol), K2CO3 (611 mg, 4.42 mmol) were added to a solution of 5,10,15,20-tetra(4-hydroxyphenyl)porphyrin (114.3 mg, 168 μmol) in dry DMF (20 mL). The solution was refluxed overnight. The DMF was evaporated in vacuo and chloroform was added to the crude. After refluxing overnight, the mixture was cooled to RT, filtrated and concentrated in vacuo. Purification by column chromatography (chloroform) gave **C_{22}O-2H** (193 mg, 101 μmol, 60%) as a purple powder. MALDI TOF-HRMS (*m*/*z*) $[M+H]^+$ calcd for $C_{132}H_{207}N_4O_4$: 1912.6112; found: 1912.6080. ^{1}H NMR (CD_2Cl_2, 500 MHz, TMS) δ −2.81 (s, 2H), 0.87 (s, 12H), 1.25−1.64 (m, 152H), 1.98 (quint, *J* = 8 Hz, 8H), 4.26 (t, *J* =7 Hz, 8H), 7.29 (d, *J* = 9 Hz, 8H), 8.11 (d, *J* = 9 Hz, 8H), 8.89 (s, 8H).

Zinc 5,10,15,20-tetrakis(4-docosyloxyphenyl)porphyrin (C_{22}O-Zn).

To a solution of **C_{22}O-2H** (59 mg, 30.8 μmol) in chloroform (20 mL) was added a solution of zinc acetate dihydrate (67.7 mg, 308 μmol) in methanol (2 mL). The mixture was refluxed for 1 h. After cooled to room temperature, the solvent was

removed under reduced pressure. After washed by methanol, the crude was purified by column chromatography (silica, chloroform) to yield zinc 5,10,15,20-tetrakis(4-docosyloxyphenyl)porphyrin (32.6 mg, 16.5 μmol, 54%) as a purple powder. ESI TOF-HRMS (*m*/*z*) $[M]^+$ calcd for $C_{132}H_{204}N_4O_4Zn$: 1973.5174; found: 1973.5203. ^1H NMR ($CDCl_3$, 400 MHz, TMS) δ 0.87 (t, *J* = 7 Hz, 12H), 1.25−1.52 (m, 144H), 1.63 (quint, *J* = 7 Hz, 8H), 1.99 (quint, *J* = 7 Hz, 8H), 4.26 (t, *J* = 7 Hz, 8H), 7.27 (d, *J* = 9 Hz, 8H), 8.11 (d, *J* = 9 Hz, 8H), 8.97 (s, 8H).

21,23-Dihidro-5,10,15,20-tetrakis(4-(*N*-hexadecylcarbamoyl)phenyl)porphyrin(C_{16} A-2H).

To a solution of 21,23-dihidro-5,10,15,20-tetrakis(4-carboxyphenyl)porphyrin (100 mg, 126 μmol) and triethylamine (1.0 mL) in chloroform (30 mL) was added 1-hexadecylamine (243 mg, 1.01 mmol) *N*,*N*'-dicyclohexylcarbodiimide (DCC) (208 mg, 1.01 mmol), 1,2,3-benzotriazole-1-ol (HOBt) (137 mg, 1.01 mmol). The mixture was stirred for 48h at room temperature. After a filtration, the resulting solution was evaporated under reduced pressure. The crude was purified by column chromatography (silica, chloroform mixed with 3% triethylamine) to yield 21,23-dihidro-5,10,15,20-tetrakis(4-(*N*-hexadecylcarbamoyl)phenyl)porphyrin (22.0 mg, 13.1 μmol, 10%) as a purple powder. MALDI TOF-HRMS (*m*/*z*) $[M+H]^+$ calcd for $C_{112}H_{163}N_8O_4$: 1684.2792; found: 1684.2776. ^1H NMR ($CDCl_3$, 500 MHz, TMS) δ −2.83 (s, 2H), 0.87 (t, *J* = 7 Hz, 12H), 1.25−1.53 (m, 106H), 1.76 (quint, *J* = 7 Hz, 8H), 3.64 (q, *J* = 7 Hz, 8H), 6.42 (t, *J* = 6 Hz, 4H), 8.16 (d, *J* = 8 Hz, 8H), 8.28 (d, *J* = 8 Hz, 8H), 8.82 (s, 8H).

Zinc 5,10,15,20-tetraksi(4-(*N*-hexadecylcarbamoyl)phenyl)porphyrin (C_{16}A-Zn).

To a solution of 5,10,15,20-tetrakis(4-(*N*-hexadecylcarbamoyl)phenyl) porphyrin (10.0 mg, 5.94 μmol) in chloroform (20 mL) was added a solution of zinc acetate dihydrate (13.0 mg, 59.4 μmol) in methanol (1 mL). The mixture was refluxed for 1h. After cooled to room temperature, the solvent was removed under reduced pressure. The crude was reprecipitated with methanol to yield zinc 5,10,15,20-tetrakis(4-(*N*-hexadecylcarbamoyl)phenyl)porphyrin (7.0 mg, 4.01 μmol, 67%) as a purple powder. MALDI TOF-MS (*m*/*z*) $[M]^+$ calcd for $C_{112}H_{160}N_8O_4Zn$: 1745.1849; found: 1745.1838. ^1H NMR ($CDCl_3$, 500 MHz, TMS) δ 0.87 (t, *J* = 7 Hz, 12H), 1.25−1.51 (m, 106H), 1.73 (quint, *J* = 7 Hz, 8H), 3.58 (q, *J* = 7 Hz, 8H), 6.41 (t, *J* = 6 Hz, 4H), 8.09 (d, *J* = 8 Hz, 8H), 8.27 (d, *J* = 8 Hz, 8H), 8.91 (s, 8H).

3. Benesi-Hildebrand plot for C_{22}O-Zn with pyridine

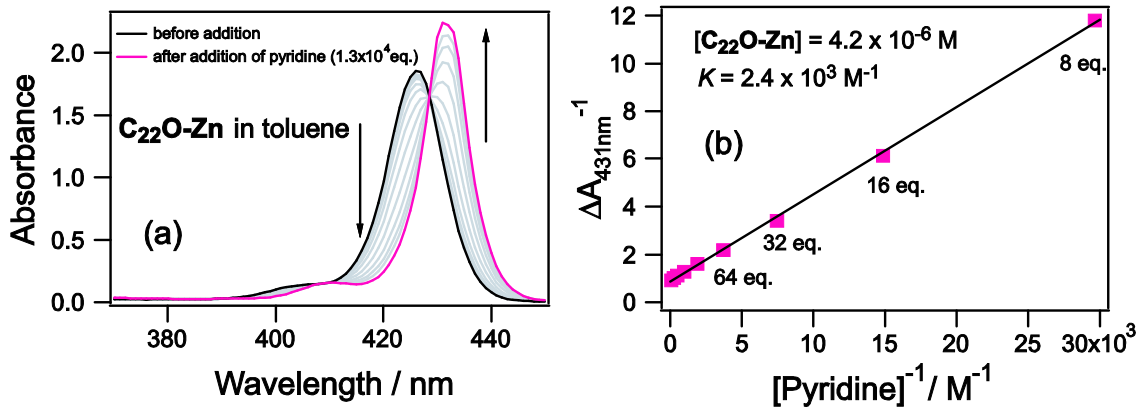

Figure 5. (a) Absorption spectral changes of **C_{22}O-Zn** (4.2×10^{-6} M) with an addition of pyridine in toluene, (b) Benesi-Hildebrand plot. The slope gives the binding constant between **C_{22}O-Zn** and pyridine ($K = 2.4 \times 10^3$ M^{-1}).

4. Preparation of C_{16}A-Zn aggregates in phenyloctane

C_{16}A-Zn cannot dissolve into 1-phenyloctane. Aggregates of **C_{16}A-Zn** were prepared by rapid injection of chloroform solution of **C_{16}A-Zn** into phenyloctane. Formation of the aggregates was confirmed by absorption spectrum as shown in Figure 6. Soret band showed blue shift from 426 nm in chloroform to 403 nm in 1-phenyloctane. This blue shift indicates the formation of *H*-type aggregates. With an addition of pyridine (10 μL), soret band was divided into two peaks at 403 nm and 441 nm. Peak at 441 nm is longer than monomer absorption band of **C_{16}A-Zn**, which indicates the formation of complex with pyridine.

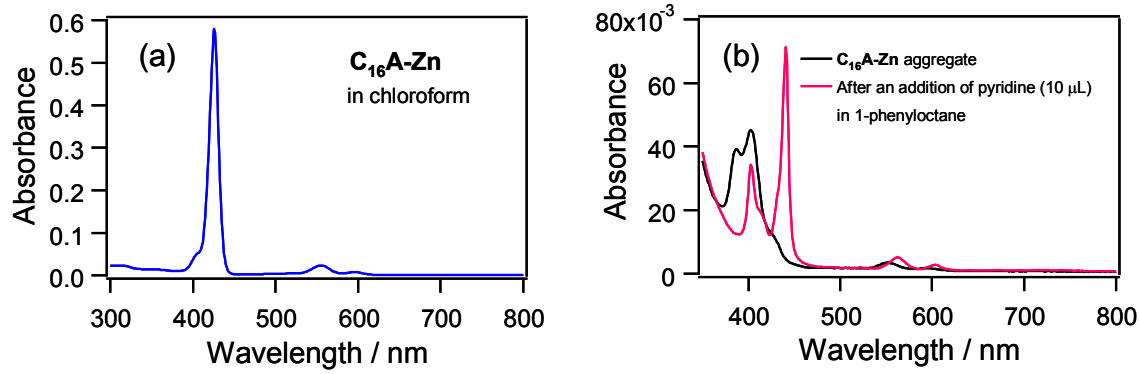

Figure 6. Absorption spectra of **C_{16}A-Zn**: (a) in chloroform; (b) in 1-phenyloctane.

5. STM images of C_{16}A-Zn aggregates at the 1-phenyloctane-HOPG interface.

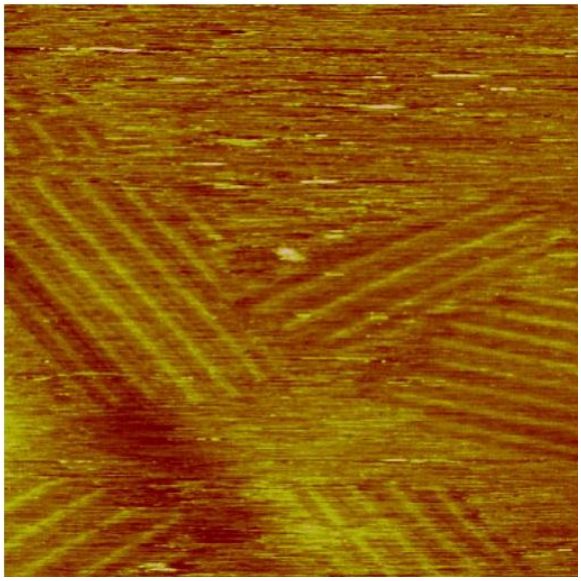

Figure 7. An STM image of **C_{16}A-Zn** aggregates at the 1-phenyloctane−HOPG interface (60 × 60 nm^2, I_{set} = 30 pA, V_{bias} = −1.0 V).

6. Calculation of the angular intervals among columnar herringbone structures

In general, when one-dimensional (1-D) columnar direction and <1-210> direction of HOPG are tilted by certain angle of θ, the periodic angular interval becomes 60° which is derived from C_6 symmetry of HOPG. When the columnar structure has a chiral isomer, the columnar direction and <1-210> direction are tilted by angle of $\pm\theta$. Therefore, the angles between the columnar directions become $60n°$ and $60n° \pm 2\theta$ as shown in Figure S4a. Even when the achiral molecule is used, adsorption-induced two-dimensional (2-D) chirality needs to be taken into consideration. In our case, when θ = 17° is assumed, the calculated angles are 34°, 60° and 94°, which is in good agreement with the observed angles of 33°, 58°, and 94°. 2-D chirality of the column was revealed by analyzing the consecutive angular intervals.

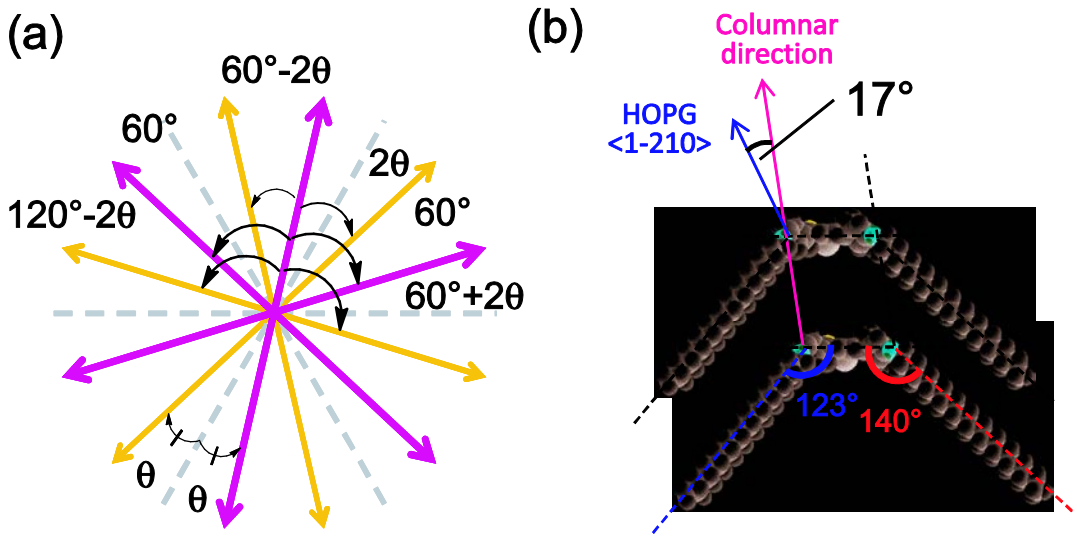

Figure 8. (a) General angular intervals among 1-D columnar direction tilted by certain angle of θ to <1-210> direction of HOPG. Purple and yellow double-headed arrows show the columnar directions. Both arrows are in chiral relationship. (b) An angular interval between columnar direction of the herringbone structure and <1-210> direction of HOPG.

7. Analysis of Moiré patterns

Moiré pattern was observed for **C_{16}A-Zn** in Figure 4. Moiré pattern was derived by the interference of two periodic waves which have close pitches. Given two pitches T_1 and T_2, the pattern is represented as $A_1 = \cos(2\pi\, x/T_1)$ and $A_2 = \cos(2\pi\, x/T_2)$. The sum becomes

$$A_1 + A_2 = \cos(2\pi\frac{x}{T_1}) + \cos(2\pi\frac{x}{T_2}) = 2\cos(\pi x(\frac{1}{T_1} - \frac{1}{T_2}))\cos(\pi x(\frac{1}{T_1} + \frac{1}{T_2})) \qquad \text{(S1)}$$

where T_1 and T_2 are the pitches of the original waves. Therefore, the pitch of the new wave is following:

$$\frac{1}{T_{\text{sum1}}} = \frac{1}{2}\left|\frac{1}{T_1} - \frac{1}{T_2}\right| \quad \text{and} \quad \frac{1}{T_{\text{sum2}}} = \frac{1}{2}\left(\frac{1}{T_1} + \frac{1}{T_2}\right) \qquad \text{(S2)}$$

that is,

$$T_{\text{sum1}} = 2\frac{T_1 T_2}{|T_1 - T_2|} \quad \text{and} \quad T_{\text{sum2}} = 2\left(\frac{T_1 T_2}{T_1 + T_2}\right) \qquad \text{(S3)}$$

Since the Moiré pattern is observed as longer pitch than the original pitches, second equation of T_{sum2} can be ignored. The observed interval between peaks is a half of the pitch. Therefore, the Moiré distance $T_{Moiré}$ can be expressed as follows:

$$T_{Moiré} = \frac{T_{HOPG} \cdot T_{mol}}{|T_{HOPG} - T_{mol}|} \qquad (S4)$$

where T_{HOPG} and T_{mol} are the pitches of the HOPG and adsorbed molecules. Intermolecular distance T_{mol} is thus calculated to be

$$T_{mol} = \left(\frac{T_{HOPG} \cdot T_{Moiré}}{T_{Moiré} \pm T_{HOPG}} \right) \qquad (S5)$$

Although this equation means that Moiré patterns give two possible intermolecular distances, they are easily distiguished by experimental data.

In the case of **C_{16}A-Zn**, Moiré patterns were along the <1-100> direction of HOPG underneath. By substitution of pitch of HOPG (T_{HOPG} = 0.426 nm) and Moiré distance ($T_{Moiré}$ = 2.48 nm) to above equation, T_{mol} is calculated to be 0.364 nm and 0.514 nm. STM image in Figure 4a shows the approximate intermolecular distance of 0.36 nm. Therefore, intermolecular distance of **C_{16}A-Zn** was determined to be 0.364 nm.

Notes and References

(1) C. Dri, M. V. Peters, J. Schwarz, S. Hecht, L. Grill, *Nat. Nanotechnol.* **2008**, *3*, 649–653.

(2) J. A. A. W. Elemans, S. Lei, S. De Feyter, *Angew. Chem. Int. Ed.* **2009**, *48*, 7298–7332.

(3) J. Otsuki, Y. Komatsu, D. Kobayashi, M. Asakawa, K. Miyake, *J. Am. Chem. Soc.* **2010**, *132*, 6870–6871.

(4) H. Xu, A. Minoia, Ž. Tomovic´, R. Lazzaroni, E. W. Meijer, A. P. H. J. Schenning, S. De Feyter, *ACS Nano* **2009**, *3*, 1016–1024.

(5) L. Piot, A. Marchenko, J. Wu, K. Müllen, D. Fichou, *J. Am. Chem. Soc.* **2005**, *127*, 16245–16250.

(6) G. M. Florio, J. E. Klare, M. O. Pasamba, T. L. Werblowsky, M. Hyers, B. J. Berne, M. S. Hybertsen, C. Nuckolls, G. W. Flynn, *Langmuir* **2006**, *22*, 10003–10008.

(7) (a) A. Stabel, R. Heinz, F. C. De Schryver, J. P. Rabe, *J. Phys. Chem.* **1995**, *99*, 505–507.; (b) K. Kim, K. E. Plass, A. J. Matzger, *Langmuir* **2003**, *19*, 7149–7152.; (c) P. Samorì, K. Müllen, J. P. Rabe, *Adv. Mater.* **2004**, *16*, 1761–1765.; (d) M. Lackinger, S. Griessl, L. Kampschulte, F. Jamitzky, W. M. Heckl, *Small* **2005**, *1*, 532–539.

(8) G. Sedghi, K. Sawada, L. J. Esdaile, M. Hoffmann, H. L. Anderson, D. Bethell, W. Haiss, S. J. Higgins, R. J. Nichols, *J. Am. Chem. Soc.* **2008**, *130*, 8582–8583.

(9) M.-H. So, V. A. L. Roy, Z.-X. Xu, S. S.-Y. Chui, M.-Y. Yuen, C.-M. Ho, C.-M. Che, *Chem. Asian J.* **2008**, *3*, 1968–1978.

(10) (a) N. J. Tao, G. Cardenas, F. Cunha, Z. Shi, Langmuir 1995, 11, 4445–4448.; (b) X. Qiu, C. Wang, Q. Zeng, B. Xu, S. Yin, H. Wang, S. Xu, C. Bai, *J. Am. Chem. Soc.* **2000**, *122*, 5550–5556.; (c) J. Otsuki, *Coord. Chem. Rev.* **2010**, *254*, 2311–2341.; (d) S. Mohnania, D. Bonifazia, *Cood. Chem. Rev.* **2010**, *254*, 2342–2362.

(11) T. Sakano, K. Higashiguchi, K. Matsuda, *Chem. Commun.* **2011**, *47*, 8427-8429.

(12) P. G. Schouten, J. M. Warman, M. P. de Haas, M. A. Fox, H.-L. Pan, *Nature* **1991**, *353*, 736–737.

(13) (a) J. A. A. W. Elemans, M. C. Lensen, J. W. Gerritsen, H. van Kempen, S. Speller, R. J. M. Nolte, A. E. Rowan, *Adv. Mater.* **2003**, *15*, 2070–2073.; (b) Y. Zhou, B. Wang, M. Zhu, J. G. Hou, *Chem. Phys. Lett.* **2005**, *403*, 140–145.; (c)

J. Otsuki, K. Namiki, Y. Arai, M. Amano, H. Sawai, A. Tsukamoto, T. Hagiwara, *Chem. Lett.* **2009**, *38*, 570–571.

(14) Y. Wakayama, J. P. Hill, K. Ariga, *Surf. Sci.* **2007**, *601*, 3984–3987.

(15) The lattice parameters of **C_{22}O-2H** at the phenyloctane–HOPG interface have also been reported as 4.2 nm × 2.1 nm and 84° in: J. Otsuki, S. Kawaguchi, T. Yamakawa, M. Asakawa, K. Miyake, *Langmuir* **2006**, *22*, 5708–5715.

(16) Binding constant of **C_{22}O-Zn** and pyridine was determined by Benesi-Hildebrand plot. For detail, see Figure 5 in experimental section.

(17) J.-R. Gong, L.-J. Wan, *J. Phys. Chem. B* **2005**, *109*, 18733–18740.

(18) P. Bhyrappa, K. Karunanithi, B. Varghese, *Acta Cryst.* **2007**, *E63*, m3201–m3202.

(19) Although the optimal concentration to observe close packed face-on ordering was 1×10^{-5} M, the ordering manner showed sample dependence.

(20) Boundary C consists of two or three columns. As indicated by a black bar in Figure 3f, intercolumnar distance in boundary C (4.0 nm) was narrower than regular edge-on orderings (5.0 nm). Because this boundary is formed by the mismatch between the domain size and the multiples of intercolumnar distance, the boundary C is considered to have the narrower intercolumnar distance to compensate the mismatch.

(21) P. Iavicoli, H. Xu, L. N. Feldborg, M. Linares, M. Paradinas, S. Stafström, C. Ocal, B. Nieto-Ortega, J. Casado, J. T. López Navarrete, R. Lazzaroni, S. De Feyter, D. B. Amabilino, *J. Am. Chem. Soc.* **2010**, *132*, 9350–9362.

(22) A. Stabel, R. Heinz, J. P. Rabe, G. Wegner, F. C. De Schryver, D. Corens, W. Dehaen, C. Süling, *J. Phys. Chem.* **1995**, *99*, 8690–8697.

Chapter 5

Preparation of Metastable 2-D Ordering of Diarylethene by Light at the 1-Octanoic Acid-HOPG Interface

Abstract

Photoinduced change of the molecular ordering of photochromic diarylethenes possessing hydrogen bonding was studied by STM at octanoic acid-HOPG interface. Upon UV irradiation, new ordering was observed which is different not only from the ordering of the open-ring isomer but also from the ordering prepared from pure closed-ring isomer. The observed photoinduced ordering change is supposed to be not the result of adsorption-desorption process, but to originate from the photochromic reaction at the interface.

Introduction

Supramolecular organization on the two-dimensional (2-D) surface is the subject of intensive research because it potentially allows the formation of functional surfaces, including the development of prototypes of future molecule-based electronic devices.[1] One of the main challenges is the realization of stimuli-controllable highly organized supramolecular nanostructures. Hecht, Grill et al. and Crommie et al. reported the observation of isomerization of individual azobenzene molecules on surface by scanning tunneling spectroscopy (STM) in ultrahigh vacuum condition.[2] Meanwhile, STM observation of self-assembled monolayer (SAM) at the liquid-solid interface is also a powerful technique to visualize individual molecules.[3] By real-time STM analysis dynamic behaviors of individual molecules, such as Ostwald ripening and phase transition, can be accessed.[4] Two-dimensional orderings are reported to change by solvent polarities[5] and chiralities,[6] heating,[7] concentration,[8] co-adsorption of molecules,[9] and photoirradiation.[10] However, all the reported ordering changes at the liquid-solid interface are originating from the replacement of ordering by adsorption-desorption equilibrium between the molecules at interface and the molecules in the solution phase.

To realize the stimuli-controllable 2-D ordering, the molecule should stay in the ordering even after the transformation. However, in general, molecular structural change makes the initial packing unstable. For example, the reported photoinduced 2-D ordering change of SAMs of azobenzene[11] and diarylethene[12] at the liquid-solid interface were explained by replacement of the initial ordering with the photogenerated molecules. Here, we intended to construct photo-controllable stable 2-D ordering made of photochromic diarylethene. For stabilization, a hydrogen-bonding amide group was introduced nearby the photochromic core in addition to the long alkyl chain. Amide group has been widely used for the self-assembled structure[13] and also is currently attracting interest because of its cooperative behavior.[14] We report here 2-D structural ordering change to the metastable phase which is only observed upon photoirradiation. The ordering observed upon photoirradiation is different from either the ordering of the initial open-ring isomer or the ordering of isolated closed-ring isomer.

Results and Discussion

Molecular design and Synthesis

For the observation of photochromic reaction on the graphite surface, high

quantum yield for the cyclization reaction is required. Therefore, for the backbone, 1,2-bis(2-methyl-5-phenyl)hexafluorocyclopentene was chosen because of high cyclization quantum yield (Φ_{OC} = 0.55).[15] *N*-hexadecylcarbamoyl chain was attached to each end of **1** in order to stabilize the diarylethenes on the graphite surface (Scheme 1). Diarylethene **1** was synthesized via Suzuki coupling reaction (Scheme 2).

Scheme 1. Photochromism of diarylethene **1**.

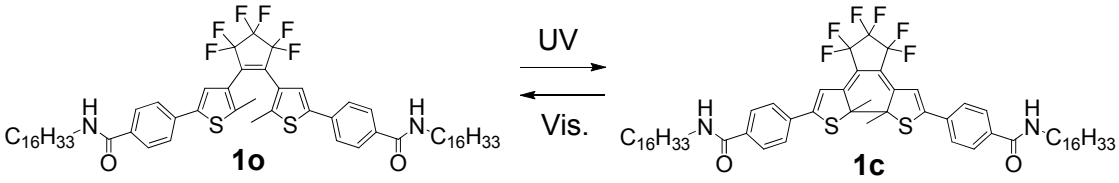

UV-vis. spectroscopy

The open-ring isomer **1o** and the closed-ring isomer **1c** were separated by the HPLC. Photochromic properties were investigated by UV-vis. spectroscopy. In ethyl acetate and in octanoic acid, **1** showed reversible photochromism upon irradiation with UV (365 nm) and visible light (λ > 460 nm). After the separation of **1c** by HPLC in the dark condition, absorption spectra were measured in ethyl acetate and 1-octanoic acid (Figure 1). Then, visible light (λ > 460 nm) was irradiated to these solutions to isomerize from **1c** to **1o**. After recording the spectra of **1o**, UV light of 365 nm was irradiated again to these solutions (Figure 1). The conversion to **1c** was evaluated by

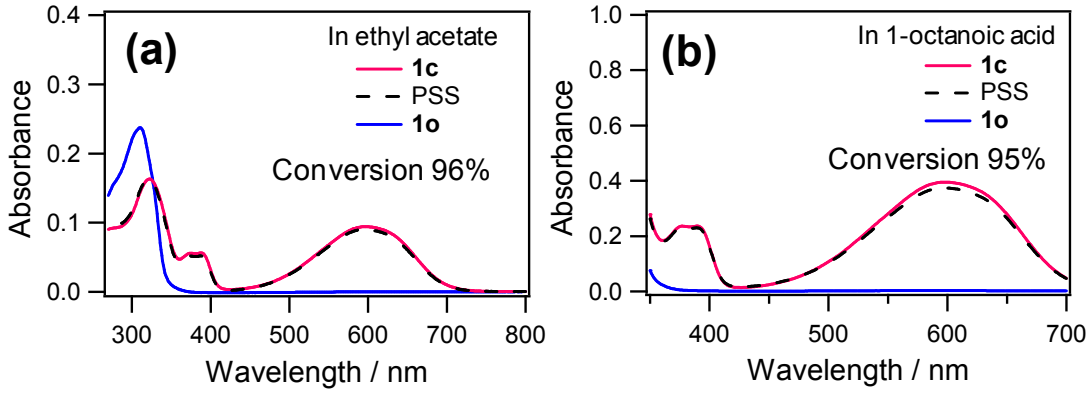

Figure 1. Absorption spectra of **1** (a) in ethyl acetate and (b) in 1-octanoic acid. Red and blue lines show the spectra of **1c** and **1o**, respectively. Dashed black lines show the spectra of photostationary state upon UV (365 nm) irradiation.

comparing the absorbance in the visible region after reaching photostationary state (PSS) to that of initial **1c** solution. Both two solutions had high conversion of 96% in ethyl acetate and 95% in 1-octanoic acid at the PSS (365 nm).

STM measurement of 1o and 1c

SAMs of **1** was analyzed by STM at the 1-octanoic acid-HOPG interface in the constant current mode. **1o** formed SAM of characteristic stripe structure (ordering α, Figure 2a). Molecular model is also shown in Figure 2a. Two bright yellow lines are derived from the columnar aggregates of the dimer of **1o**. Neighboring two **1o** molecules lie in the up-side-down configuration. They are stabilized by the interdigitation of hexadecyl chains and hydrogen bonding of amide groups. One of *N*-hexadecylcarbamoyl chains is not adsorbed on the graphite surface but dissolved in octanoic acid solution or adsorbed on the neighboring diarylethene. Figure 2b shows the STM image of **1c** at the 1-octanoic acid-HOPG interface, which is different from that of **1o** (ordering β). Each **1c** stacked to form columnar structure and two hexadecyl chains crossovered with the angle of 43°. The average domain size of ordering β is relatively larger (> 4×10^4 nm^2) than that of ordering α (4×10^3 nm^2). The ordering of **1c** is more stabilized than that of **1o**.

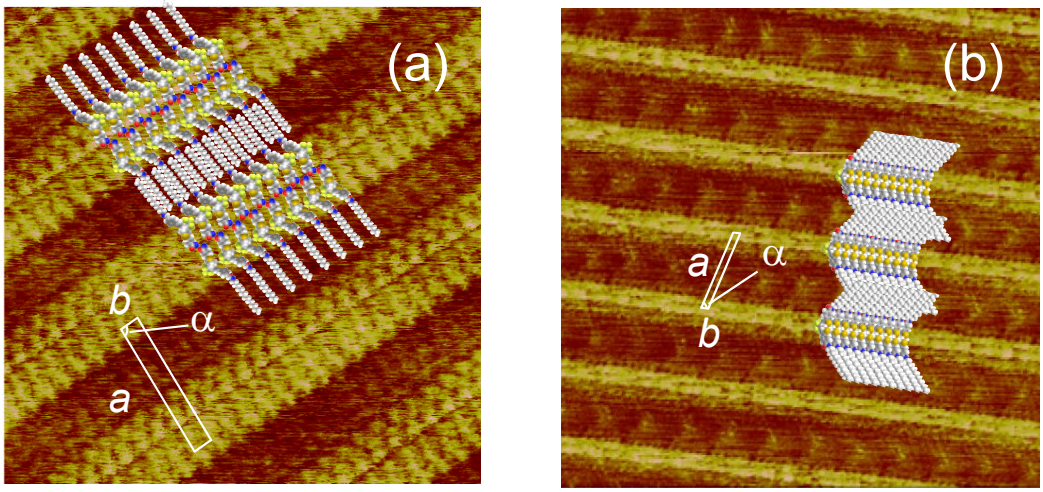

Figure 2. STM images of (a) **1o** (ordering α) (20×20 nm^2, I_{set} = 60 pA, V_{bias} = -1.0 V, a = 5.8 nm, b = 0.90 nm, α = 86°, S_α = 2.6 nm^2/molecule), (b) **1c** (ordering β) (30×30 nm^2, I_{set} = 30 pA, V_{bias} = -1.0 V, a = 5.1 nm, b = 0.53 nm, α = 75°, S_β = 2.6 nm^2/molecule) at the 1-octanoic acid-HOPG interface with molecular models. One of alkyl chains, which is dissolved into solution phase, was omitted from Figure 2a.

In the case that the mixture of **1o** and **1c** was used, when the **1c** ratio (f_{1c}), namely f_{1c} = [**1c**]/([**1o**]+[**1c**]), was smaller than 0.42, the observed ordering is only α and when **1c** ratio was larger than 0.42 the observed ordering is only β (Figure 3). This means that ordering β is more preferentially formed than ordering α to some extent. Steep change at the turning point suggests cooperative behavior.

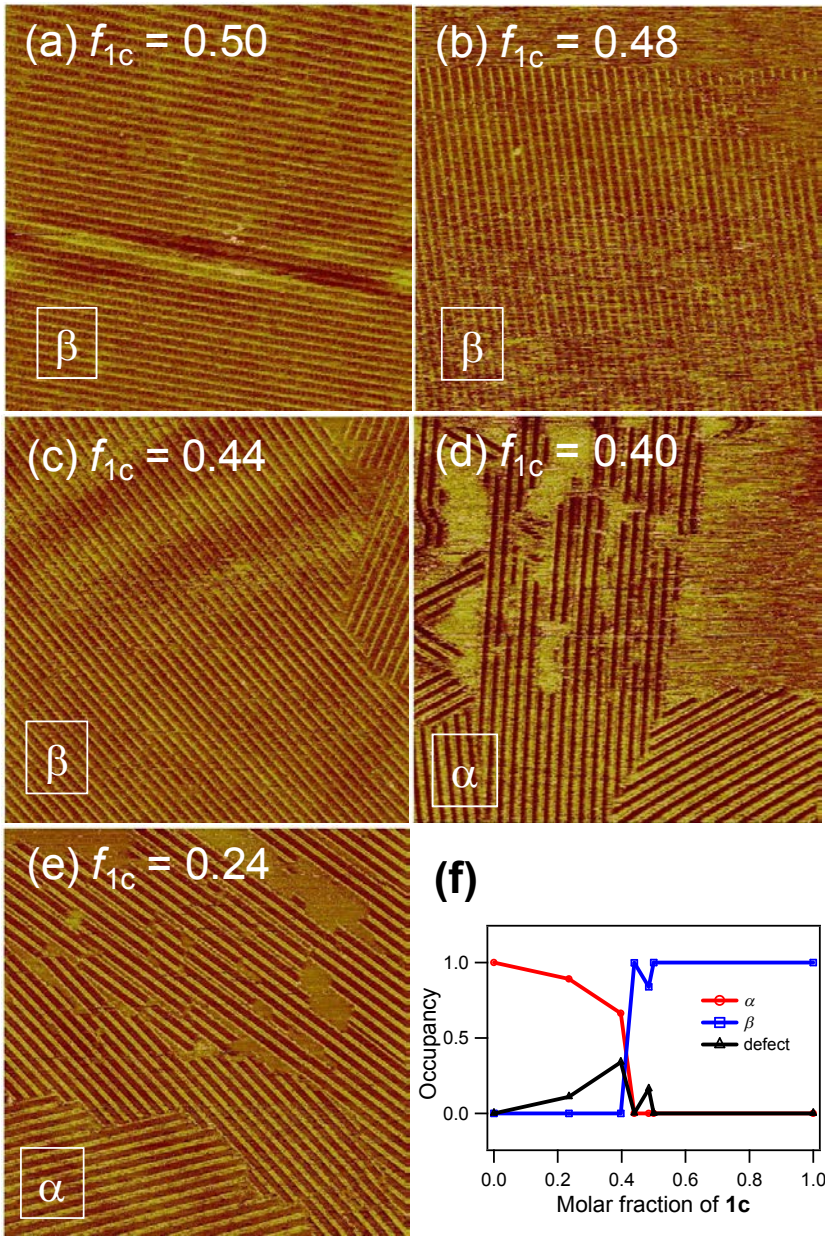

Figure 3. STM images of the mixture of **1o** and **1c** at the 1-octanoic acid−HOPG interface in the constant current mode (200 × 200 nm^2, I_{set} = 30 pA, V_{bias} = −1.0 V): the molar fractions of the **1c** in the solution (f_{1c}) were (a) f_{1c} = 0.50; (b) f_{1c} = 0.48; (c) f_{1c} = 0.44; (d) f_{1c} = 0.40; (e) f_{1c} = 0.24. (f) Occupancy of the ordering α and β and defect on the surface against the f_{1c}.

STM measurements upon photoirradiation

At first of photochemical studies, visible light (λ > 460 nm) was irradiated to ordering β made of pure **1c** at the 1-octanoic acid-HOPG interface and the change of STM image was traced. The surface ordering changed from β to α clearly by 5 min irradiation. Growth of ordering α was observed over the time (Figure 4). This behavior is very similar to that observed in the experiment with diarylethene having pyrene moiety.[12] Adsorption-desorption equilibrium can explain this behavior.

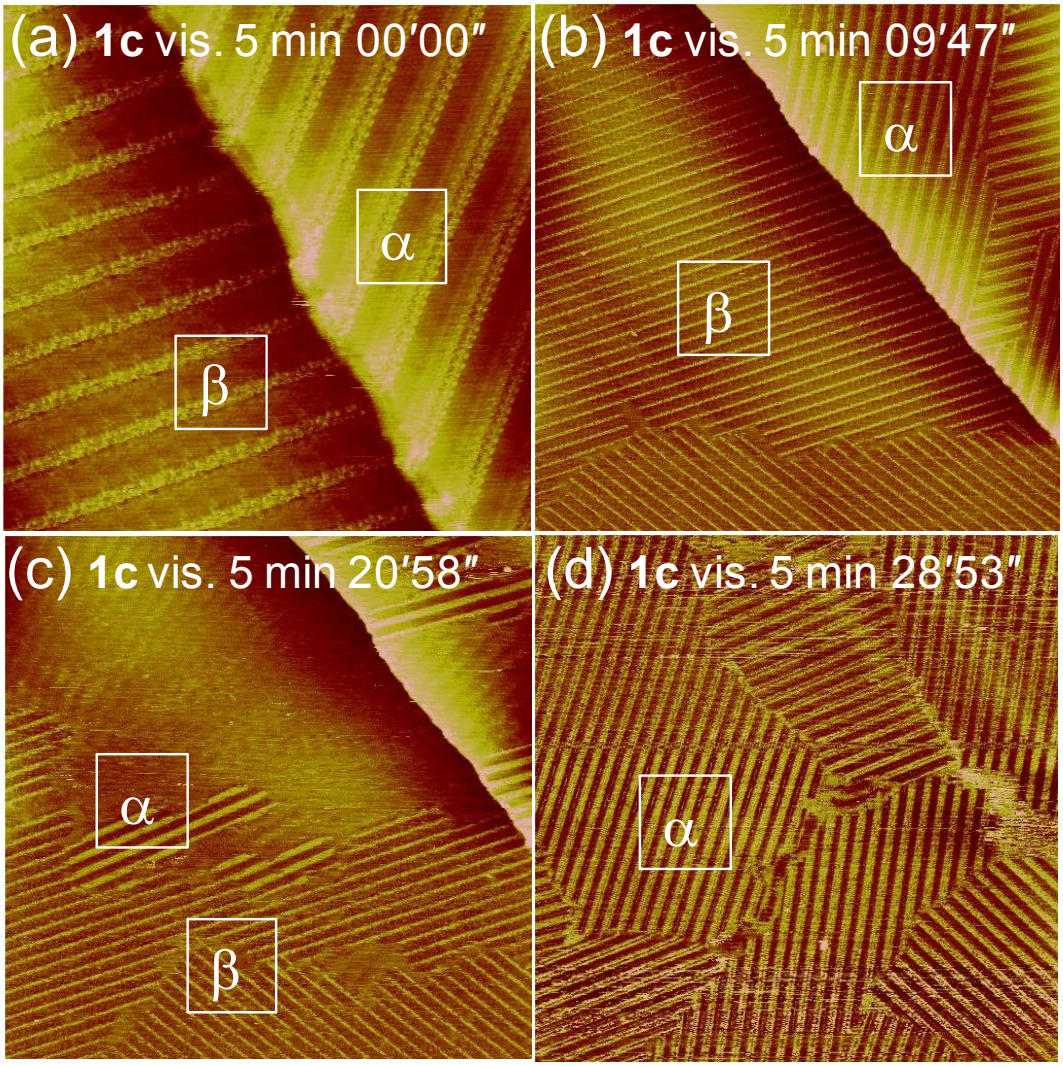

Figure 4. STM images of **1c** after visible light irradiation for 5 min at the 1-octanoic acid-HOPG interface (I_{set} = 30 pA, V_{bias} = -1.0 V): (a) just after photoirradiation (50 × 50 nm^2); (b) 9 min 47 sec (200 × 200 nm^2); (c) 20 min 58 sec (200 × 200 nm^2); (d) 28 min 53 sec (200 × 200 nm^2).

Secondly, UV light of 365 nm was irradiated to the ordering α made from the solution of pure **1o** at the octanoic acid-HOPG interface. Figure 5a and b show the STM image after UV irradiation for 15 min. Interestingly, the new ordering was observed. The ordering manner was different not only from ordering α but also from ordering β (ordering γ). Dimer structure of ordering α was transformed to the columnar structure. Because the shorter irradiation time (1 min) did not generate the ordering γ (vide infra), the new ordering is suggested to originate from the photogenerated closed-ring isomer. Since mixed solution of the open- and closed-ring isomer **1o** and **1c** only yield ordering α and β, this behavior cannot be explained by adsorption-desorption equilibrium. By comparing with the molecular model of ordering β made of **1c** shown in Figure 2b, ordering γ was revealed to be different from the ordering β in that new ordering γ does not have crossover chains. Two types of alkyl parts, which are dark brown and yellow parts, were observed. Higher resolution STM image of ordering γ in Figure 5b revealed that these side chains orient in the different directions with angular interval of 146°. By analyzing the orientation of HOPG underneath, it is revealed that the yellow and brown alkyl chains inclined +3° and +22° with respect to <11-20> direction of HOPG, respectively (Figure 5b). The occupied area by one molecule in ordering γ (S_γ = 3.2 nm^2

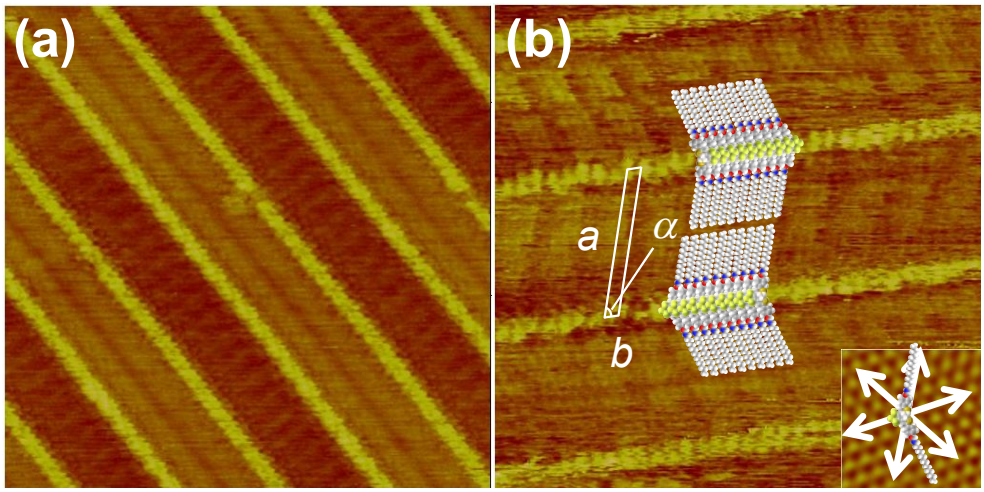

Figure 5. STM images of **1** (ordering γ) after in-situ UV irradiation for 15 min at the 1-octanoic acid-HOPG interface. Before the irradiation, initial ordering was ordering α: (a) (40 × 40 nm^2, I_{set} = 30 pA, V_{bias} = -1.0 V); (b) with molecular models (17.6 × 17.6 nm^2, I_{set} = 30 pA, V_{bias} = -1.2 V, a = 5.9 nm, b = 0.56 nm, α = 73°, S_γ = 3.2 nm^2/molecule). White double-headed arrows show the <11-20> direction of HOPG substrate underneath.

/molecule) became larger than that of ordering α (S_α = 2.6 nm^2/molecule). To expand the occupied size by photoirradiation, some molecules are required to desorb from the surface to the solution phase.

The photoinduced phase transition was analyzed by changing the UV irradiation time (Figure 6). UV irradiation for 1 min did not change the ordering and did not desorb the SAMs, which suggests that ordering α has relatively high stability against mixing with small fraction of **1c**. After 3 min irradiation, both orderings α and γ were observed in separate domains. The smallest angular interval between diarylethene columns of ordering α and γ was 7°. UV irradiation for 20 min yielded only the ordering γ. In the situation of 3 min irradiation, since orderings α and γ were observed on the same substrate, the content of the solution is the mixture of **1o** and **1c**. However, mixed solution did not yield the ordering γ. This result suggests that the observed orderings were different in the cases of (i) dropping a mixed solution of **1o** and **1c** onto the HOPG surface and (ii) firstly dropping a solution of **1o** and then isomerizing **1o** to **1c** by in-situ UV irradiation.

Chronological change of the surface ordering was measured after stopping UV irradiation for a short-time (3 min). Figure 7a shows the STM image just after the irradiation. Phase transition has already started to occur during the irradiation time of 3min. Although small fragmented domains of ordering γ were observed, some domains of ordering α were still observed as indicated by white line in Figure 7a. Continuous recording of the STM images without further photoirradiation revealed that domain size of ordering γ grew up over the time. Figure 7b shows the STM image after UV irradiation for 3 min and leaving for 26 min. Average domain size of ordering γ became 2.5 times larger (Figure 7c), and the fraction of surface occupancy of ordering γ also increased (Figure 7d). These results revealed that (i) first phase transition from ordering α to small domains of ordering γ quickly took place within 3 min irradiation, then (ii) the small domains of ordering γ gradually grew up by Ostwald ripening phenomena.[4a] It is noted that the quick formation of the small domain of the ordering γ suggests the quick surface reorientation from ordering α to ordering γ. More importantly, ordering β was never observed throughout this experiment, though the closed-ring isomer **1c** should exist in the solution phase. This implies that the ordering γ is not an unstable transient structure, but a stable ordering.

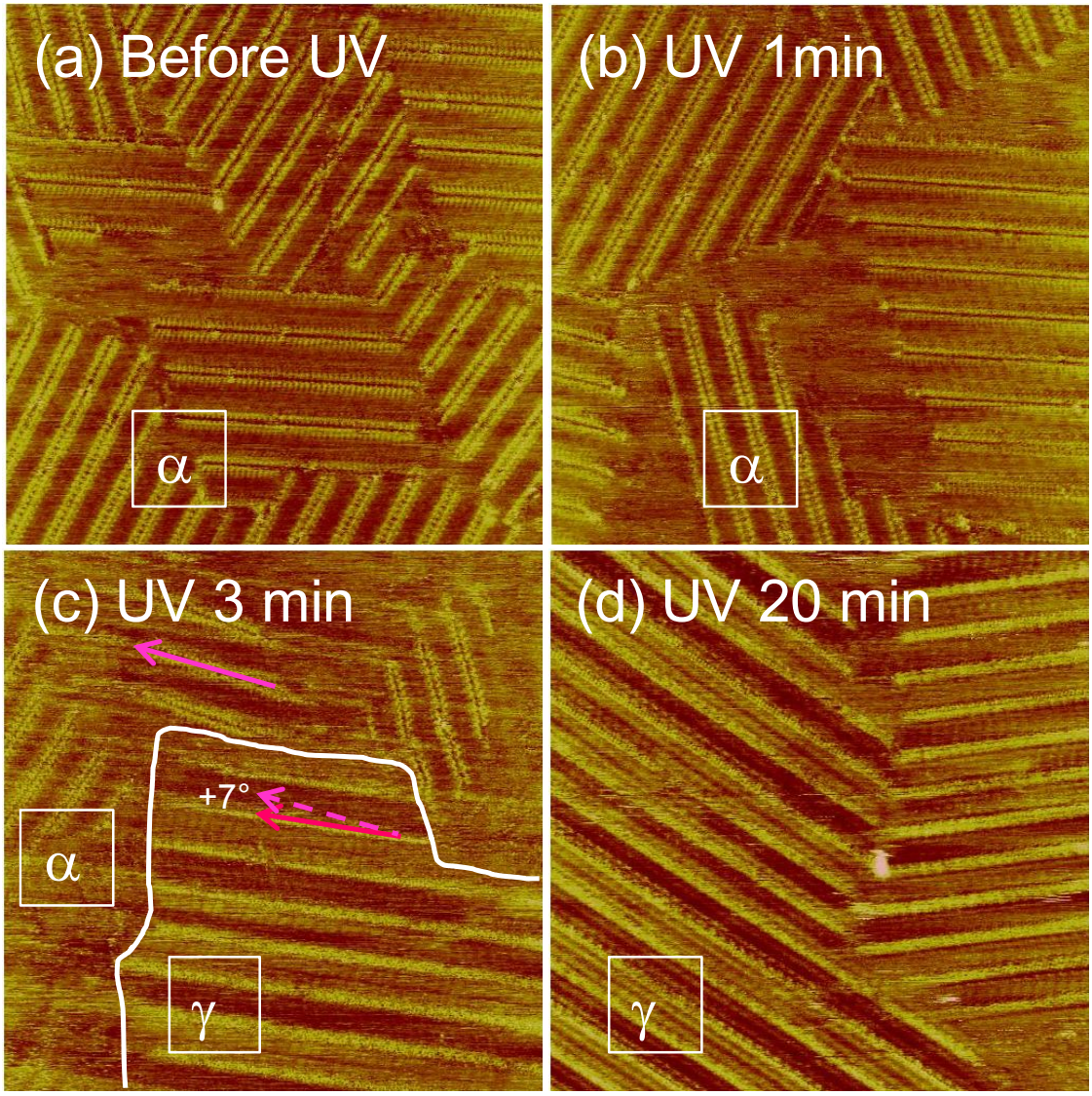

Figure 6. STM images of 1o at the 1-octanoic acid−HOPG interface in the constant current mode (80 × 80 nm^2); (a) before irradiation (I_{set} = 30 pA, V_{bias} = −0.6 V); (b) after UV (365 nm) irradiation for 1 min (I_{set} = 30 pA, V_{bias} = −0.6 V); (c) for 3 min (I_{set} = 30 pA, V_{bias} = −0.6 V); (d) for 20 min (I_{set} = 30 pA, V_{bias} = −1.0 V). Pink solid and dashed arrows show one of the columnar directions of ordering α, and red arrow shows that of ordering γ. The angular interval between these arrows was 7°.

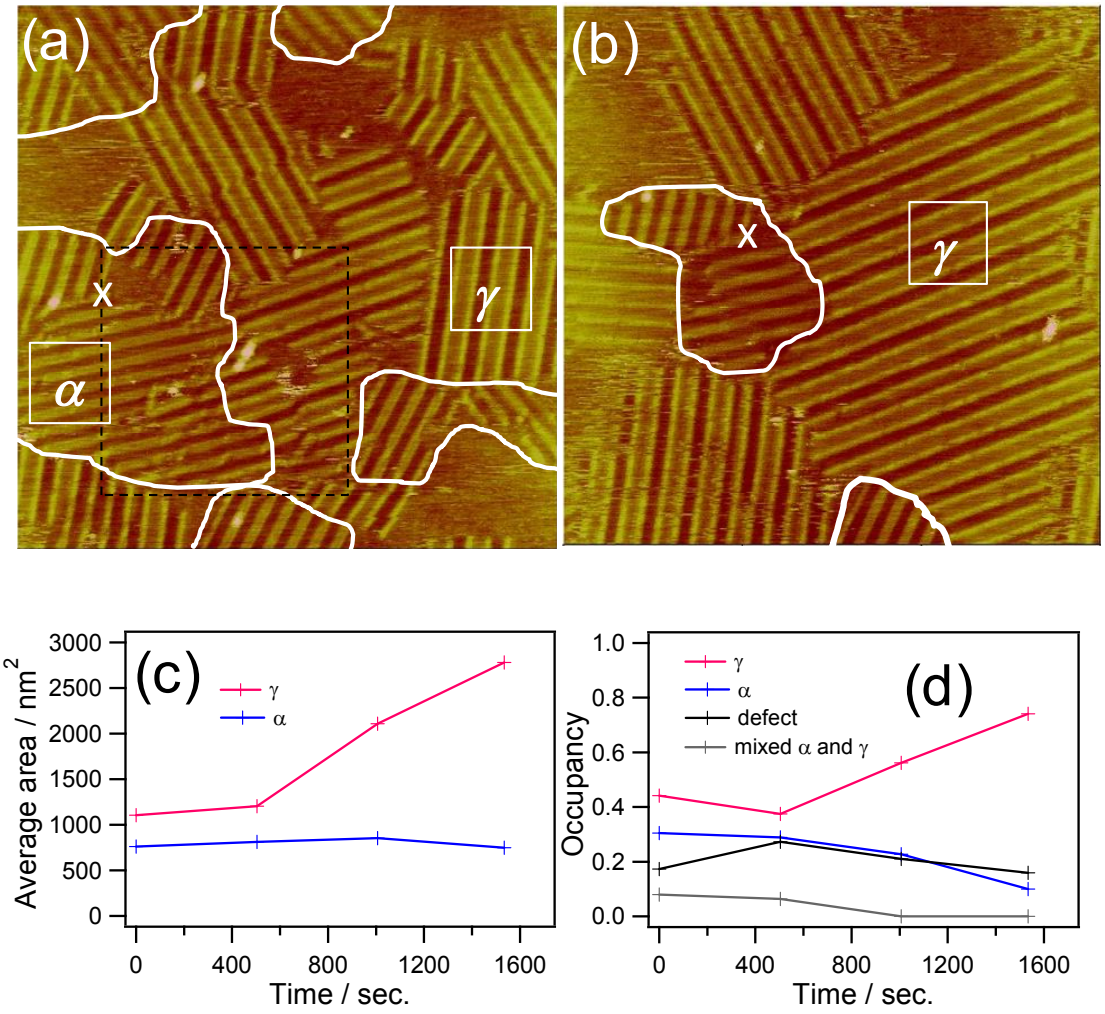

Figure 7. Chronological change of the STM images of 1 after UV irradiation for 3 min at the 1-octanoic acid-HOPG interface (150 × 150 nm^2, I_{set} = 30 pA, V_{bias} = -1.0 V): (a) just after irradiation; (b) leaving after 26 min. Ordering α was indicated by the white line. White "x" shows the same position in Figures a and b. Black dashed square was enlarged in Figure 8a. (c) Chronological change of the averaged domain sizes of orderings α (blue) and γ (red). (d) Chronological change of the occupancy of orderings α (blue), γ (red), defect (black) and mixed domain of α and γ (gray).

Further analysis of Figure 3a revealed the evidence of phase transition on surface. Figure 8a shows the enlarged image of Figure 7a in the region of mixed domain of orderings α and γ. Three columns of diarylethene shown by black arrows are crossing the multiple domains of ordering α and γ. If this phase transition were arising from adsorption-desorption equilibrium, such unstable structure would never be observed.

Phase transition from ordering α to γ is supposed to occur without complete dissolution of ordering α into the solution phase. This behavior is rationally explained by the transition at the interface.

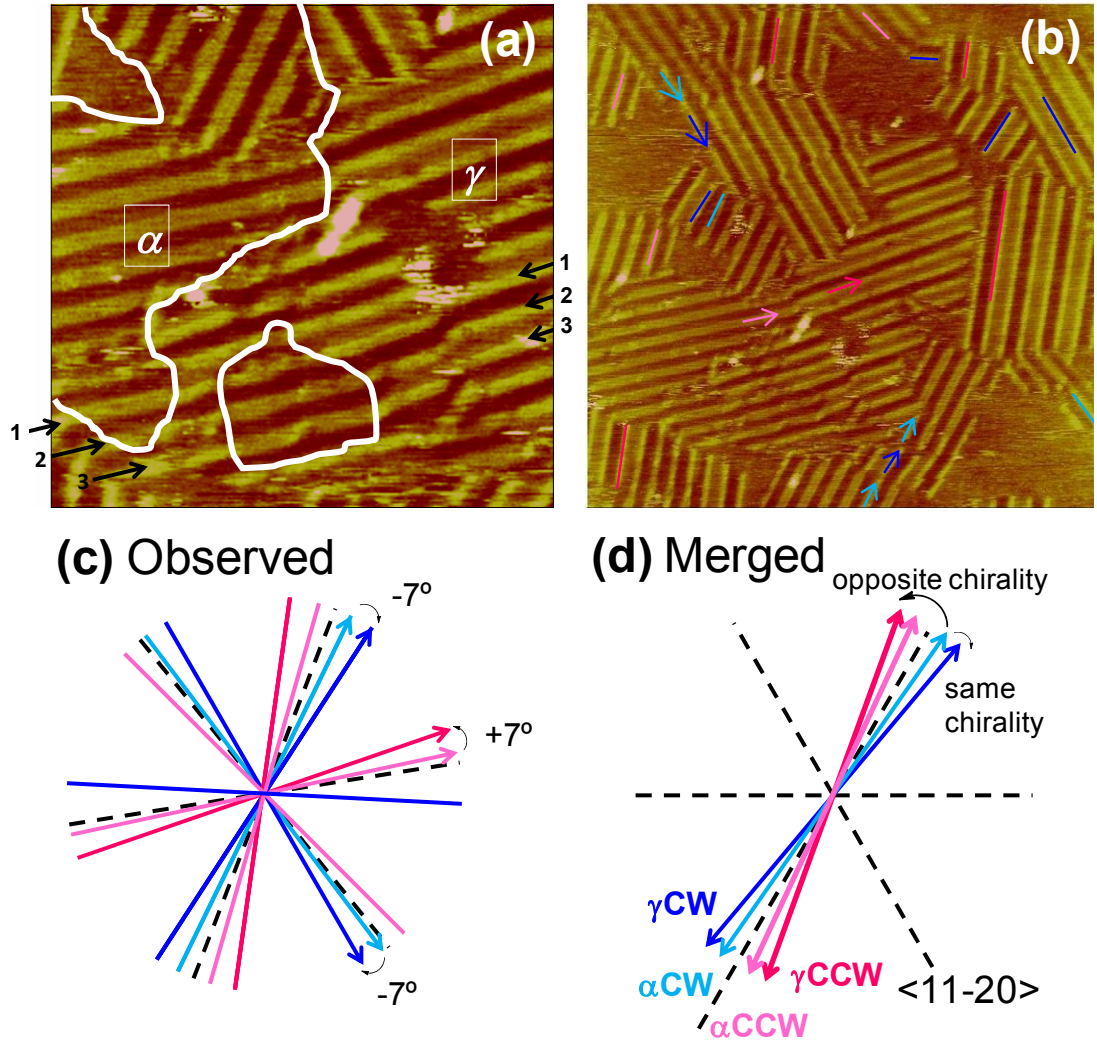

Figure 8. (a) An enlarged image of Figure 3a in the region marked by dashed black square (70 × 70 nm^2). Three mixed columns of orderings α and γ were shown by black arrows. Ordering α is surrounded by white lines. (b) Angular analysis of Figure 3a. Sky blue, pink, blue and red arrows and bars show the columnar direction of orderings α_{CW}, α_{CCW}, γ_{CW}, and γ_{CCW}, respectively (see text). (c) Observed columnar direction of orderings α and γ. (d) Merged angular interval of ordering α (± 4°) and γ (± 10°) with respect to <11-20> direction of HOPG .

Two-dimensional chiral isomerization at the interface

The diarylethene columnar direction is analyzed for the ordering of Figure 7a (Figure 8b). Sky blue and pink bars and arrows show the direction of diarylethene columns in ordering α and blue and red bars and arrows show that in ordering γ. The observed columnar directions of ordering α and γ (Figure 8c) were merged with respect to <11-20> direction of HOPG (Figure 8d). The columnar directions of ordering α were ±4°and those of ordering γ were ±10° (Figure 9). Columnar directions of clockwise from the <11-20> direction (-4°, sky blue, α_{CW}; -10°, blue, γ_{CW}) and counterclockwise (+4°, pink, α_{CCW}; +10°, red, γ_{CCW}) were supposed to have opposite 2-D chirality. If the photoinduced ordering change proceeds with keeping the 2-D chirality, the angular interval should be 6°. In Figure 8b, the colored arrows show the successively linked columns of orderings α and γ. These columns are derived from partially phase-transited ordering. The combination of two successively linked columns were only from pink to red (α_{CCW} to γ_{CCW}) or form sky blue to blue (α_{CW} to γ_{CW}) and the angular interval was

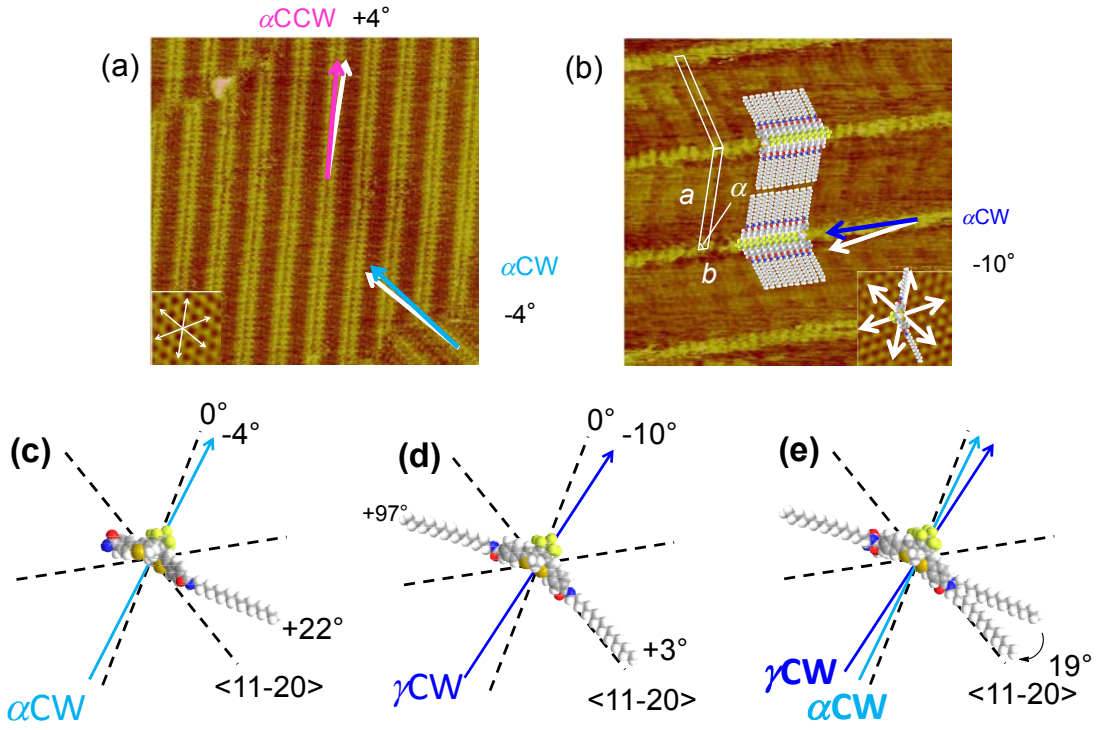

Figure 9. STM images of (a) the ordering α_{CW} of **1o** and (b) the ordering γ_{CW}. Molecular models of (c) **1o** in the ordering α_{CW} and (d) **1c** in the ordering γ_{CW}. (e) Superposed image of c and d.

7°. These results suggest the photoinduced phase transition took place with keeping 2-D chirality. This means the 2-D chirality of ordering γ is determined by the chirality of parent ordering α. This relationship was also observed in another experiment (Figure 6c). When the transition occurs at the interface, the 2-D chirality should be kept, thus the retention of chirality is another support to explain the transition at the interface.

Proposed molecular movement during photo-induced phase transition

The observed phase transition is summarized as follows (Figure 10). Firstly, **1o** forms a SAM on the HOPG substrate. Secondly, UV irradiation induces the photochromic reaction from **1o** to **1c** on the HOPG surface. Then, molecules **1c** are lifted up from the substrate along with the molecular structural change. Thirdly, molecules **1c** stack and align each other to make their columnar direction move away from <11-20> direction by 7°. Ordering γ should contain some amount of the open-ring isomer **1o** because UV irradiation also induces the reverse photochromic reaction, but the phase transition should occur when the ratio of the closed-ring isomer **1o** gets larger than certain critical ratio. The ordering stabilized by hydrogen bonding is considered to be stable even after isomerization and allows the transition at the interface. The phase transition behavior is found to be strongly influenced by the presence of HOPG surface.

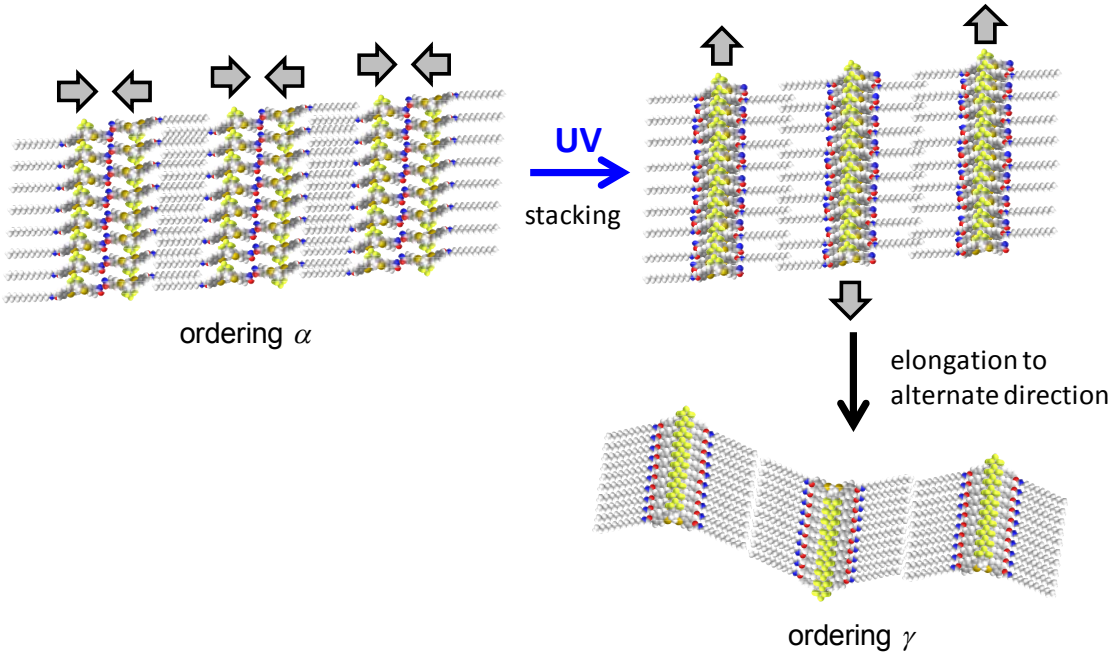

Figure 10. Proposed molecular movement during phase transition from ordering α to γ.

Conclusion

In conclusion, we have investigated photoinduced change of the molecular ordering of photochromic diarylethenes possessing hydrogen bonding by STM at octanoic acid-HOPG interface. Upon in-situ UV irradiation, new ordering was observed which is different not only from the ordering of the open-ring isomer but also from the ordering prepared from pure closed-ring isomer. Judging from the fact that the transformation proceeded with keeping the 2-D chirality and that some molecular columns crossed multiple domains of two different phases, the photoinduced ordering change is not the result of adsorption-desorption process, but is originating from the photochromic reaction at the interface. Hydrogen bonding stabilized the ordering even after isomerization and helped the transition at the interface.

Experimental details

1. Syntheses of the materials

General. ^{1}H NMR spectra were recorded on a JEOL JMN-A500 instrument. Mass spectra were obtained by Bruker autoflex III MALDI-TOF mass spectrometer and Thermo Scientific Exactive mass spectrometer. All reactions were monitored by thin-layer chromatography carried out on 0.2 mm Merck silica gel plates (60F-254). Column chromatography was performed on silica gel (Nakarai, 70-230 mesh). Final product was purified by the HPLC (Kanto chemical, Mightysil Si 60 250-4.6, 5 μm).

Scheme 2. Synthesis of **1o**.

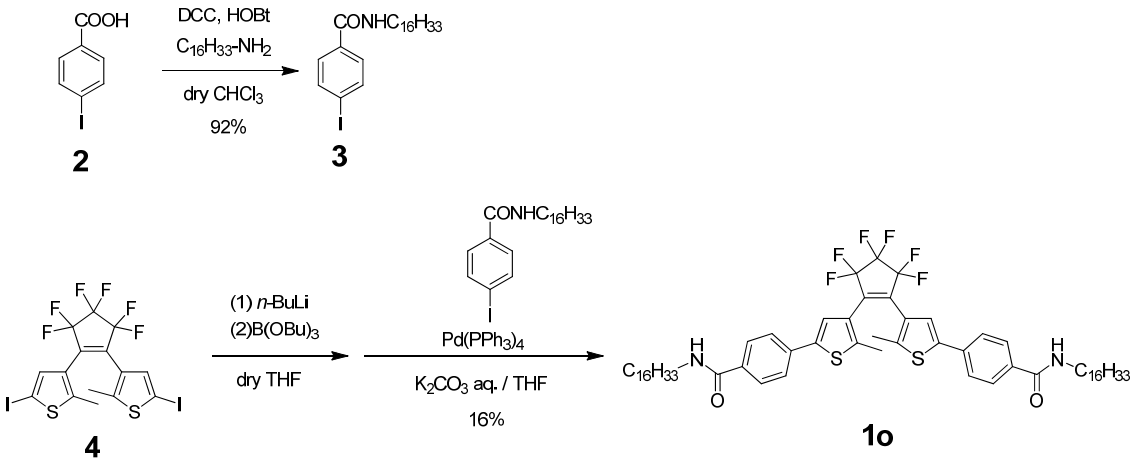

***N*-hexadecyl-4-iodobenzamide (3)**

To a solution of 4-iodobenzoic acid (**2**) (2.48 g, 10.0 mmol) in dry $CHCl_3$ (50 mL) was added 1-hexadecylamine (3.21 g, 15.0 mmol) *N*,*N*'-dicyclohexylcarbodiimide (DCC) (4.12 g, 20 mmol) and 1,2,3-benzotriazole-1-ol (HOBt) (1.35 g, 10.0 mmol). The mixture was stirred for 4 days at room temperature. After a filtration, the filtrate was evaporated *in vacuo*. The crude was extracted by diethyl ether. The organic layer was washed with brine for three times, dried with $MgSO_4$, filtrated and evaporated *in vacuo*. The crude was purified by column chromatography (silica, MeOH:$CHCl_3$=1:9) to yield *N*-hexadecyl-4-iodobenzamide (**3**) (4.35 g, 9.23 mmol, 92%) as a white solid.
MALDI TOF-MS (*m*/*z*) $[M+H]^+$ calcd for $C_{23}H_{39}INO$: 472; found: 472. ^1H NMR ($CDCl_3$, 500 MHz, TMS) δ 0.88 (t, *J* = 7 Hz, 3H), 1.25-1.39 (m, 26H), 1.60 (quin, *J* = 7 Hz, 2H), 3.43 (q, *J* = 7 Hz, 2H), 6.05 (s, 1H), 7.48 (d, *J* = 7 Hz, 2H), 7.78 (d, *J* = 7 Hz, 2H).

4,4'-(4,4'-(perfluorocyclopent-1-ene-1,2-diyl)bis(5-methylthiophene-4,2-diyl))bis(*N*-hexadecylbenzamide) (1o)

A solution of 3,3'-(perfluorocyclopent-1-ene-1,2-diyl)bis(5-iodo-2-methylthio -phene) (**4**) (500 mg, 0.81 mmol) in dry THF (30 mL) was cooled down to -78°C in N_2 atmosphere and *n*-BuLi (1.6 M, 1.1 mL, 1.8 mmol) was slowly added by a syringe pomp. The mixture was stirred for 30 min and tributyl borate (556 mg, 2.42 mmol) was added. After stirring for 1h, the mixture was allowed to room temperature and this reaction was quenched by an addition of water. To a solution of the mixture was added tetrakis(triphenylphosphine)paradium(0) (93 mg, 80 μmol), **3** (1.01 g, 2.42 mmol), and potassium carbonate aq. (20 wt%, 10 mL). The mixture was refluxed for 2h, cooled down to room temperature and extracted by diethyl ether. The organic layer was washed with brine, dried with $MgSO_4$, filtered and concentrated *in vacuo*. The crude was purified by column chromatography (silica, chloroform), GPC (chloroform) and HPLC (EtOAc:Hexane = 1:9) to yield **1o** (139 mg, 129 μmol, 16%) as a white-blue powder. Retention times of **1o** and **1c** were 22 min and 14 min, respectively.
ESI TOF-HRMS (*m*/*z*) $[M+H]^+$ calcd for $C_{61}H_{84}F_6N_2O_2S_2H^+$: 1055.5951; found: 1055.5948. ^1H NMR ($CDCl_3$, 500 MHz, TMS) δ 0.88 (t, *J* = 7 Hz, 6H), 1.23-1.40 (m, 52H), 1.63 (quin, *J* = 7 Hz, 4H), 3.46 (q, *J* = 7 Hz, 4H), 6.08 (t, *J* = 6 Hz, 2H), 7.34 (s, 2H), 7.59 (d, *J* = 8 Hz, 4H), 7.77 (d, *J* = 8 Hz, 4H).

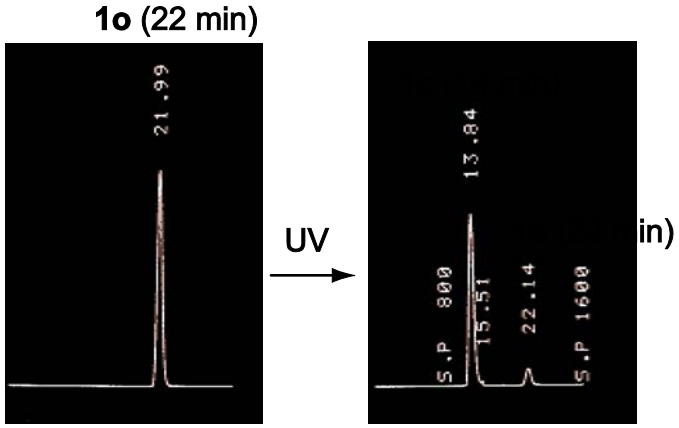

Figure 11. HPLC charts of **1o** before and after UV irradiation.

2. STM measurement

All STM experiments were performed at room temperature and ambient conditions. The STM images were acquired with a Digital Instrument Multimode Nanoscope IIIa and obtained at liquid-solid interface. All STM images were acquired in the constant current mode. The STM tips were electrochemically etched in a $CaCl_2$/HCl aqueous solution from Pt/Ir (80/20, diameter 0.25 mm) wire. Highly oriented pyrolytic graphite purchased from the Veeco Metrology Group was used as a substrate. Solutions of **1o** and **1c** in 1-octanoic acid for the STM measurements were prepared by mixing into the solvent with heating. Concentrations of the solution used for STM measurements (10-30 μM) were checked by absorption spectroscopy. A drop of the solution (10 μL) was deposited onto freshly cleaved HOPG, and the tip was immersed into the solution and the image scanned. Images were analyzed by using the graphite substrate as a calibration grid.

3. Photochemical reaction

Absorption spectra were measured on a spectrophotometer (JASCO V-670). Optical length of the quartz cell was 1 cm. Photoirradiation study for STM investigation was performed using a Keyence UV-400 UV-LED equipped with an optical fiber for UV irradiation and a USHIO 500 W super high-pressure mercury lamp with a thermal cut filter and sharp cut filter (Y-48) for visible light. UV light (300 mW/cm^2, λ = 365 nm) and visible light (80 mW/cm^2, λ > 460 nm) were used for the photoreaction. The photoirradiation time was automatically controlled.

4. Lattice constants

Table 1. Lattice constants of the unit cell of the orderings α, β and γ.

ordering	*a* / nm	*b* / nm	α / °	area / $nm^2 molecule^{-1}$
α	5.8	0.90	86	2.6
β	5.1	0.53	75	2.6
γ	5.9	0.56	73	3.2

5. Chronological change of the SAMs of 1o after UV irradiation for 3 min.

Chronological change of the surface ordering after UV irradiation was measured by leaving the sample without irradiation (Figure 12). White arrow shows the disordered lines in ordering γ, in which two brown lines are consecutive. The growing of the disordered lines can be seen.

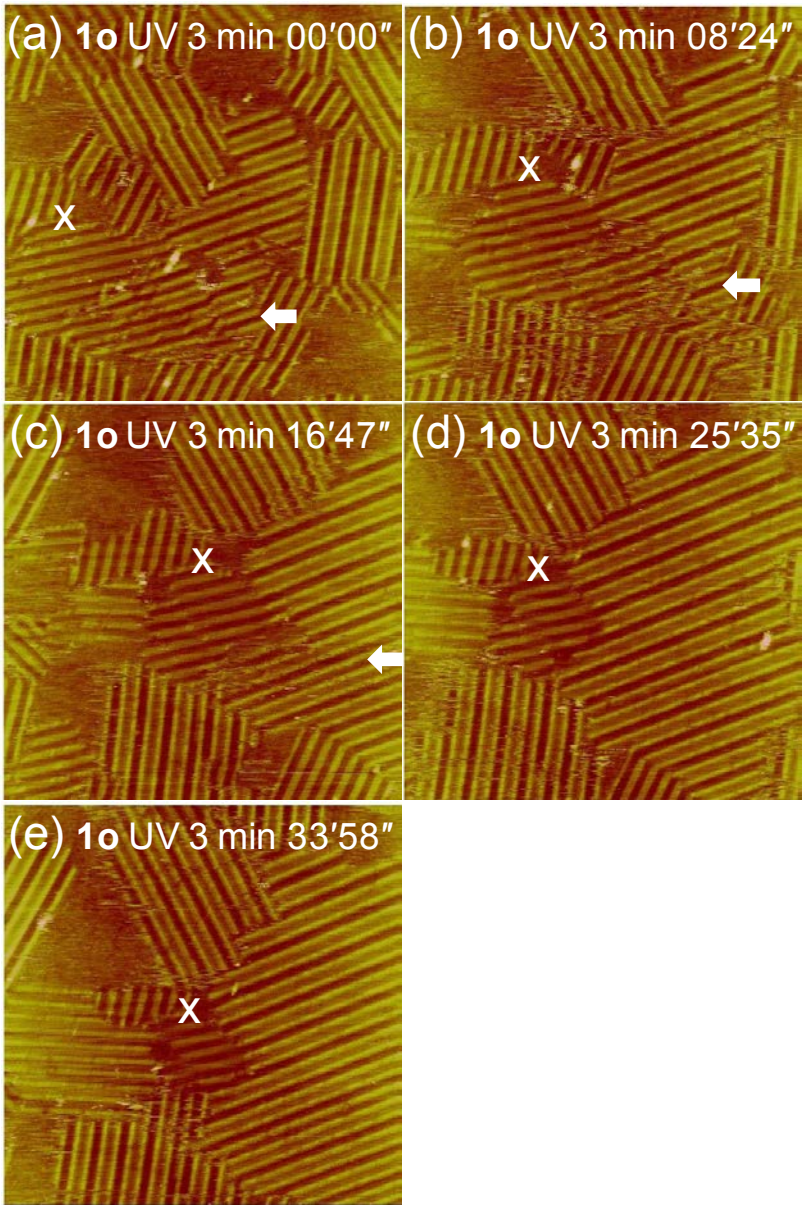

Figure 12. Chronological change of the STM images after UV irradiation for 3 min at the 1-octanoic aicd-HOPG interface. The initial SAM of ordering α was prepared from a solution of pure **1o**. (a) Just after UV irradiation, (b) 8min 24 sec, (c) 16 min 47 sec, (d) 25 min 35 sec and (d) 33 min 58 sec. White "x" shows the same position. The white arrow shows the disordered lines in ordering γ.

Notes and References

(1) (a) Lehn, J.-M. *Proc. Natl. Acad. Sci. USA* **2002**, *99*, 4763–4768. (b) Barth, V.; Costantini, G.; Kern, K. *Nature* **2005**, *437*, 671–679. (c) Müllen, K.; Rabe, J. P. *Acc. Chem. Res.* **2008**, *41*, 511–520.

(2) (a) Alemani, M.; Peters, M. V.; Hecht, S.; Rieder, K. H.; Moresco, F.; Grill, L. *J. Am. Chem. Soc.* **2006**, *128*, 14446–14447. (b) Dri, C.; Peters, M. V.; Schwarz, J.; Hecht, S.; Grill, L. *Nat. Nanotechnol.* **2008**, *3*, 649–653. (c) Comstock, M. J.; Levy, N.; Kirakosian, A.; Cho, J. W.; Lauterwasser, F.; Harvey, J. H.; Strubbe, D. A.; Frechet, J. M. J.; Trauner, D.; Louie, S. G.; Crommie, M. F. *Phys. Rev. Lett.* **2007**, *99*, 038301.

(3) Elemans, J.; Lei, S. B.; De Feyter, S. *Angew. Chem., Int. Ed.* **2009**, *48*, 7298–7333.

(4) (a) Stabel, A.; Heinz, R.; De Schryver, F. C.; Rabe, J. P. *J. Phys. Chem.* **1995**, *99*, 505–507. (b) Florio, G. M.; Klare, J. E.; Pasamba, M. O.; Werblowsky, T. L.; Hyers, M.; Berne, B. J.; Hybertsen, M. S.; Nuckolls, C.; Flynn, G. W. *Langmuir* **2006**, *22*, 10003–10008. (c) Piot, L.; Marchenko, A.; Wu, J.; Müllen, K.; Fichou, D. *J. Am. Chem. Soc.* **2005**, *127*, 16245–16250. (d) Sakano, T.; Higashiguchi, K.; Matsuda, K. *Chem. Commun.* **2011**, *47*, 8427-8429.

(5) Liu, J.; Zhang, X.; Yan, H. J.; Wang, D.; Wang, J. Y.; Pei, J.; Wan, L. J. *Langmuir* **2010**, *26*, 8195–8200.

(6) Katsonis, N.; Xu, H.; Haak, R. M.; Kudernac, T.; Tomovic, Z.; George, S.; Van der Auweraer, M.; Schenning, A. P. H. J.; Meijer, E. W.; Feringa, B. L.; De Feyter, S. *Angew. Chem., Int. Ed.* **2008**, *47*, 4997–5001.

(7) Rohde, D.; Yan, C. J.; Yan, H. J.; Wan, L. J. *Angew. Chem., Int. Ed.* **2006**, *45*, 3996–4000.

(8) (a) Tahara, K.; Okuhata, S.; Adisoejoso, J.; Lei, S.; Fujita, T.; de Feyter, S.; Tobe, Y. *J. Am. Chem. Soc.* **2009**, *131*, 17583–17590. (b) Ha, N. T. N.; Gopakumar, T. G.; Hietschold, M. *J. Phys. Chem. C* **2011**, *115*, 21743–21749.

(9) Guan, C.-Z.; Chen, T.; Wu, J.-Y.; Chen, Q.; Wang, D.; Stang, P. J.; Wan, L.-J. *Langmuir* **2011**, *27*, 9994–9999.; (b) Zhang, X.; Chen, T.; Chen, Q.; Deng, G. J.; Fan, Q. H.; Wan, L. J. *Chem. Eur. J.* **2009**, *15*, 9669–9673.

(10) Shen, Y. T.; Guan, L.; Zhu, X. Y.; Zeng, Q. D.; Wang, C. *J. Am. Chem. Soc.* **2009**, *131*, 6174–6180.

(11) (a) Vanoppen, P.; Grim, P. C. M.; Ru1cker, M.; De Feyter, S.; Moessner, G.; Valiyaveettil, S.; Mü1llen, K.; De Schryver, F. C. *J. Phys. Chem.* **1996**, *100*,

19636–19641. (b) Xu, L.-P.; Wan, L.-J. *J. Phys. Chem. B* **2006**, *110*, 3185–3188.

(12) Arai, R.; Uemura, S.; Irie, M.; Matsuda, K. *J. Am. Chem. Soc.* **2008**, *130*, 9371–9379.

(13) (a) Hameren, R. V.; Schon, P.; Buul, A. M. V.; Hoogboom, J.; Lazarenko, S. V.; Gerritsen, J. W.; Engelkamp, H.; Christianen, P. C. M.; Heus, H. A.; Maan, J. C.; Rasing, T.; Speller, S.; Rowan, A. E.; Elemans, J. A. A. W.; Nolte, R. J. M. *Science* **2006**, *314*, 1433–1436. (b) Iavicoli, P.; Xu, H.; Feldborg, L. N.; Linares, M.; Paradinas, M.; Stafstrom, S.; Ocal, C.; Nieto-Ortega, B. L.; Casado, J.; Navarrete, J. T. L.; Lazzaroni, R.; De Feyter, S.; Amabilino, D. B. *J. Am. Chem. Soc.* **2010**, *132*, 9350–9362.

(14) (a) Green, M. M.; Peterson, N. C.; Sato, T.; Teramoto, A.; Cook, R.; Lifson, S. *Science* **1995**, *268*, 1860–1866. (b) Hirschberg, J. H. K. K.; Brunsveld, L.; Ramzi, A.; Vekemans, J. A. J. M.; Sijbesma, R. P.; Meijer, E. W. *Nature* **2000**, *407*, 167–170.

(15) Nishi, H.; Namari, T.; Kobatake. S. *J. Mater. Chem.* **2011**, *21*, 17249–17258.

List of Publications

Chapter 1.

Conductance Photoswitching of Diarylethene-Gold Nanoparticle Network Induced by Photochromic Reaction
Kenji Matsuda, Hidehiro Yamaguchi, Takeshi Sakano, Masumi Ikeda, Naoki Tanifuji and Masahiro Irie
J. Phys. Chem. C **2008**, *112*, 17005-17010.

Chapter 2.

Percolation-type Photoswitching Behavior in Conductance of Diarylethene–Silver Nanoparticle Networks
Takeshi Sakano, Hidehiro Yamaguchi, Naoki Tanifuji, Masahiro Irie and Kenji Matsuda
Chem. Lett. **2008**, *37*, 634-635.

Chapter 3

Comparison of Molecular Conductance between Planar and Twisted 4-Phenylpyridines by Means of Two-Dimensional Phase Separation of Tetraphenylporphyrin Templates at a Liquid–HOPG Interface
Takeshi Sakano, Kenji Higashiguchi and Kenji Matsuda
Chem. Commun. **2011**, *47*, 8427-8429.

Chepter 4.

Chronological Change from Face-On to Edge-On Ordering of Zinc Tetraphenylporphyrin at Phenyloctane–Highly Oriented Pyloritic Graphite Interface
Takeshi Sakano, Jun-ya Hasegawa, Kenji Higashiguchi and Kenji Matsuda
Chem. Asian J. **2012**, 7, 394-399.

Chapter 5.

Preparation of Metastable 2-D Ordering of Diarylethene by Light at the 1-Octanoic Acid-HOPG Interface
Takeshi Sakano and Kenji Matsuda
Submitted.

Other Publications

1.

Formation of Specific Charge-transfer Complexes between Hyperbranched Polymer Viologen and Neutral Donors in Solid Films Depending on Donor Fraction
Takeshi Sakano, Fuyuki Ito, Osamu Hirata, Masaaki Ozawa and Toshihiko Nagamura
Chem. Lett. **2009**, *38*, 858-859.

2.

Synthesis and Electrochromic Properties of a Highly Water-soluble Hyperbranched Polymer Viologen
Takeshi Sakano, Fuyuki Ito, Tomonori Ono, Osamu Hirata, Masaaki Ozawa and Toshihiko Nagamura
Thin Solid Films **2010**, *519*, 1458-1463.

3.

Fluorescence Properties of Pyrene Derivative Aggregates Formed in Polymer Matrix Depending on Concentration
Fuyuki Ito, Toshifumi Kakiuchi, Takeshi Sakano and Toshihiko Nagamura
Phys. Chem. Chem. Phys. **2010**, *12*, 10923-10927.